THE STRESS, MORPHOLOGY, AND VERTICAL DEFORMATION OF CREEPING FAULTS

by

TYLER J. NEWTON

A DISSERTATION

Presented to the Department of Earth Sciences
and the Division of Graduate Studies of the University of Oregon
in partial fulfillment of the requirements
for the degree of
Doctor of Philosophy

September 2022

DISSERTATION APPROVAL PAGE

Student: Tyler J. Newton

Title: The Stress, Morphology, and Vertical Deformation of Creeping Faults

This dissertation has been accepted and approved in partial fulfillment of the requirements for the Doctor of Philosophy degree in the Department of Earth Sciences by:

Prof. Amanda Thomas	Chairperson and Advisor
Prof. Douglas Toomey	Core Member
Prof. Ray Weldon	Core Member
Prof. Henry Childs	Institutional Representative

and

Krista Chronister	Vice Provost for Graduate Studies

Original approval signatures are on file with the University of Oregon Division of Graduate Studies.

Degree awarded September 2022

DISSERTATION ABSTRACT

Tyler J. Newton

Doctor of Philosophy

Department of Earth Sciences

September 2022

Title: The Stress, Morphology, and Vertical Deformation of Creeping Faults

The goal of my dissertation is to broadly investigate source and surface processes on faults hosting creep and slow fault slip. The discovery of different modalities of slip has proven to be ubiquitous across faults in nearly all geologic settings, yet the geometry and physical properties of the fault surface remain difficult to constrain due to lack of physical access to faults and poorly constrained stress and vertical deformation analyses of regions hosting slow slip and creep. In this dissertation, I present an analysis of crustal stress in the Nankai Trough region of Japan constrained from seismic and aseismic slip. This work shows that slow fault slip source regions may appear to have misoriented stress fields if slow fault slip constitutes a substantial proportion of fault slip and the stress field is not well constrained by earthquakes. Further, I show that the coefficient of friction for areas hosting slow slip events is low ($\mu = 0.19$–0.50), implying frictionally weak materials in the slow slip event source region. Next, I present an analysis of microseismicity and fault structure on the Rattlesnake Ridge landslide. This work highlights a novel approach to detect and associate microseismic events, and an analysis of microseismic events and their source frequency paired with a roughness analysis of an exposed fault scarp that hosted the recorded seismicity. This analysis explores the relationship between fault heterogeneity and source frequency, revealing that source

frequency is most correlated to fault roughness at the scale of 5 cm on the Rattlesnake Ridge landslide, and the source frequency distribution remained nearly uniform throughout the duration of our experiment, suggesting a uniform fracture mechanism and elastic decoupling along the landslide body. Finally, I present an analysis of vertical deformation along coastal Washington that is predominantly driven by the Cascadia subduction zone. In this analysis of vertical land motion, I utilize data from global navigation satellite systems, leveling of geodetic monuments, tide gauge records, and a tectonic model of the Cascadia subduction zone to constrain absolute rates of vertical land movement in coastal Washington. Through this work, I generated a model of absolute vertical land movement that was combined with sea level rise estimates to inform local relative sea level projections on a community-scale.

CURRICULUM VITAE

NAME OF AUTHOR: Tyler J. Newton

GRADUATE AND UNDERGRADUATE SCHOOLS ATTENDED:

    University of Oregon, Eugene, Oregon, USA
    University of Maryland, College Park, Maryland, USA

DEGREES AWARDED:

    Doctor of Philosophy, Earth Sciences, 2022, University of Oregon
    Bachelor of Science, Geology, 2013, University of Maryland

AREAS OF SPECIAL INTEREST:

    Seismology
    Data Science

PROFESSIONAL EXPERIENCE:

    Graduate Research Assistant, University of Oregon, 2016-2022

    Computational Geophysicist Intern, Leidos, 2021-2022

    Visiting Graduate Research Assistant, University of Washington, 2017-2018

    Associate Geologist, Environmental Resources Management, Inc., 2013-2016

    Undergraduate Research Assistant, University of Maryland, 2012-2013

    Intern, NASA Goddard Space Flight Center, 2011-2011

GRANTS, AWARDS, AND HONORS:

    Earth Sciences Emeritus Faculty Tribute Award, University of Oregon, 2021

    Smith Scholarship, University of Oregon, 2020

    Research Recognition Award, University of Oregon, 2020

Earth in 4D Travel Scholarship, IRIS/UNAVCO, 2019

Wikipedia Scientist Fellowship, Wikipedia, 2019

Stovall Fellowship, University of Oregon, 2018

Weiser Scholarship, University of Oregon, 2017

Marthe E. Smith Memorial Science Scholarship, University of Oregon, 2017

Excel Research Scholarship, University of Maryland, 2013

Mineralogical Society of America Award, University of Maryland, 2012

PUBLICATIONS:

Inbal, A., Thomas, A. M., **Newton, T. J.**, and Bürgmann, R. (2021). Complex Migration of Tremor near Cholame, CA Resolved by Seismic Array Analysis. Journal of Geophysical Research: Solid Earth. https://doi.org/10.1029/2021JB022174

Newton, T. J., Weldon, R., Miller, I. M., Schmidt, D., Mauger, G., Morgan, H., Grossman, E. (2021). An Assessment of Vertical Land Movement to Support Coastal Hazards Planning in Washington State. Water. https://doi.org/10.3390/w13030281

Newton, T. J., Thomas, A. M. (2020). Stress Orientations in the Nankai Trough Constrained Using Seismic and Aseismic Slip. Journal of Geophysical Research: Solid Earth. https://doi.org/10.1029/2020JB019841

Uieda, L., Dongdong, T., Leong, W. J., Toney, L., **Newton, T.**, Wessel, P. (2020). PyGMT: A Python interface for the Generic Mapping Tools. Zenodo. https://doi.org/10.5281/zenodo.425345

Miller, I. M., Morgan, H., Mauger, G., **Newton, T.**, Weldon, R., Schmidt, D., Welch, M., Grossman, E. (2018). Projected Sea Level Rise for Washington State – A 2018 Assessment. Prepared for the Washington Coastal Resilience Project.

ACKNOWLEDGMENTS

This research was possible because of conversations and interactions with many people at the University of Oregon over the span of six years. I wish to express sincere appreciation to Professors Thomas, Weldon, Toomey, Rempel, and Childs for their insights, feedback, and guidance throughout the duration of this research. I thank everyone that assisted with field work to make this research possible, especially my friends Alex Babb, Emily Sexton, Geena Littel, and Brennah McVey. In addition, special thanks are due to my coauthors and collaborators, namely my friend Josh Wiejaczka. I'm also thankful for the friends I met during graduate school, especially Tim Lin, Miles Bodmer, Brandon VanderBeek, Chelsea Obeidy, Gabbie LaFayette, and Kevin Gardner. Finally, thanks to everyone else that gave me something to ponder along the way.

Dedicated to my father and his endless sense of wonder.

TABLE OF CONTENTS

LIST OF FIGURES

LIST OF TABLES

CHAPTER I

INTRODUCTION

The strength of subduction thrust faults is key to understanding seismogenesis at the provenance of Earth's largest earthquakes. Earthquake focal mechanisms are routinely inverted to constrain the stress state at seismogenic depths. However, on some megathrusts, deformation is accommodated by both earthquakes and types of slow fault slip. In Chapter II, I employ focal mechanisms of short-term slow slip events (SSEs), a type of slow fault slip, and earthquakes in a regional stress inversion to investigate the stress state of the Nankai Trough megathrust and interpret the results in the context of regional tectonics. Previous studies using earthquake-only stress inversions found principal stress orientations in this region that are incompatible with thrust faulting on the megathrust. When both SSEs and earthquakes are considered, the stress state of the central and eastern Nankai Trough megathrust is well oriented for thrust faulting. The results presented here suggest that slow fault slip source regions may appear to have misoriented stress fields if slow fault slip constitutes a substantial proportion of fault slip and the stress field is not well constrained by earthquakes. In the SSE region, I find that faults are well oriented for failure, suggesting they have strengths similar to their surroundings. Combined with low V_p/V_s ratios and sensitivity to small stress changes, these results imply that the megathrust and surroundings operate at low deviatoric stresses in the SSE source region. Further, I show that the coefficient of friction for areas hosting SSEs is low ($\mu = 0.19$–0.50), implying frictionally weak materials in the SSE source region.

The Rattlesnake Ridge landslide is a unique natural laboratory to study seismic records of landslide deformation due to the continuous exposure of the scarp that accommodates sliding and hosts microseismic events. In the work presented in Chapter III, I detect microseismic events, associate phase arrivals, locate events, and present an analysis of the microseismicity and fault properties of the slow-moving Rattlesnake Ridge landslide. In total I detected 43,661,881 microseismic phase arrivals and 4,837,460 events over the 17-week span of the nodal seismometer experiment. I determined

1

locations for 24,115 events detected on March 13, 2018, the first day of the experiment, and showed that source frequency is most correlated to fault roughness at the scale of 5 cm. Fault roughness at other length scales is not strongly correlated to source frequency. I found a nearly constant source frequency distribution throughout the duration of the experiment, suggesting a uniform fracture mechanism. This research on RRL remains in progress to further explore the relationship between fault heterogeneity and source character.

The sea and land change elevation spatially and temporally from a multitude of processes, so it is necessary to constrain the movement of both to evaluate how coastlines will evolve and how those evolving coastlines will impact the natural and built environment over time. In Chapter IV, I combine land movement observations from global navigation satellite systems (GNSSs), leveling of geodetic monuments, and tide gauge records with a tectonic model of the Cascadia subduction zone to constrain absolute rates of vertical land movement in coastal Washington. I infer rates of vertical land movement in areas lacking direct observations by interpolating high-quality land movement observations and a discretely sampled interseismic locking model. Here I present a model of absolute vertical land movement that is combined with sea level rise estimates to inform local relative sea level projections on a community-scale. The most rapid vertical uplift (~3.5 mm/year) of the land is found across the northwest Olympic Peninsula, which currently outpaces sea level rise. Conversely, some areas, including a stretch of the northern Pacific Ocean coast from La Push to Kalaloch and the southern Puget Sound, are found to be subsiding at 0.5–1.0 mm/year, exacerbating the rate of relative sea level rise and thereby increasing the vulnerability of coastal communities.

CHAPTER II

STRESS ORIENTATIONS IN THE NANKAI TROUGH CONSTRAINED USING SEISMIC AND ASEISMIC SLIP

1. Introduction

Earthquakes are caused by tectonic stresses that govern the type of faulting. The orientation of a tectonic stress field can be described by the three orthogonal principal stresses, σ_1, σ_2, and σ_3, where $\sigma_1 \geq \sigma_2 \geq \sigma_3$ and compression is defined as positive. These principal stresses are, by definition, oriented such that the shear stress on the plane normal to each principal stress is zero. Tectonic stresses accumulate during the interseismic period and are rapidly released as fault slip (Reid, 1910). Anderson (1951) proposed that in an idealized tectonic setting (i.e., absent of topographic stresses), thrust, normal, and strike-slip faults develop in conformance with Mohr-Coulomb yield criterion, with one principal stress axis near vertical because Earth's surface is a boundary with no shear stress. Well-oriented faults composed of rocks with typical friction coefficients ($\mu = 0.6-0.85$ Byerlee, 1978) form and reactivate with the same sense of slip when σ_1, the maximum compressive stress axis, is oriented $\approx 30°$ from the fault plane (Sibson, 1985). Slip on a poorly oriented fault with a high ($> 60°$) or low ($<10°$) angle of σ_1 to the fault plane (and a typical friction coefficient) is less mechanically favorable than the generation of a new well-oriented fault (Sibson, 1985). The occurrence of slip on poorly oriented faults implies either that the tectonic stress orientation is not well constrained or the fault must be considerably weaker, having a lower apparent coefficient of friction, than its surroundings (Hill, 1993). Thus, the orientation of a stress field relative to faults within it can be used as a proxy for fault strength, assuming the stress field is well constrained.

In areas with abundant fault slip data, earthquake focal mechanisms can be used to constrain the tectonic stress field (Maury et al., 2013). Stress inversions solve for a deviatoric stress tensor that best describes the distribution of slip vectors determined from earthquake focal mechanisms. The inverse problem is commonly solved by grid-search methods (Arnold & Townend, 2007; Gephart, 1990; Gephart & Forsyth, 1984), linearized least-squares methods (Hardebeck & Michael, 2006; Michael, 1984), and Monte Carlo-based methods (Angelier, 1984). Focal mechanism inversion methods assume fault slip occurs in the same direction as the resolved shear stress (i.e., the tangential component of the traction vector) (Bott, 1959; Wallace, 1951), the stress field is homogeneous in each discretized domain, fault slip occurs on preexisting faults, and that the considered focal mechanisms are sufficiently diverse to constrain the stress field (McKenzie, 1969). The magnitude of fault slip is not considered in the inversion, so principal stress directions rather than absolute stress values are calculated from the deviatoric stress tensor. However, quantitative models have been developed to estimate in situ stresses from earthquake focal mechanisms in conjunction with high-density borehole stress measurements (Shen et al., 2019). Earthquake focal mechanisms intrinsically contain fault plane ambiguity, so inversions that do not distinguish the fault plane from the auxiliary plane may produce inaccurate results. Vavryčuk (2014) modified the Michael (1984) method to invert jointly for stress and fault orientation, where the nodal plane closest to failure, based on the fault instability coefficient (Lund & Slunga, 1999; Vavryčuk et al., 2013), is selected as the fault plane. If the focal mechanisms utilized in a stress inversion do not accurately sample the tectonic stress field, the calculated deviatoric stress tensor will be misoriented. Martínez-Garzón et al. (2016) detailed a best practice methodology for stress inversions of earthquake focal mechanisms and suggested that aftershock sequences be removed from focal mechanism catalogs so the assumption of stress field homogeneity is not violated by considering internal stress perturbations of earthquake clusters. In this study, we employ stress inversion best practices to determine the spatially variable stress field of the subduction interface in the Nankai Trough region of Japan.

The tectonic setting of Japan is unique in that southwestern Japan hosts subduction of the Philippine Sea plate (PS) beneath the Amur plate (AM) at 63–68 mm year−1 N55°W near the Nankai Trough (Miyazaki & Heki, 2001) while in northeastern Japan the Pacific plate (PA) subducts beneath the Okhotsk plate (OK) (Zonenshain & Savostin, 1981) at 92 mm year−1 N66°W (DeMets et al., 2010), creating the Kuril arc and the Japan arc (Figure 1). Convergence of PS-AM is oblique, causing migration of the
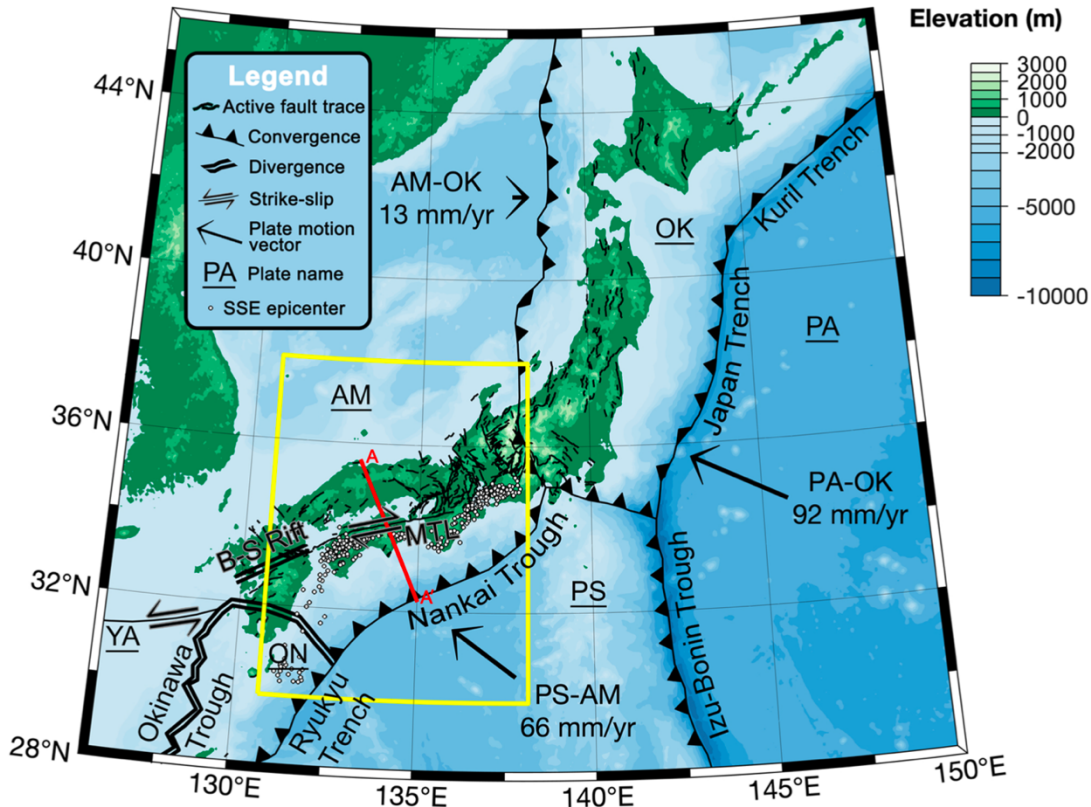
Figure 1. The tectonic setting of Japan. Yellow box denotes the study area. The dominant tectonic features in the Nankai Trough are the Median Tectonic Line (MTL), a right-lateral strike-slip fault, the subducting Philippine Sea plate (PS), the overriding Amur plate (AM), and the Beppu-Shimabara (B-S) rift. The Pacific plate (PA) subducts under the Okhotsk plate (OK) to the north and the Philippine Sea plate to the south. AM-OK subduction forms an incipient subduction zone. To the south, PS subducts beneath the Okinawa plate (ON), adjacent to the Okinawa Trough, a backarc rift. The Okinawa Trough is bordered on the west by the Yangtze plate (YA). Locations of slow slip events considered in this study are denoted by white circles with black outlines. Active fault traces from AIST Research Information Database DB095: Active fault database of Japan (2012). Plate boundaries from Kita et al. (2001) and Bird (2003).

Nankai forearc sliver to the west. The Nankai forearc sliver is bounded on the north by the Median Tectonic Line (MTL), a right-lateral strike-slip fault with an average slip-rate of 5–8 mm year−1 (Tsutsumi et al., 1991). The Ryukyu arc, associated with subduction of the PS beneath the ON, hosts an actively rifting backarc basin, the Okinawa Trough, which decouples the forearc and generates arc-parallel extension (Kubo & Fukuyama, 2003). The Beppu-Shimabara rift transects the island of Kyushu and has been interpreted by Tada (1985) to be a northern extension of the Okinawa Trough. The majority of the seismicity in Japan is associated with PA-OK subduction in the northeast. The Nankai Trough hosts predominantly small (M < 5) thrust earthquakes due to active subduction of the PS beneath the AM and right lateral strike-slip earthquakes due to the proximity of the MTL. The Nankai Trough generated a Mw8.1 earthquake in 1944 and a Mw8.3 earthquake in 1946 (Usami, 1996).

Previous studies that have estimated stress orientations in the Nankai Trough are based on borehole observations and the inversion of earthquake focal mechanisms or fault orientations. The Kii Peninsula has been the site of numerous studies that find σ_1 oriented nearly vertical to 2 km depth (Byrne et al., 2009; Lin et al., 2016; Sacks et al., 2013), suggesting that topographic gradients are a dominant control on the shallow crustal stress state. Townend and Zoback (2006) and Terakawa and Matsu'ura (2010) conducted stress inversions of focal mechanisms shallower than 35 and 50 km, respectively, finding that the orientation of the maximum horizontal compressive stress is dominantly oriented E-W across Japan (due to AM-OK convergence) but varies throughout the Nankai Trough due to the complicated tectonics of the region (and potentially the low seismicity rate). Wang et al. (2004) and Lee et al. (2017) examined focal mechanism solutions in the Nankai Trough, similarly finding E-W compression throughout the Nankai Trough, and downdip tension near Kyushu. Conversely, Ito et al. (2009) derived moment tensor solutions for shallow very-low-frequency (VLF) earthquakes and inverted them to find that σ_1 is trench-normal in the Nankai Trough accretionary prism, indicating that types of fault slip other than traditional earthquakes are useful to constrain the stress field in low-seismicity areas.

Multiple prior studies using focal mechanism stress inversions of the megathrust have revealed principal stress orientations in the Nankai Trough subduction zone that are misoriented for thrust faulting (Hardebeck, 2015; Hardebeck & Loveless, 2018). Hardebeck (2015) investigated principal stress orientations in subduction zones globally to find that in most subduction zones the maximum compressive stress axis plunges trenchward and makes an angle of 45°–60° to the subduction megathrust. However, in the Nankai Trough, Hardebeck (2015) and Hardebeck and Loveless (2018) found maximum compressive stress axis orientations at negative and high angles to the subduction megathrust, differing by >80° in adjacent bins, that are misoriented for thrust faulting. Hardebeck and Loveless (2018) inverted earthquake focal mechanisms across Japan to determine the deviatoric megathrust stress field and found that creeping areas of the Nankai Trough and Japan Trench subduction zones host principal stress orientations that are more poorly oriented for failure than adjacent locked areas. The stress field in an active tectonic margin determines the preferred faulting mechanism in that area, so regions with principal stress orientations incompatible with the observed type of faulting require a physical explanation of such a discrepancy. Hardebeck (2015) attributed the seemingly misoriented principal stress orientations of the Nankai Trough subduction zone to high pore fluid pressure and regionally low deviatoric stress.

An observation of relevance to this study is that the regions with stress fields that are poorly oriented for megathrust faulting found in previous studies are spatially coincident with areas of observed and inferred slow fault slip (Figure S7 Hardebeck & Loveless, 2018). Over the past two decades, analyses of geodetic and seismic time series have revealed various types of slow fault slip in the Nankai Trough subduction zone (Hirose & Obara, 2005; Katsumata & Kamaya, 2003; Obara, 2002; Obara et al., 2004), and other faults globally (Brown et al., 2009; Dragert et al., 2001; Nadeau & Dolenc, 2005; Payero et al., 2008; Rogers & Dragert, 2003), that slip over a range of spatial and temporal scales. Slow slip events (SSEs) constitute distinguishable geodetic episodes of slow fault slip with durations of days to years. VLF earthquakes are slow earthquakes with characteristic time scales of tens of seconds. Low-frequency earthquakes and tremor are another manifestation of slow fault slip that occurs in the Nankai Trough with a

dominant frequency of several Hz (Obara, 2002; Shelly et al., 2007). Episodes of tremor have been found to accompany VLF earthquakes and short-term SSEs (Obara et al., 2004; Rogers & Dragert, 2003), which is termed episodic tremor and slip (ETS). The occurrence of slow fault slip, or creep, in subduction zones varies spatially and temporally along strike and dip and can occur both updip and downdip of the seismogenic zone where earthquakes nucleate.

Tremor and ETS occur in a narrow zone along the downdip edge of the megathrust seismogenic zone in Nankai, while long-term SSEs fill the gap between ETS and the seismogenic zone (Kobayashi, 2014). Shallow VLF earthquakes and short-term SSEs occur updip of the seismogenic zone in this region (Obara & Ito, 2005). Yokota et al. (2016) revealed that areas of slow fault slip bound areas of historic megathrust slip. Various studies have inferred high pore fluid pressures in areas of the Nankai Trough that spatially coincide with shallow slow fault slip (Takemura et al., 2019; Tobin & Saffer, 2009; Ujiie et al., 2018). Friction experiments on materials from the shallow megathrust in the Nankai Trough (Brown et al., 2003; Ikari et al., 2009; Kopf & Brown, 2003), and from faults globally (Bürgmann, 2018; Collettini et al., 2019), reveal low-strength materials; however, the sampling of in situ megathrust materials at the depths of downdip SSEs is not feasible with current methods. In the Hikurangi margin, Warren-Smith et al. (2019) observed temporal evolution of the stress shape ratio in subducting oceanic crust that temporally correlates with SSEs, interpreted as fluid pressure cycling, providing further evidence that the presence of fluids at high pore pressures is a control on the nucleation of SSEs.

Interestingly, the Nankai trough hosts less earthquakes and more slow fault slip than adjacent areas, so SSEs make up a substantial portion of the moment budget in this area (Figure 2). Figure 2 shows the fraction of summed SSE moment to total summed moment including both earthquakes and SSEs, where all events that occur within arbitrary 0.5° bins contribute to the moment sum of that bin. SSEs constitute the majority of the total moment in the Nankai Trough, even if a very conservative shear modulus (1 GPa) is used to constrain the lower bound of SSE moment fraction. Stress orientations
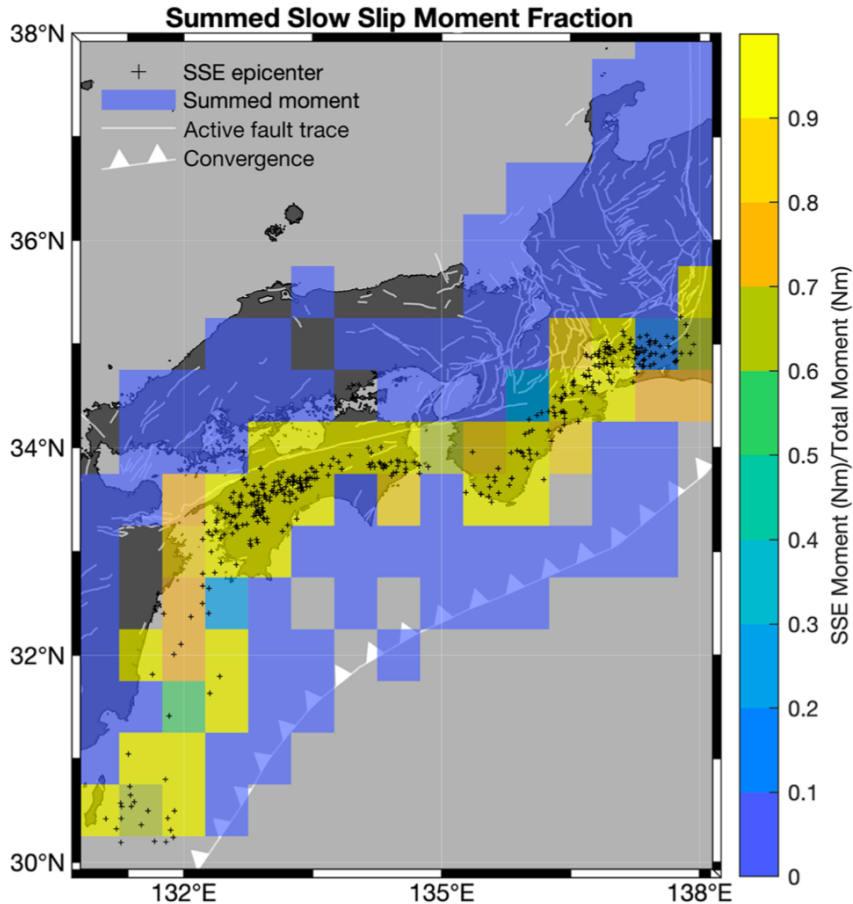
Figure 2. The fraction of summed moment from 1997 to 2015 for arbitrary 0.5° bins of SSEs considered in this study to the total summed moment of earthquakes and SSEs. In each bin that SSEs are pervasive, SSEs constitute the majority of the summed moment. We use a shear modulus of 30 GPa and inversion-derived fault parameters to calculate the moment of slow slip events. Earthquake moments are sourced from the NIED F-Net catalog. Active fault traces from AIST Research Information Database DB095: Active fault database of Japan (2012).

based on focal mechanism inversions estimate the deviatoric stress tensor of the sampled volume; therefore, regional principal stress analyses of the subduction zone interface should include all substantial sources of megathrust slip for which focal mechanisms can be resolved, as different types of fault slip occupy different volumes of the fault interface. SSEs are generally not represented in focal mechanism catalogs and are therefore excluded from stress inversions. To date, no studies have introduced focal mechanisms of slow fault slip in conjunction with earthquakes into spatially variable regional stress analyses to further constrain the tectonic stress field. In this paper, we investigate the stress orientations in the Nankai Trough while considering both earthquakes and slow

fault slip along the subduction interface. We invert SSE focal mechanisms in conjunction with a standard moment tensor catalog to estimate the best-fitting spatially variable stress field and its relationship to the megathrust geometry.

2. Data and Methods

2.1. Focal Mechanism Catalog Processing

We perform stress inversions of 368 short-term SSE focal mechanisms compiled from Sekine et al. (2010), Nishimura et al. (2013), Nishimura (2014), and Kano et al. (2018). Sekine et al. (2010) estimated fault parameters for short-term SSEs occurring from 2001 to 2008 by inverting tiltmeter data for events recorded by at least four stations near the source, resulting in the detection of 54 SSEs with moment magnitudes of 5.4 to 6.2. The SSEs detected by Sekine et al. (2010) have a recurrence interval of approximately 6 months, and each event accommodated approximately 1 cm of slip. Nishimura et al. (2013) detected short-term SSEs from June 1996 to January 2012 along the Nankai Trough, ranging in moment magnitude from 5.5 to 6.3, by identifying displacement reversals in the convergence-parallel component of GNSS (Global Navigation Satellite System) data in addition to estimating fault parameters for the detected SSEs using the nonlinear inversion method of Matsu'ura and Hasegawa (1987). Similarly, Nishimura (2014) applied the method of Nishimura et al. (2013) to data from 352 continuous GNSS stations spanning January 1997 to November 2013 to detect SSEs ranging in moment magnitude from 5.6 to 6.8 and estimate their fault parameters. The data made available by Kano et al. (2018) in the Science of Slow Earthquakes Slow Earthquake Database include the work of Kitagawa et al. (2011, 2012), Itaba et al. (2012, 2013a, 2013b), Itaba, Koizumi, Takahashi, Matsumoto, Kitagawa, Takeda, et al. (2014), Itaba, Koizumi, Takahashi, Matsumoto, Kitagawa, Ochi, et al. (2014), and Ochi et al. (2015, 2016) from reports of the Coordinating Committee for Earthquake Prediction in Japan, which includes detected SSEs and their fault parameters spanning February 2011 to December 2015. SSE focal mechanisms from Sekine et al. (2013a), Kitagawa et al. (2011, 2012), Itaba et al. (2012, 2013a, 2013b, 2013b), Itaba, Koizumi, Takahashi, Matsumoto, Kitagawa, Takeda, et al. (2014), Itaba, Koizumi, Takahashi, Matsumoto, Kitagawa, Ochi, et al. (2014), and Ochi et al. (2015) are derived from models that fix the

fault plane to the plate boundary and define the slip direction as the direction of plate convergence. In contrast, Nishimura et al. (2013) and Nishimura (2014) fix the fault plane to the plate boundary but include slip as a free parameter. Duplicate SSEs detected by more than one study are removed from the compiled SSE catalog. We consider only events within the study area shown in Figure 1. The magnitude of completeness of the NIED catalog is approximately 3.8 (Kubo et al., 2002). In contrast, all SSEs with a magnitude <6 are not expected to be completely recovered by geodetic studies (Nishimura et al., 2013). Given that slow fault slip is expected to follow a Gutenburg-Richter frequency-magnitude distribution (Gutenberg & Richter, 1944; Wech et al., 2010), Figure 2 represents a minimum estimate of the summed SSE moment and a minimum bound on the contribution of SSEs to total moment.

Additionally, we perform stress inversions of 1,229 earthquake focal mechanisms from the National Research Institute for Earth Science and Disaster Resilience (NIED) F-net moment tensor catalog (Okada et al., 2004). The NIED catalog is truncated to have the same temporal span as the compiled SSE catalog, from 22 January 1997 to 30 December 2015. Martínez-Garzón et al. (2016) demonstrated that clustered seismicity in earthquake catalogs biases the results of stress inversions. Therefore, we decluster the NIED earthquake catalog and compiled SSE catalog using SEDA (Lombardi, 2017), a tool for Epidemic Type Aftershock Sequence (ETAS) declustering (Zhuang et al., 2002). The ETAS declustering method of Zhuang et al. (2002) uses a space-time branching process model to distinguish persistent background earthquake activity from aftershock sequences and earthquake swarms that are clustered in time and space, by means of a maximum likelihood estimation. Declustering the catalogs minimizes the inclusion of events triggered by local stress perturbations in our analysis of the stress field surrounding the megathrust. The earthquake catalog is then filtered to contain only events within 10 km of the megathrust, as determined by Hayes et al. (2018), and above 60 km depth. We use a 10 km envelope around the megathrust to avoid including seismicity originating from the MTL and other crustal faults in our analysis of the megathrust stress field.

Binning the data is necessary to investigate spatial variation in the stress field.

Previous studies (Hardebeck & Michael, 2004) have shown that varying interpretations of results from the same focal mechanism data set result from different binning schemes (e.g., Hardebeck & Hauksson, 1999; Townend & Zoback, 2001). Here, we determine bins using k-means++ clustering (Arthur & Vassilvitskii, 2006) of epicenters and require a minimum cluster size of 50 events to minimize the uncertainty associated with the inversion and provide robust estimates of the stress field orientation for the spatial extent of each cluster. We perform three different inversions to explore the effect of SSEs on the
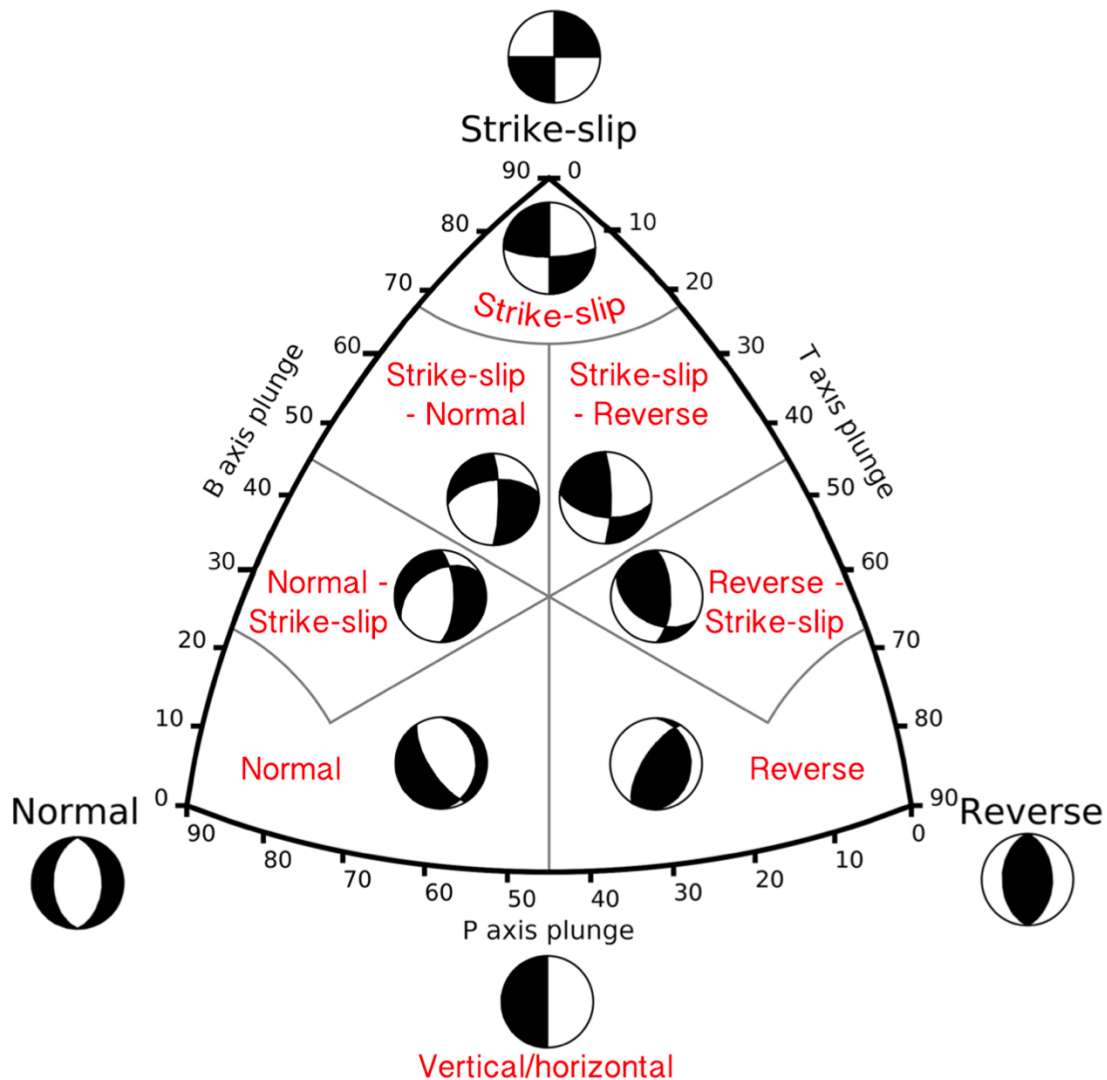

Figure 3. The Kaverina rupture type classification ternary diagram used in this study to visualize the sense of slip, which classifies events into seven types as a function of the plunges of the P, B, and T centroid moment tensor axes computed from the deviatoric moment tensor (modified from Álvarez-Gómez, 2019).

calculated stress field, one containing only earthquake focal mechanisms from the NIED catalog, one containing only SSE focal mechanisms, and one containing both SSE focal mechanisms and earthquake focal mechanisms. The number of clusters for each inversion was selected to generate clusters containing between 50 and 70 events. The filtered earthquake catalog is discretized into 21 clusters with a mean cluster size of 57 events. The compiled SSE catalog is discretized into six clusters with a mean cluster size of 61 events. The catalog containing earthquakes and short-term SSEs is discretized into 30 clusters with a mean cluster size of 53 events. Since each inversion contains clusters of unique dimensions, we facilitate comparison between the earthquake-only and the earthquake-and-SSE inversion results by designating groups of clusters that span similar spatial areas, labeled EI#, for groups from the earthquake-only inversion, and ESI# for groups from the earthquake and SSE inversion. We utilize Kaverina-type rupture classification diagrams (Kagan, 2005; Kaverina et al., 1996) generated by FMC (Álvarez-Gómez, 2019) to visualize the rupture type of focal mechanism data to determine each group. Kaverina-type ternary diagrams classify events into seven rupture types based on the plunges of the P, B, and T centroid moment tensor axes: (1) strike-slip; (2) strike-slip–normal; (3) strike-slip–reverse; (4) normal–strike-slip; (5) reverse–strike-slip; (6) normal; and (7) reverse (Figure 3). Groups were determined by including adjacent clusters that have similar Kaverina classification diagrams (i.e., they include similar focal mechanism distributions).

2.2. MSATSI

We use MSATSI (Martínez-Garzón et al., 2014), a revised version of the SATSI algorithm (Hardebeck & Michael, 2006), to invert focal mechanisms for the best fitting deviatoric stress tensor of each cluster. SATSI is a damped least-squares inversion algorithm based on the Michael (1984) inversion method. In addition to the assumption shared among all stress inversions that fault slip occurs in the same direction as the shear stress vector (Bott, 1959; Wallace, 1951), Michael (1984) assumes the magnitude of shear stress for all fault slip is similar, which simplifies the inverse problem to a system of linear equations. SATSI expands on the method of Michael (1984) by damping the inversion over spatial and/or temporal dimensions to generate solutions with the

minimum complexity necessary to fit the data (Hardebeck & Michael, 2006). A damped inversion allows the model to include heterogeneous solutions for areas where heterogeneity is required by the data and smoothed solutions for areas in which the data do not require heterogeneity by simultaneously inverting for stress orientations in all clusters while minimizing the solution difference between adjacent clusters to better approach a continuous transition between stress states. MSATSI includes minor corrections to the SATSI algorithm and wrapped versions of SATSI for the MATLAB environment (MATLAB, 2018). We select fault planes from auxiliary planes using the method of Vavryčuk (2014), in which the nodal plane with the highest fault instability coefficient is selected as the fault plane; then we perform a 2-D inversion of each data set using MSATSI. Uncertainty is determined by 2,000 iterations of bootstrap resampling of the input data for each cluster, then identifying the bootstrapped data within the 95% confidence intervals.

3. Results

As described in section 2, we perform three main inversions: one that includes only focal mechanisms from earthquakes, one that includes a regional catalog of SSEs in conjunction with earthquakes, and one that includes only focal mechanisms from SSEs. The results of these analyses are shown in Figures 4 and 6 and are not sensitive to different cluster arrangements. We describe our results in terms of the angle between the mean-local megathrust dip for each cluster and the apparent plunge of σ_1 in the dip direction. The plunge of σ_1 is defined as positive if the plunge direction (i.e., the trend) is greater than $\pm 90°$ from the average megathrust dip direction defined by Slab2 (Hayes et al., 2018) for each cluster. The angle of σ_1 to the megathrust and its uncertainty for each cluster are shown in Figures 4c and 4d. Since uncertainties are estimated from bootstrap resampling, higher uncertainties result from groups of slip vectors that are less likely to originate from the same stress field. In general, higher uncertainties in our analysis represent clusters contaminated with focal mechanisms that represent local faulting that differs from regional megathrust activity. We separate clusters from both the earthquake-only and the earthquake and SSE inversions into groups that span similar areas, labeled EI# (Figure 4c) for groups from the earthquake-only inversion and ESI# (Figure 4d) for

groups from the earthquake and SSE inversion. Kaverina-type rupture classification diagrams for all events in each group are shown in Figures 5a and 5b.

When only earthquakes are considered, σ_1 is at intermediate angles to the megathrust ($> 40°$ and $\leq 60°$) in the western Nankai Trough for Clusters 1–3 (Figure 4a) and at high angles to the megathrust ($> 60°$) for Clusters 4–10. Clusters 1–4, denoted as Group EI1 (Figure 4c), predominantly reflect oblique thrust faulting along the megathrust
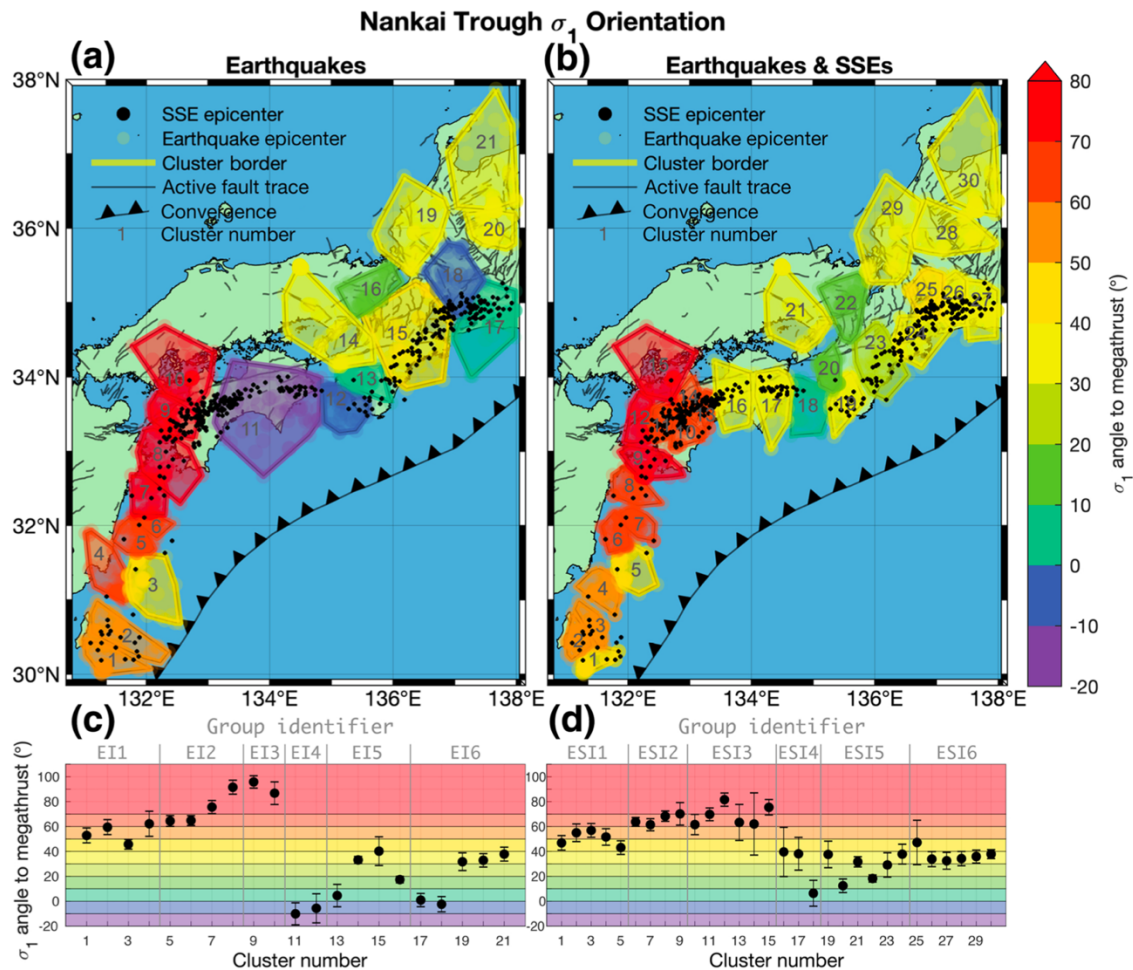
Figure 4. Results of stress inversions for two cases of inputs. (a) Spatial distribution of the orientation of σ_1 to the megathrust for the case of earthquakes only. Cluster numbers are indicated by gray integers. Angles of σ_1 to the megathrust above 80° saturate the colorbar for Clusters 8 and 9. (b) Same as panel (a) but for earthquakes and SSEs. (c) σ_1 to the megathrust versus cluster number for earthquake clusters. Error bars indicate the 95% confidence interval. Groups of clusters that span similar spatial areas between the two inversions are denoted by vertical gray lines and the corresponding group identifier. (d) Same as panel (c) but for earthquakes and SSEs.
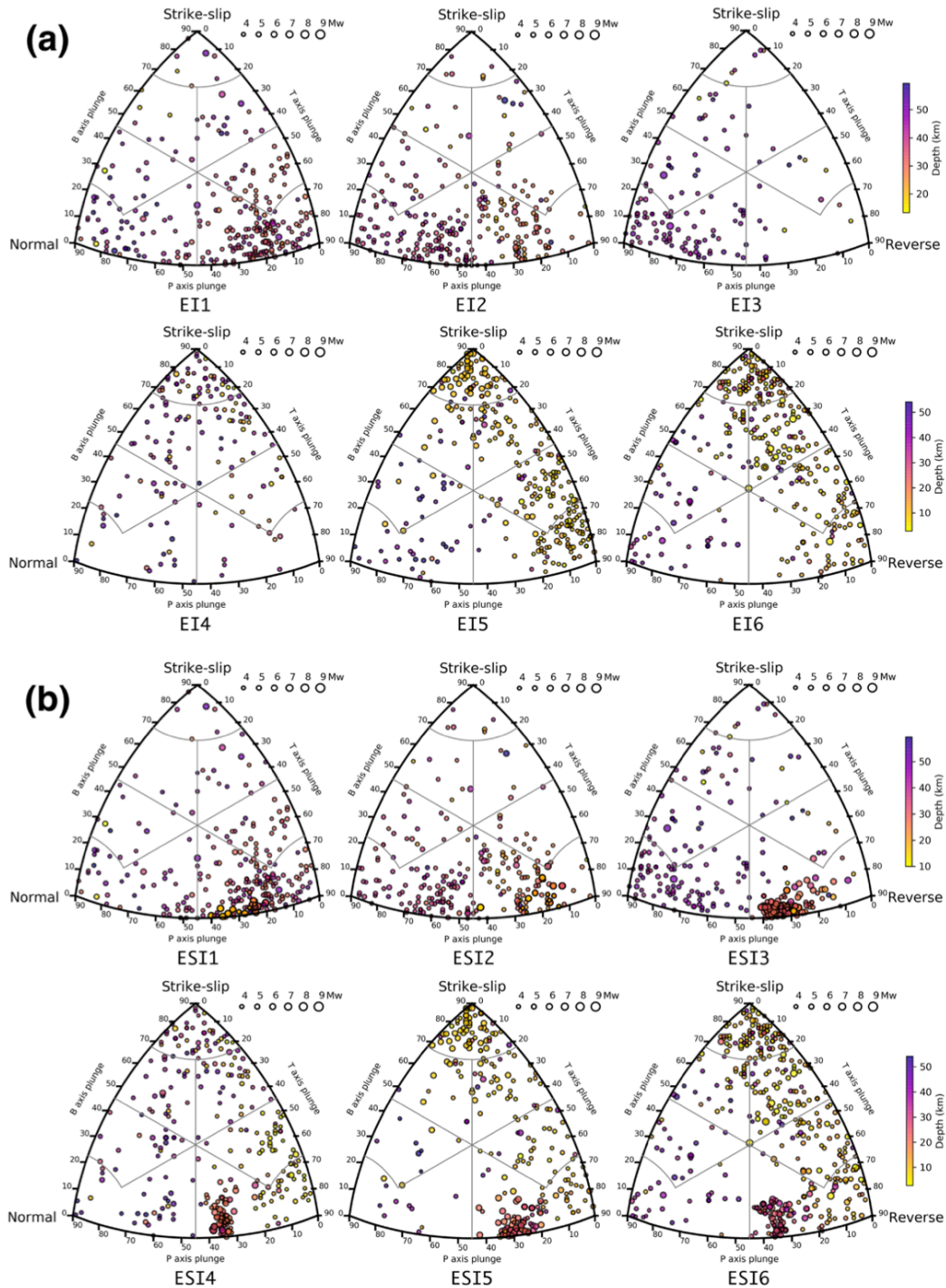
Figure 5. Ternary diagrams of the focal mechanisms comprising (a) Groups EI1 to EI6, identified in Figure 4c, from the earthquake-only inversion, and (b) Groups ESI1 to ESI6, identified in Figure 4d, from the earthquake-and-SSE inversion. Groups that share the same number represent similar spatial areas between the two inversion. SSEs appear as clusters of points. Ternary diagrams generated with FMC (Álvarez-Gómez, 2019). Focal mechanisms are denoted by black-outlined circles filled to indicate event depth in km and sized to indicate the moment magnitude of the event. Refer to Figure 3 for the seven classification types represented in a Kaverina diagram.

16

(Figure 5a), transitioning into a zone dominated by extension to the north. Cluster 4 has greater uncertainty than the surrounding clusters, at ±10.1° for the 95% confidence interval (Figure 4c). Groups EI2 and EI3, composed of Clusters 5–8 and 9–10, respectively, reflect pervasive normal faulting in this area due to the proximity of the Beppu-Shimabara rift (Figure 5a). In Clusters 11, 12, and 18, σ_1 plunges at negative angles to the megathrust. Clusters 11 and 12, grouped as EI4, primarily contain right-lateral strike-slip events, consistent with the sense of slip on the MTL and the sparseness of megathrust seismicity in this area. Cluster 18 includes many left-lateral focal mechanisms, indicative of active local faulting along a network of faults known to host large (Mw ≥ 7.5) crustal earthquakes (Kaneda & Okada, 2008), rather than activity along the megathrust. Clusters 13 and 17 exhibit low angles of σ_1 to the megathrust (> 0° and ≤10°). σ_1 plunges at angles > 10° and ≤50° to the megathrust in Clusters 14 through 16 and 19 through 21.

When short-term SSEs are considered in conjunction with earthquakes, a larger number of events results in increased spatial resolution of the stress field (Figure 4b). The cluster numbers associated with the inversion shown in Figure 4a identify different spatial areas from those shown in Figure 4b; however, the six cluster groups identified for each inversion in Figures 4c, 4d, 5a, and 5b represent similar spatial areas between inversions. σ_1 is at intermediate angles to the megathrust (> 40° and ≤ 60°) for Clusters 1 through 5, denoted as Group ESI1 (Figure 5a), which reflects oblique thrust faulting consistent with the direction of PS-AM convergence. Clusters 6 through 15, which spatially coincide with Clusters 5 through 10 in the earthquake-only inversion, exhibit high angles of σ_1 to the megathrust (> 60°), though σ_1 to the megathrust may be oriented at (<60°) in Clusters 10, 13, and 14 within the bounds of uncertainty (Figure 4d). Similar to Groups EI2 and EI3, Groups ESI2 and ESI3 reflect pervasive normal faulting due to the proximity of the Beppu-Shimabara rift. However, the inclusion of SSEs resolves a thrust component in Group ESI3, which was not resolved in Group EI3. With the exception of Cluster 18, σ_1 plunges at angles > 10° and ≤ 50° to the megathrust in Clusters 16 through 30; however, Cluster 25 contains significant uncertainty of ± 17.8°. Cluster 25 occupies a similar spatial domain as Cluster 18 in the earthquake-only

inversion, an area with active left lateral faulting. Cluster 18 exhibits negative to intermediate angles of σ_1 to the megathrust at the 95% confidence interval. With the inclusion of SSEs, Group ESI4 includes a greater proportion of thrust events rather than being composed of predominately right lateral events as in Group EI4. Both Groups ESI5 and ESI6 experience an increase in the proportion of thrust focal mechanisms over Groups EI5 and EI6.

When only SSEs are considered, σ_1 is well oriented at angles between 39.0° and 51.4° to the megathrust for all clusters (Figure 6). The plunge direction of σ_1 agrees with the megathrust dip direction (i.e., the plunge direction of σ_1 is oriented 180° from the megathrust dip direction) to within ± 12.7° for all clusters except Cluster 4. In Cluster 4,
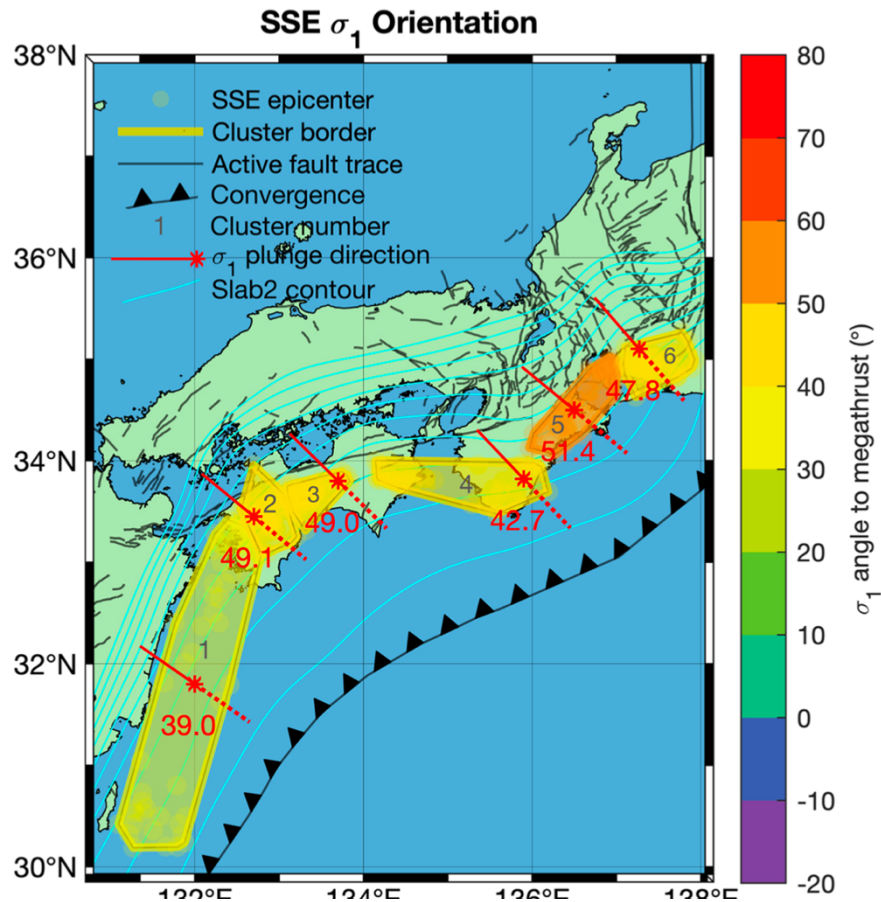
Figure 6. The spatial distribution of the orientation of σ_1 to the megathrust for the case of SSEs only. Clusters numbers are indicated by gray integers. The orientation of σ_1 is denoted by red lines. Red numbers denote the plunge of σ_1 relative to the megathrust, which is also indicated by the colorbar. We use the convention of σ_1 being the most compressive principal stress. 10 to 100 km megathrust depth contours from Hayes et al. (2018) are shown as cyan lines.

σ_1 is oriented 36.6° from the mean-local megathrust dip. All SSEs considered have thrust focal mechanisms. The iterative inversion method of Vavryčuk (2014) evaluates the fault instability coefficient of each cluster based on the stress field shape ratio, the orientation of the fault plane to the principal stress axes, and a range of values for overall fault friction, μ. We allow the value for fault friction to span values from 0.01 to 1.00 by a step of 0.01 to determine the value of μ that requires the highest fault instability based on the input focal mechanisms for each cluster. Table 1 shows estimated values of fault friction for all SSE clusters. The estimated apparent fault friction is lowest for Cluster 5, at $\mu =$ 0.19, and highest for Cluster 3, at $\mu = 0.50$. To consider the effect of different SSE data sets on the stress inversion results, we perform two additional SSE-only

Table 1

SSE Friction Estimates

SSE Cluster[a]	μ
1	0.24
2	0.21
3	0.50
4	0.20
5	0.19
6	0.28

[a]As shown in Figure 6.

stress inversions for the compiled data set that includes slip direction as a free parameter (Nishimura et al., 2013; Nishimura, 2014) and the compiled data set that fixes the SSE slip direction to the plate convergence direction (Itaba et al., 2012, 2013a, 2013b; Itaba, Koizumi, Takahashi, Matsumoto, Kitagawa, Takeda, et al., 2014; Itaba, Koizumi, Takahashi, Matsumoto, Kitagawa, Ochi, et al., 2014; Kitagawa et al., 2011, 2012; Sekine et al., 2010; and Ochi et al., 2015, 2016). However, Nishimura et al. (2013) and Nishimura (2014) use reversals in plate convergence direction to trigger SSE detection; therefore, both SSE data sets do not include SSEs that are not dominantly reversals of plate convergence. The results presented here are not sensitive to the SSE data set, and similar principal stress orientations are observed for each permutation of the SSE data set.

4. Discussion

For the earthquake-only inversion, our stress field estimates are similar to those found by Hardebeck (2015) and Hardebeck and Loveless (2018) and include multiple regions where σ_1 is poorly oriented for megathrust faulting (Figure 4a). When focal mechanisms of SSEs, which account for a large fraction of the total moment release in

the Nankai Trough, are considered in addition to typical earthquakes, σ_1 more closely approaches the range of angles appropriate for thrust faulting. The area of the largest change in the orientation of σ_1 between the two inversions is Groups EI4/ESI4 (Figure 4a and 4b), where the inclusion of slow fault slip results in the angle between σ_1 and the megathrust changing from negative to positive values consistent with thrust faulting. Due to large ($> 30°$) changes in the orientation of σ_1 between the two inversions for Groups EI4 and ESI4, we interpret the negative angles of σ_1 to the megathrust found in our earthquake-only inversion and previous studies (Hardebeck, 2015; Hardebeck & Loveless, 2018) to be products of the low seismicity rate (i.e., few earthquakes are available to constrain the stress state in these areas) and the inclusion of focal mechanisms more closely associated with the MTL (Figures 5a and 5b). In areas where SSEs constitute the majority of the summed moment on a fault, such as the Nankai Trough (Figure 2), the stress field may be poorly constrained if slow fault slip is not considered.

The inclusion of short-term SSEs with earthquakes in the inversion produces high angles of σ_1 to the megathrust in the western Nankai Trough, with improved spatial resolution over the earthquake-only inversion. σ_1 orientations for the western Nankai Trough do not differ significantly between the two data sets (Figures 4a and 4b) and are similar to the results of Hardebeck (2015) and Hardebeck and Loveless (2018). High angles of σ_1 to the megathrust in this region are consistent with prevalent normal faulting from backarc extension (Figures 5a and 5b). The overriding AM of the western Nankai Trough experiences extension from the nearby Okinawa Trough and Beppu-Shimabara rift (Figure 1), in addition to compression from the obliquely subducting PS. Ikeda et al. (2009) proposed stress field segmentation of the MTL on the basis of geological, geophysical, and seismic data, finding the MTL in a state of transpression in the eastern Nankai Trough transitioning to a state of transtension in the western Nankai Trough. Our results support the interpretation of Ikeda et al. (2009) and show that the same stress field segmentation governs faulting in the volume of crust surrounding the megathrust. Our results are consistent with GPS measurements of crustal deformation, which show northwest motion in eastern Nankai Trough transitioning to predominantly southeast

20

motion in the western Nankai Trough (Sagiya et al., 2000). While the inclusion of SSEs does not significantly change the σ_1 orientation in the western Nankai Trough, it does provide insight into the influence of extensional tectonic features on the stress field. The high angles of σ_1 to the megathrust in the western Nankai Trough are a result of the proximity of extensional tectonic features to the subduction margin. This result is further supported by the SSE-only inversion, which results in σ_1 orientations that are optimally oriented for thrust faulting, though the SSE data sets used in this study utilize detection criteria that preclude the detection of SSEs that are not dominantly reversals of the plate convergence direction.

Stress inversions employ catalogs of earthquake focal mechanisms to determine tectonic stress orientations, and since most focal mechanism catalogs exclude SSEs, aseismic slip is not typically included in stress inversions. In regions like the Nankai Trough, SSEs occur both downdip and updip of the seismogenic zone, so their inclusion in stress inversions increases the spatial extent of the data and can be used to determine the stress field in areas where typical earthquakes are sparse or absent. For example, future studies utilizing seafloor observation systems to detect shallow seismicity and slow fault slip may be capable of resolving the megathrust stress field to the trench. Further, future studies may explore methods of constraining the fault slip vector of SSEs beyond convergence-parallel displacement reversals to better constrain the megathrust stress state. Additionally, the resolution of stress inversions is often data limited, and the number of events per bin is selected to achieve a balance between the desired spatiotemporal resolution and model uncertainty. The inclusion of slow fault slip in stress inversions increases the quantity of data, which may improve the model uncertainty and resolution. To conclude this study, we explore the implications of results from the SSE-only inversion.

4.1. Implications for SSEs

Our results show that the maximum compressive principal stress orientations of all SSE clusters (Figure 6) are 39.0°–51.4° from the megathrust, well oriented for megathrust faulting. Optimally oriented faults with typical friction coefficients make

angles between ~25° and ~45° to σ_1 and are thought to have strengths similar to their surroundings. However, some faults are observed to operate at angles to σ_1 that are outside this range. Such faults are called non-optimally oriented and are thought to be much weaker than their surroundings because they slip at low applied shear stress. Our results imply that the strength of the megathrust in regions hosting slow slip is similar to the surrounding material. SSEs often occur in regions of elevated V_p/V_s ratios which are attributed to elevated pore fluid pressures in the SSE source and surrounding regions (Audet & Bürgmann, 2014). Additionally, the extreme sensitivity of slow fault slip to small magnitude dynamic stress changes imparted from earthquakes and tides implies that the megathrust itself is weak in regions hosting slow slip (e.g., Hawthorne & Rubin, 2010; Thomas et al., 2012). These observations are consistent with our results and imply that the megathrust and its surroundings operate at low deviatoric stresses due to the presence of pressurized fluids.

Our fault stability analyses reveal overall fault friction coefficients that are lower than those predicted by Byerlee's law (Table 1). Estimated friction coefficients are determined from the deviatoric stress tensor and are independent of the pore fluid pressure in the SSE source region assuming the same pore fluid pressure modulates each principle stress (Sibson, 1985). As such, the low coefficients of friction for all SSE clusters suggest that frictionally weak materials are present in the SSE source region in the Nankai Trough (e.g., French & Condit, 2019).

To further explore the implications of our results, we consider the principal stress shape ratio and the principal stress orientations (Figure 7), recovered from stress inversions of each cluster, in conjunction with the overall fault friction coefficient to estimate the effective differential stress required for frictional activation of areas that host SSEs. Zones of accumulated fault slip may be considered isotropic for the sake of simplicity or due to the assumption that successive slip has randomized the orientations of pores (or cracks) in the fault core (Healy, 2012). The governing assumption of isotropic poroelasticity is that fluids occupy equant pores and therefore the principal stresses are modulated by the pore fluid pressure, P_f, such that the effective principal

22

Mohr-Coulomb Failure Conditions Constrained by Fault Instability
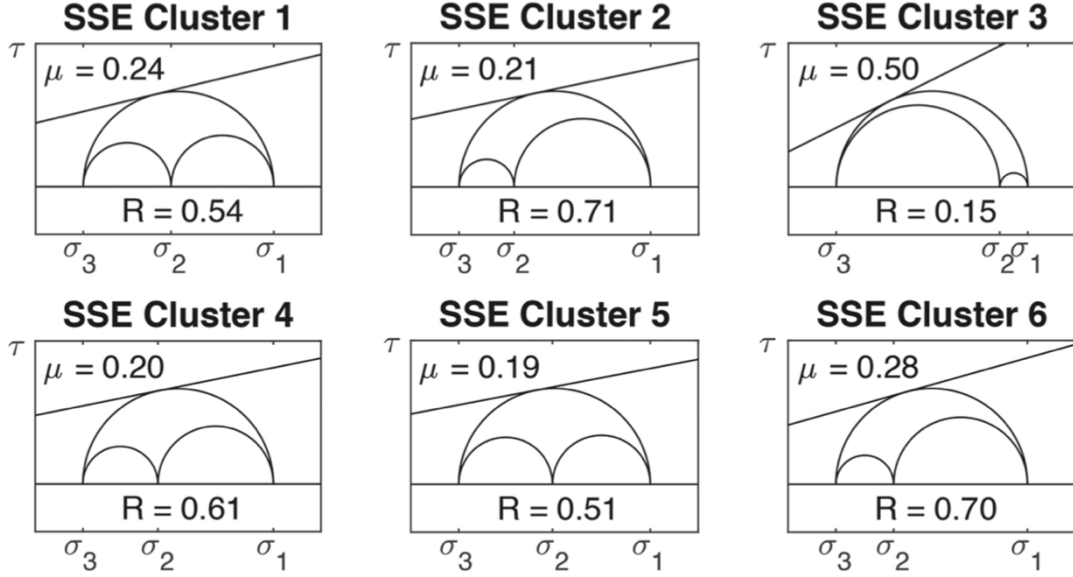
Figure 7. Mohr-Coulomb failure conditions for the SSE clusters shown in Figure 6 determined by iterative stress inversions with a fault instability constraint. R is the shape ratio (Gephart & Forsyth, 1984), where $R = (\sigma_1 - \sigma_2)/(\sigma_1 - \sigma_3)$.

stresses are $\sigma'_1 = \sigma_1 - P_f$, $\sigma'_2 = \sigma_2 - P_f$, and $\sigma'_3 = \sigma_3 - P_f$. In this case, frictional reactivation of a fault with static coefficient of friction, μ, is expressed as the frictional failure envelope, $\tau = \mu(\sigma_n - P_f)$, where τ and σ_n are the shear and normal stresses, respectively.

The frictional failure envelope may be expressed in terms of the principal effective stresses for the 2-D case as

$$(\sigma'_1 - \sigma'_3)\sin(2\theta) = \mu[(\sigma'_1 + \sigma'_3) - (\sigma'_1 - \sigma'_3)\cos(2\theta)] \qquad \text{(Eq. 1)}$$

where θ is the angle between σ_1 and the fault (Sibson, 1985). The effective differential stress required for reactivation of a thrust fault at depth, z, with near-vertical σ_3 is expressed as

$$(\sigma'_1 - \sigma'_3) = \frac{\mu(\cot\theta + \tan\theta)}{1 - \mu\tan\theta} \rho g z(1 - \lambda_v) \qquad \text{(Eq. 2)}$$

where ρ is the average rock density, g is the gravitational acceleration, and λ_v is the pore-fluid factor (Sibson, 1990). The pore-fluid factor is defined as the ratio of the pore fluid pressure to the vertical stress, $\lambda_v = P_f/\sigma_3$. We confirmed that σ_3 is near-vertical and calculated the effective differential stress required for reactivation of each SSE cluster using the mean cluster depth, an average crustal density of 2.7 g/cm^3, a near-lithostatic pore-fluid factor of 0.99 (Bürgmann, 2018; Gao & Wang, 2017), and parameters recovered from the stress inversions: angles from σ_1 to the megathrust, the relative principal stress magnitudes, and the coefficient of friction. Additionally, we solve for the absolute effective maximum and minimum principal stresses by substituting Equation 2 into Equation 1.

The effective differential stress required for frictional reactivation for each SSE cluster ranges from 3.2 to 12.2 MPa, which is considerably weaker than observations and models of differential stress in the lithosphere (Scholz, 2015; Zoback et al., 2002). Further, we find the maximum effective principal stress to be on the order of 10–20 MPa and the minimum effective principal stress to be on the order of 6–9 MPa, yielding values of effective mean stress ranging from 7.9 to 13.7 MPa. Overall, our findings suggest that the SSE source region is composed of intrinsically weak materials (e.g., $\mu = 0.19$–0.50) at high pore fluid pressures, resulting in slow fault slip due to absolute principal stresses on the order of several to tens of MPa.

5. Conclusions

We determine the deviatoric stress field of the Nankai Trough megathrust and interpret the results in the context of the regional tectonics. We find principal stress orientations in the central and eastern Nankai Trough that are consistent with a convergent margin and faulting on the megathrust and principal stress orientations in the western Nankai Trough that are consistent with subduction of the PS beneath an overriding plate that hosts widespread extension in the forearc sliver. Short-term SSEs with a magnitude <6 are not completely represented by our compiled catalog, and shallow SSEs are poorly recovered by current geodetic studies. Given improved methods and instrument coverage that allow the detection of long-term, shallow, and low-

magnitude SSEs, future stress analyses may reveal a more complete view of active tectonic stress fields. Our conclusions are summarized below.

1. Stress inversions typically employ catalogs of earthquake focal mechanisms to constrain regional stress orientations. In the Nankai Trough, SSEs release greater summed seismic moment than earthquakes for the same time period and have well-resolved focal mechanisms. As such, SSE focal mechanisms can be used to augment traditional focal mechanism catalogs resulting in better constrained estimates of stress field orientations and increased spatial resolution.

2. We find that creeping areas of the Nankai Trough subduction zone are well oriented for failure when both earthquakes and SSEs are considered in the inversions. Our results suggest that areas hosting SSEs and other slow fault slip may appear to have misoriented stress fields if slow fault slip is not included in the stress analysis.

3. The principal stress orientations of clusters of SSEs are well oriented for frictional failure with σ_1 at angles of 39.0° to 51.4° from the megathrust. From this we infer that the strength of the megathrust is similar to its surroundings. Low V_p/V_s ratios in the SSE source region and the modulation of slow slip by small applied stresses suggest the megathrust and surrounding faults operate at low deviatoric stresses.

4. Further, these angles imply friction coefficients between 0.19 and 0.50, suggesting that intrinsically low-strength materials are present in the SSE source region and surroundings in the Nankai Trough. Low fault friction coefficients and near-lithostatic pore fluid pressures in these regions imply low effective differential stress ($\sigma'_1 - \sigma'_3 = 3.2$–12.2 MPa) and effective mean stress (($\sigma'_1 + \sigma'_3$) / 2 = 7.9–13.7 MPa).

CHAPTER III

A COMPREHENSIVE ANALYSIS OF MICROSEISMICITY, DEFORMATION, AND FAULT STRUCTURE OF THE RATTLESNAKE RIDGE LANDSLIDE

From Newton, T. J., Thomas, A. M., Toomey, D. R., Delong, S., Pickering A. J., and Malone, S. (in prep.). A Comprehensive Analysis of Microseismicity, Deformation, and Fault Structure on the Rattlesnake Ridge Landslide. *Journal of Geophysical Research: Earth Surface.*

1. Introduction

Slow-moving landslides may creep intermittently or continuously for days or centuries before potentially failing catastrophically, which can result in dammed rivers or impacts on the built environment. The movement of slow landslides is the result of both aseismic creep and microearthquakes from brittle fracturing that collectively comprise the displacement of the landslide body (Gomberg et al., 1995). In some cases, precipitation or increased pore fluid pressure triggers accelerated rates of landslide movement (Corominas et al., 2005; Iverson & Major, 1987; Prior & Stephens, 1972), however not all landslides respond to these conditions (van Asch, 2005; Massey et al., 2013), suggesting the geological setting of a landslide is a major controlling factor of the failure mechanisms driving mass movement. The processes governing landslide failure are analogous to the failure processes on crustal faults (Gomberg et al., 1995), thus seismically-monitored slow landslides with exposed slip surfaces present a unique opportunity to study the fault that hosted the recorded seismicity. In this study, we examine seismic recordings from a slow-moving landslide in Washington and the resulting topographic deformation to interpret the relationship between landslide seismicity and associated fault.

The Yakima Fold and Thrust Belt (YFTB) extends throughout central Washington and consists of a series of east-west and northwest-southeast trending anticlines comprised of primarily Columbia River Flood Basalt group (17.5-6.0 Ma) lithologies separated by wide synclinal valleys filled with suprabasalt sedimentary deposits (Blakely

et al., 2011). Near Union Gap, WA the N-S oriented Yakima River forms a water gap separating the Ahtanum Ridge (west) from Rattlesnake Ridge (east); both ridges comprise one of the major anticlines in the YFTB. In October of 2017, several North-South trending, meter-deep cracks were discovered in the westernmost extent of Rattlesnake Ridge (immediately adjacent to Hwy 82) north of a quarry operated by Columbia Asphalt and Gravel (Figure 1A). By December of 2017, the cracks had grown to ~80 m deep and delineated the eastern edge of a large (~3 million cubic meters) landslide mass known as the Rattlesnake Ridge Landslide (RRL) (Norrish, 2018).

The RRL is classified as a translational landslide because motion is accommodated along side-bounding strike-slip faults and a basal slip surface along which the slide body is translated (Hungr et al., 2014). Its basal slip surface is thought to coincide with the Selah sedimentary interbed, a nearly planar layer of weak materials such as clays, silts, and sands that marks the boundary between the underlying Umatilla and the overlying Pomona member of the Saddle Mountain basalt group (Norrish, 2018; Reidel et al., 2013). This inference is based on observations of the slide morphology and exposures of the sedimentary interbed and overlying basalt in the quarry headwall (Figure 1A). The eastern edge of the RRL is delineated by a nearly vertical fracture zone thought to penetrate down to the Selah sedimentary interbed that accommodates both left-lateral motion and subsidence as the slide body moves south (Figure 1B). Large tension cracks are visible in the north, near the head of the slide body (Figure 1A) and fault structures that accommodate slide body deformation are particularly abundant in the eastern section of the slide body (near UGAP6, Figure 1A). While geometrically unconstrained, the western slide boundary is also diffuse and likely coincides with the exposure of the Selah interbed. An independent firm monitoring slide activity reported that the slide body, which largely moves in the southerly downhill direction towards the quarry pit (Figure 1A), accelerated throughout late 2017 and early 2018 reaching peak speeds of 0.64 m/wk (Figure 1B), two orders of magnitude faster than typical plate boundary faults. As of July 2021, the slide had slowed considerably to ~0.04 m/wk.
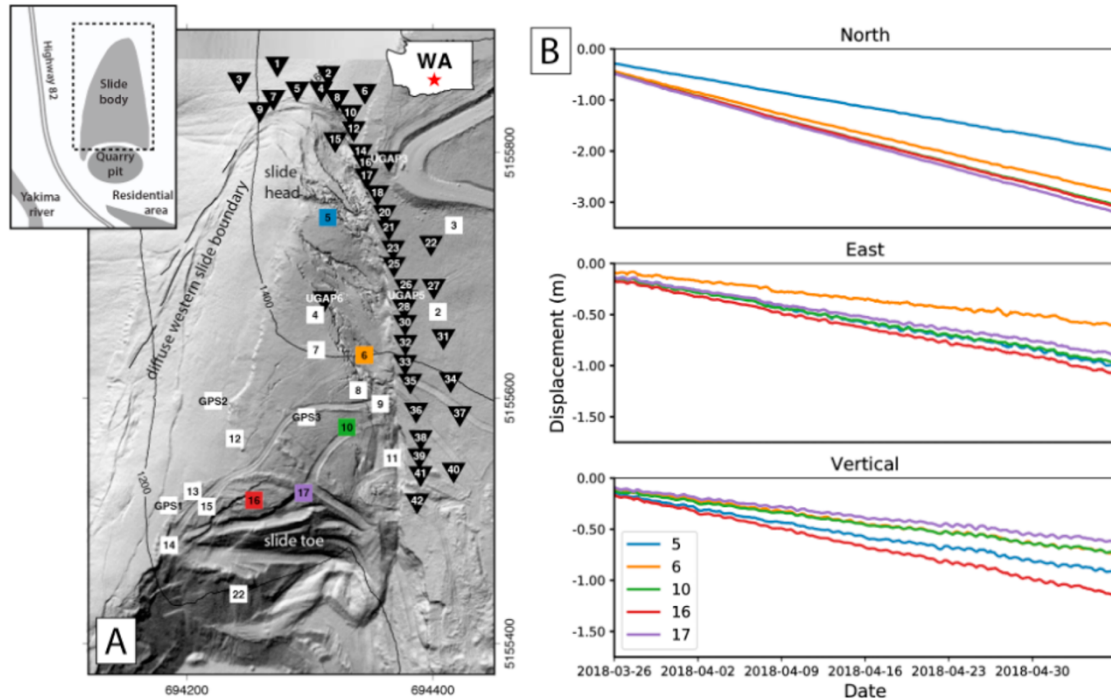
Figure 1. Map view of slide body and displacement history. (a) Map view of the slide body. Nodal seismometer locations are shown as black triangles labeled with their corresponding station ID. Squares are prism locations that were repeatedly surveyed by a total station for some portion of the deployment period and are labeled by their corresponding station ID. The colored squares correspond to the time series shown in Figure 1b. Insets show location of the RRL within Washington State and nearby features of relevance including the quarry pit and residential area. (b) The three component deformation data from a six-week period for select stations shown in Figure 1a. Note the difference in y-scale.

The Pacific Northwest Seismic Network (PNSN) installed four telemetered seismic stations near the landslide on January 2, 2018 for risk reduction monitoring with the hope that if the landslide accelerated to catastrophic failure, the increasing frequency of microseismicity would act as a warning signal. For safety reasons, these instruments were located some 10s-100s of meters from the landslide (UGAP3 in Figure 1A and UGAP1 and UGAP2, not shown). On 22 Jan. 2018, two more seismographs (UGAP5 and UGAP6, Figure 1A) were established next to and on the landslide body. Realtime data were monitored for spectrograms, event counts, and real-time seismic amplitude. Over the course of the next few months, many tiny individual seismic events were recorded on these instruments; however, there were few cases where the same event would be

28

recorded by more than two instruments, thus making detailed locations of events impossible.

These limitations of the temporary PNSN stations motivated us to deploy a temporary network of 40 three-component nodal seismometers on and surrounding the RRL for four months. The resulting dataset has abundant small magnitude seismic events and anthropogenic noise from surrounding transportation corridors. In this work, we detect microseismic events, associate phase arrivals, locate events, and present a comprehensive analysis of the microseismicity contained in this dataset. The RRL presents a unique opportunity to study coincident microseismicity and deformation at a spatial and temporal scale that is unprecedented on crustal faults because of the unique RRL geometry in which one of the fault structures that hosted the recorded seismicity was continuously exposed during progressive deformation. We analyze the geometry of the exposed slip surface and the spectral properties of microseismic events to explore the influence of fault geometry on earthquake character.

2. Data and Methods
2.1. Seismic Deployment

Beginning on March 13, 2018, we installed 38 5-Hz three-component nodal seismometers around and on the RRL. Owing to concerns over continued site accessibility and safety, our deployment was concentrated on the eastern and northern portions of the slide body. Instruments recorded data at a 250 Hz sampling rate for their 30-day battery life and were then replaced with charged instruments, which resulted in continuous seismic monitoring for a four-month period (until July 8). In early April we deployed two additional instruments on the slide body (Figure 1A) which operated until the end of the deployment. A significant amount of anthropogenic noise is present in the resulting seismograms, which is unsurprising given that the site is proximal to highway traffic, active railways, and the approach route to a regional airport. Earthquake signals of interest typically manifest in the 20 to 60 Hz frequency band, so we apply a 4th order bandpass filter between these frequencies to the seismograms to mitigate the effect of noise sources.

Analysis of waveforms recorded in early March reveals a dataset rich in small magnitude earthquakes. As an example of this, Figure 2a shows a one-minute record section of vertical component seismic data from five stations in the network. These microseismic events manifest as near-simultaneous amplitude changes on multiple stations and are abundant in the 60 s record shown. Some events are small and are recorded on only a few stations whereas others are recorded across the network. Because of the highly attenuating nature of the slide body, most of these events likely emanate from the eastern slide boundary which accommodates both left-lateral motion and subsidence.

2.2. Phase Detection

Off-the-shelf deep-learning phase picking models (Mousavi et al., 2020; Ross et al., 2018; Zhu & Beroza, 2019) do not predict accurate phase arrival times for RRL seismic data. The poor performance of these neural
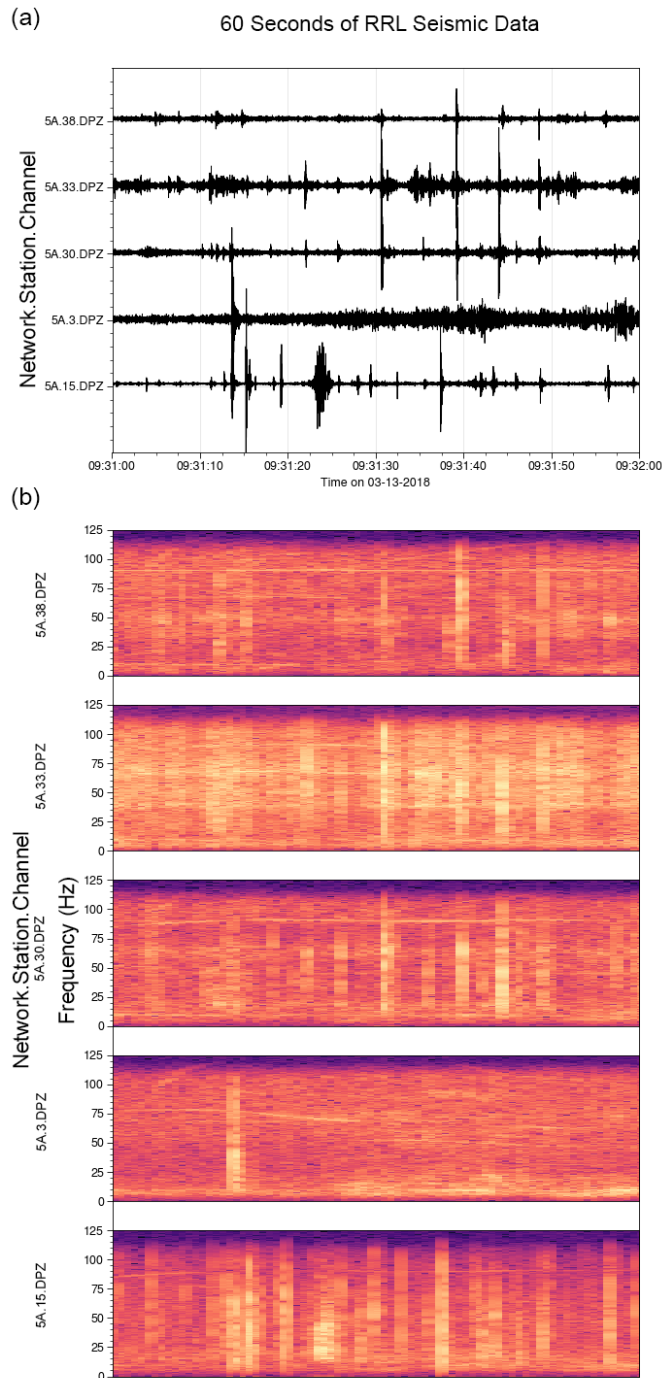
Figure 2. (a) One minute of seismic recordings from the vertical component of five selected nodal stations on March 13, 2018. (b) Spectrograms for the same period and stations as in Figure 2a.

networks, which are pretrained on earthquakes, is due to the waveform dissimilarity of the microseismic events compared to ordinary earthquakes. In particular, microseismic events at Rattlesnake Ridge exhibit a short event recurrence interval (~2.1 seconds on average), low signal-to-noise ratios, and spectral depletion of low frequencies compared to earthquakes (Figure 2a, 2b).

To address this problem, we developed a phase detection and association algorithm to identify microseismic events, consisting of a convolutional neural network, a density-based clustering algorithm, and a decision tree. We trained and fine-tuned a U-Net (Ronneberger et al., 2015) convolutional neural network to predict phase arrival time onsets in time series from 8,570 manually picked P-wave arrival times and 8,570 examples of noise. Our U-Net phase detector takes in 0.48-second chunks of time series data (120 samples at 250 Hz) in a 2-by-120 array of the log-modulus transform (John & Draper, 1980), where the first row contains the natural logarithm of the absolute value of each time series sample, and the second row contains the sign of each time series sample. Training labels (signal or noise) are encoded as 1-by-120 arrays that represent a Gaussian probability distribution centered on the manually-picked arrival time with a standard deviation of 2.5 samples. The phase detection model output is a 1-by-120 array containing the model prediction for each time series sample, where each prediction is a value between 0 and 1. Only arrival times with a prediction value above 0.23 are considered. This target threshold of 0.23 was determined from the model F1 score bias-variance tradeoff curve.

2.3. Phase Association

Most association methods require travel times derived from a velocity model of the region. To associate phase arrivals without a robust velocity model for this area, we take advantage of the pseudo-linear network geometry to create a distance proxy by arranging stations in their N-S order along the main scarp. Using ordered stations during phase time clustering has the effect of clustering phases in space and time, thus forming the basis of a simple association algorithm. We expanded on the idea of clustering as an associator by developing an association algorithm that utilizes the pretrained phase

31

detection model, a density-based clustering algorithm, and a manual decision tree (a set of rules) to build a catalog of events. We assigned phase arrivals to distinct events by traversing the time series data from every station in 5-second windows. In each window, the U–Net arrival time predictions were used as input for our phase association algorithm.

The first step of the association algorithm clusters the phase time predictions using DBSCAN (Ester et al., 1996), from a set of parameters fine-tuned for five-second windows (epsilon=0.73, minimum samples=3). The five-second window duration was chosen to include multiple events in each window. Next, the median phase time of each cluster is calculated and used to define three time windows as inputs into the phase detection model for revised phase time predictions. The three time windows are each 0.48 seconds in duration, centered on the median cluster phase time, 0.2 seconds before the median cluster phase time, and 0.2 seconds after the median cluster phase time. Duplicate phase time predictions are removed, then the phase times are clustered again. Clusters are then processed according to a set of rules:

- If there are multiple phase time predictions on the same station in the same cluster, keep only the phase time prediction closest to the cluster median.
- If a cluster has less than 5 members it is dissolved.
- All phase time predictions greater than 0.14 seconds from the cluster median are removed from the cluster.
- All phase time predictions greater than 3 stations from another phase time prediction (according to the station ordering described above) are removed from the cluster.
- Clusters are merged if they contain phase time predictions that occur within 0.14 seconds of another cluster's median and within 3 stations from another phase time prediction in that cluster.
- Finally, each phase time prediction that does not belong to a cluster is checked against the same temporal and spatial thresholds and assigned to that cluster if it is nearby.

Clusters are reprocessed using the same rules until the quantity and size of clusters are stable. Each final cluster represents an event and each cluster's members represent the phase arrival times comprising that event.

2.4. Event Location

We determined event locations using the method of Battaglia & Aki, 2003 based on corrected seismic amplitudes. The location method approximates the seismic amplitude as a function of source distance, modeled as the decay of seismic waves in a homogeneous medium, and is shown to be effective for locating various source types (Battaglia & Aki, 2003). In the absence of a velocity model for this region, we used the nearest time-averaged shear-wave velocity measurement (VS30) of 0.58 km/s (McPhillips et al., 2020) and converted it to the P-wave velocity at the surface using the global average crustal Vp/Vs ratio of 1.74 (Kennett et al., 1995) as a scaling factor, for a P-wave velocity of 1.02 km/s. The resulting event locations are precise despite the absence of a robust initial seismic velocity model, and the event locations are used to inform our analysis of event sources.

2.5. Source Analysis

We analyzed the source spectra for each event by calculating the median instantaneous frequency from the Hilbert transform of all phases that comprise an event. The instantaneous frequency serves as a measure of the dominant frequency content of an event. Additionally, we estimated the size of each event from the source amplitude, which we extracted from the event location method of Battaglia and Aki (2003).

2.6. Terrestrial LiDAR

We conducted terrestrial lidar scans of the landslide body and surrounding area in June 2019. Over a period of three days, we traversed the landslide with a RIEGL laser scanner to collect a point cloud representation of the landslide geometry. The data set captures the complex geometry of the eastern bounding scarp and the landslide body. We

calculate the point cloud roughness, mean curvature, planarity, and verticality over different length scales using CloudCompare.

3. Results

We detected 43,661,881 microseismic phase arrivals with our phase detection algorithm over the 17-week span of the nodal seismometer deployment. We then used our phase association algorithm to assign each phase to an event (Figure 3a), resulting in 4,837,460 detected events (Figure 3b) with an average of 9 phases per event. We detected over 10,000 microseismic events per day for the duration of the experiment, peaking at around 70,000 events per day in mid-to-late May. The rate of event detections stayed below 40,000 events per day for the first 52 days of the experiment, then remained above 40,000 events per day for a period of 35 days before fluctuating between approximately 27,000 and 57,000 event detections per day for the remainder of the experiment, as shown in Figure 3b.
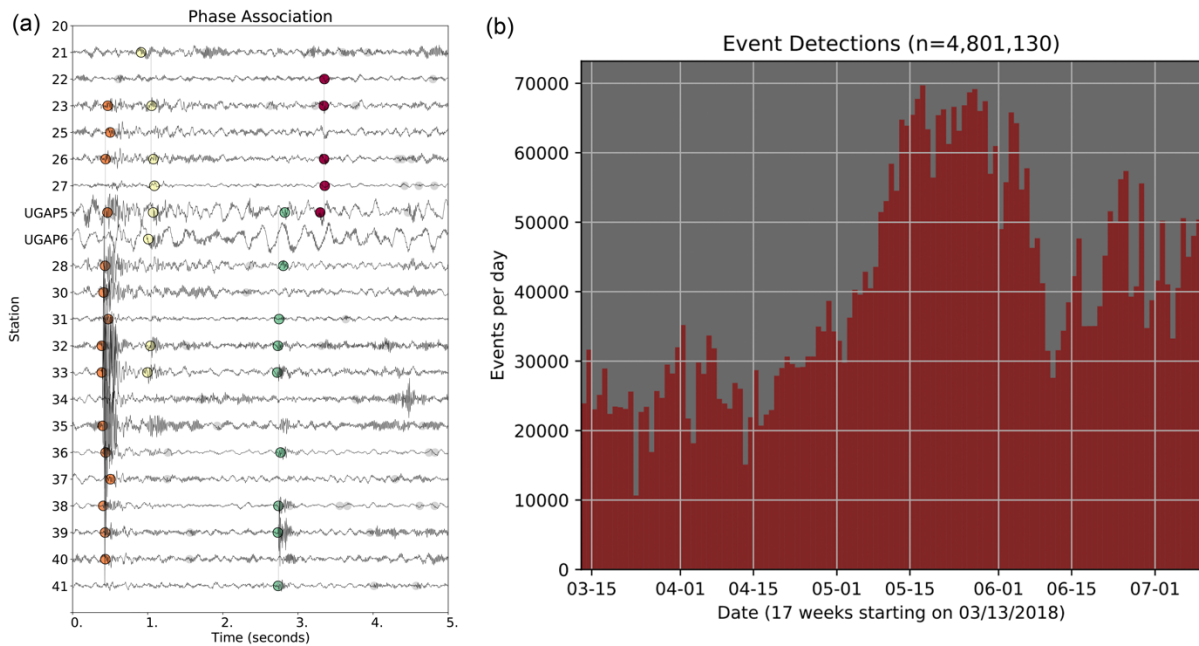
Figure 3. (a) plot of associated picks (colored circles with black outline) and discarded picks (gray circles) from phase association algorithm for a 5-second window, (b) histogram of event detections per day over the duration of the nodal seismometer deployment.

Locations for the 24,115 events detected on March 13, 2018, the first day of the experiment, show strong clustering of event hypocenters on the eastern extent of the landslide body. The spatial distribution of event locations closely follows the spatial extent of the vertical scarp that is exposed on the eastern and northern boundaries of the landslide body (Figures 4a, 4b). The eastern boundary of event locations resembles a step-like or combed shape with a couple regions of diffuse events, however the western extent of event locations is diffuse across the entire length of the landslide. The majority of microseismic events occur shallower than 70 m in depth, as shown in Figure 4a and 4b.
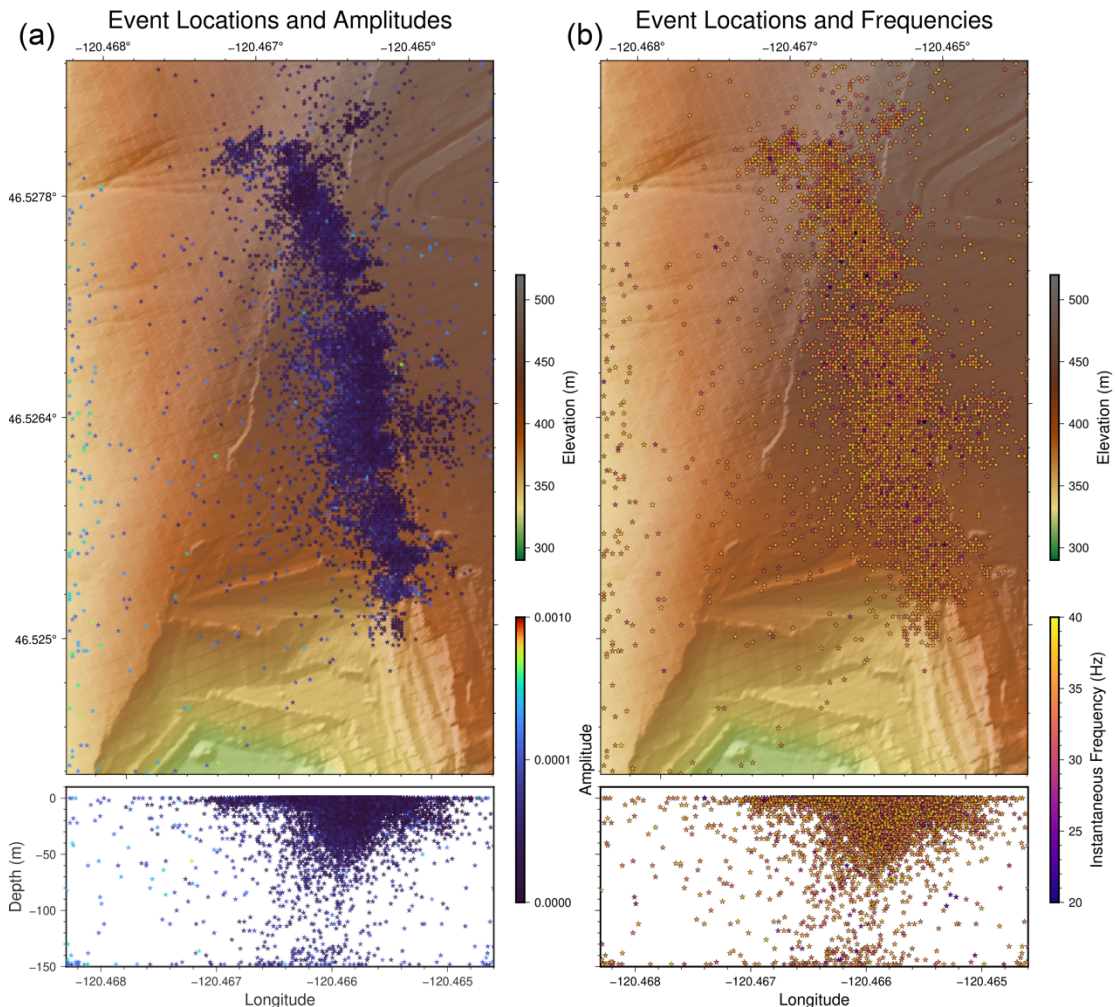
Figure 4. (a) Event locations for the 24,115 events detected on March 13, 2018, the first day of the experiment, are marked by stars colored by the event amplitude. The upper panel shows event hypocenters in the latitude-longitude plane, and the lower panel shows event hypocenters in the depth-longitude plane. (b) Same as Figure 4a, but colored by the median instantaneous frequency of all phases for each event.

The spatial distribution of source amplitudes for the events detected on March 13, 2018 is shown in Figure 4a, alongside the spatial distribution of source instantaneous frequencies for the same events (Figure 4b). Additionally, the distribution of source instantaneous frequencies for all events on March 13, 2018 is shown in Figure 5a, with a median of 34.5 Hz, alongside the same distribution for May 17, 2018, the date with the most event detections, with a median of 34.9 Hz. The distribution of source amplitude for all events detected on March 13, 2018 is shown in Figure 5b.
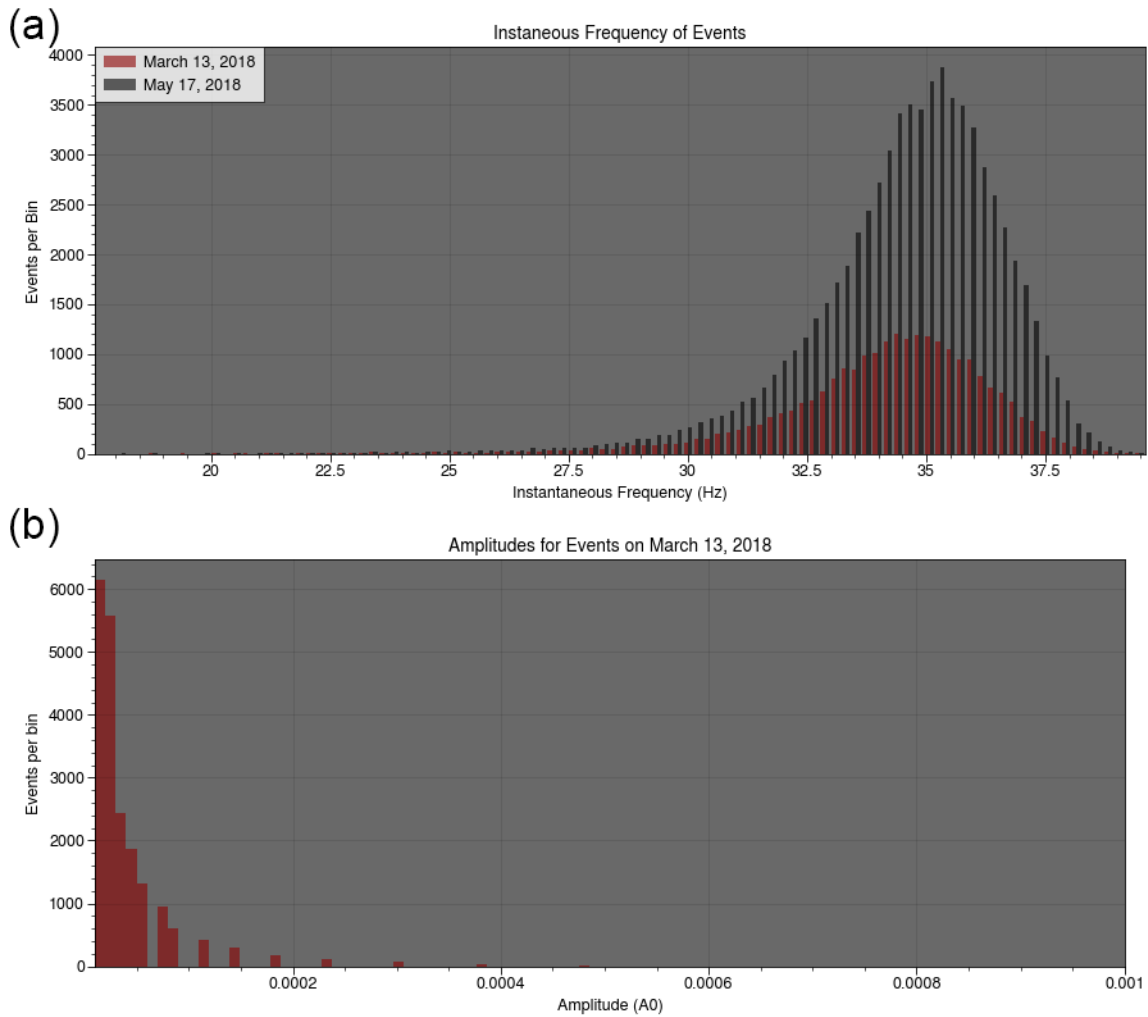
Figure 5. (a) Histogram of the instantaneous frequency of the 24,115 events detected on March 13, 2018, the first day of the experiment, and the 70,412 event detections on May 17, 2018. (b) Histogram (100 bins) of amplitudes for all detected events on March 13, 2018.
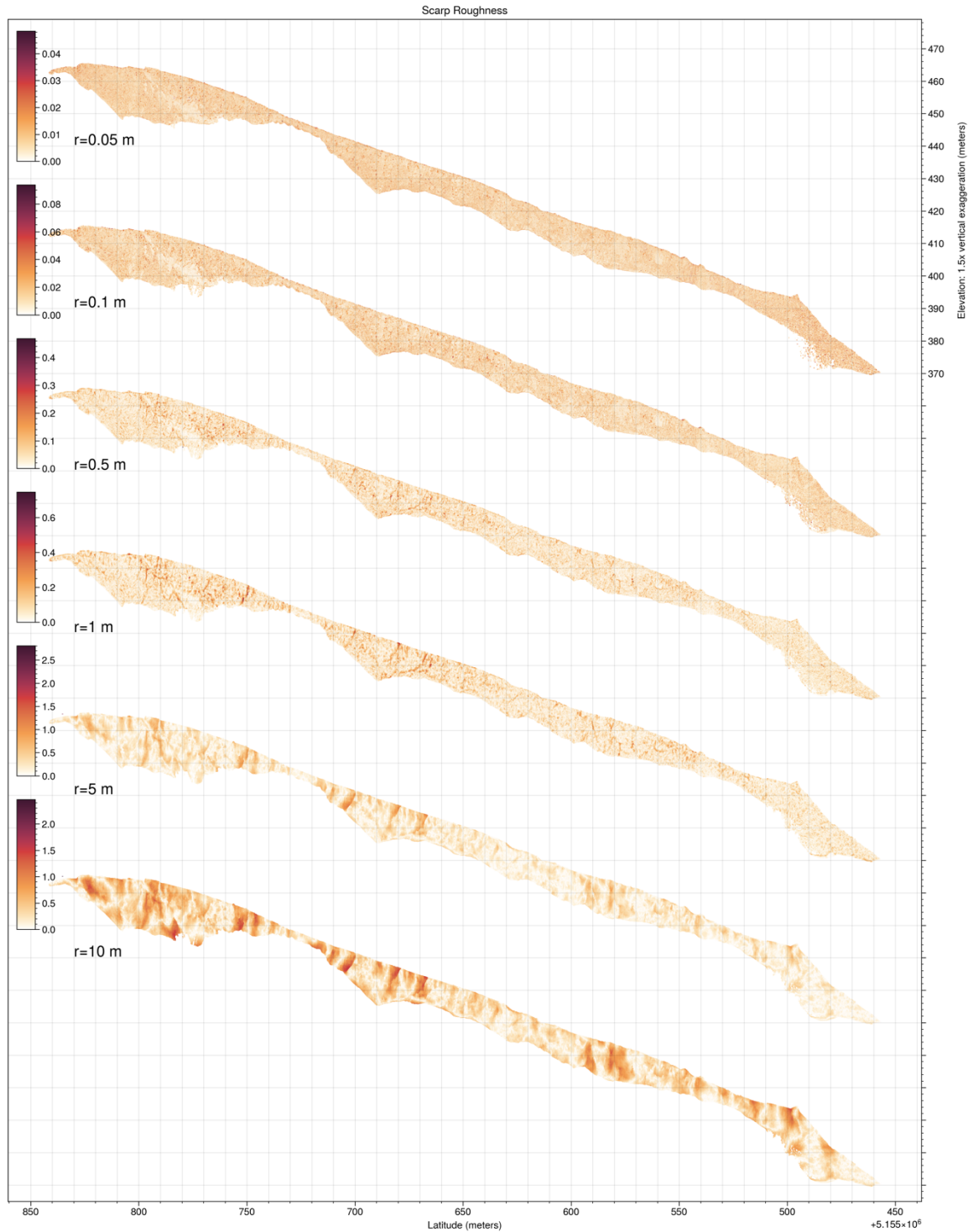
Figure 6. Scarp roughness for neighborhood radii of 0.05 m, 0.1 m, 0.5 m, 1 m, 5 m, and 10 m. The scarp trends approximately North-South and is plotted in the latitude-elevation plane as it would appear from standing on the landslide body looking east. The head of the landslide is on the left and the toe of the landslide is on the right. The scarp elevation in meters for the uppermost plot is shown on the right. The color of each plotted scarp point represents the local roughness at that point for the specified neighborhood radii. Note the different range of each colorbar, representing the range of roughness values in each analysis, expressed in meters.

37

We calculated the local roughness of the terrestrial lidar point cloud at varying radii to characterize the topographic heterogeneity of the RRL scarp at different length scales. We used radii of 0.05 m, 0.1 m, 0.5 m, 1 m, 5 m, and 10 m to calculate the local scarp roughness for each point in the point cloud, considering all points within the specified radius (Figure 6). Our finest scale roughness analysis (r=0.05 m) highlights fine surface roughness on the scale of several centimeters, like the edges of basalt columns and the surface of fractured basalt (Figure 7). The 0.1 m roughness analysis is effective at highlighting the edges of columnar basalt structures that are visually apparent along the scarp (Figure 7). Our 0.5 m roughness analysis of the scarp shows high roughness values along the faces of the columnar basalt, and along small ridges of the scarp (Figure 7). The 1 m roughness analysis highlights rough blocks of the scarp and the meter-scale step-like ridges that are more apparent in the 5 m and 10 m roughness analyses (Figure 6).

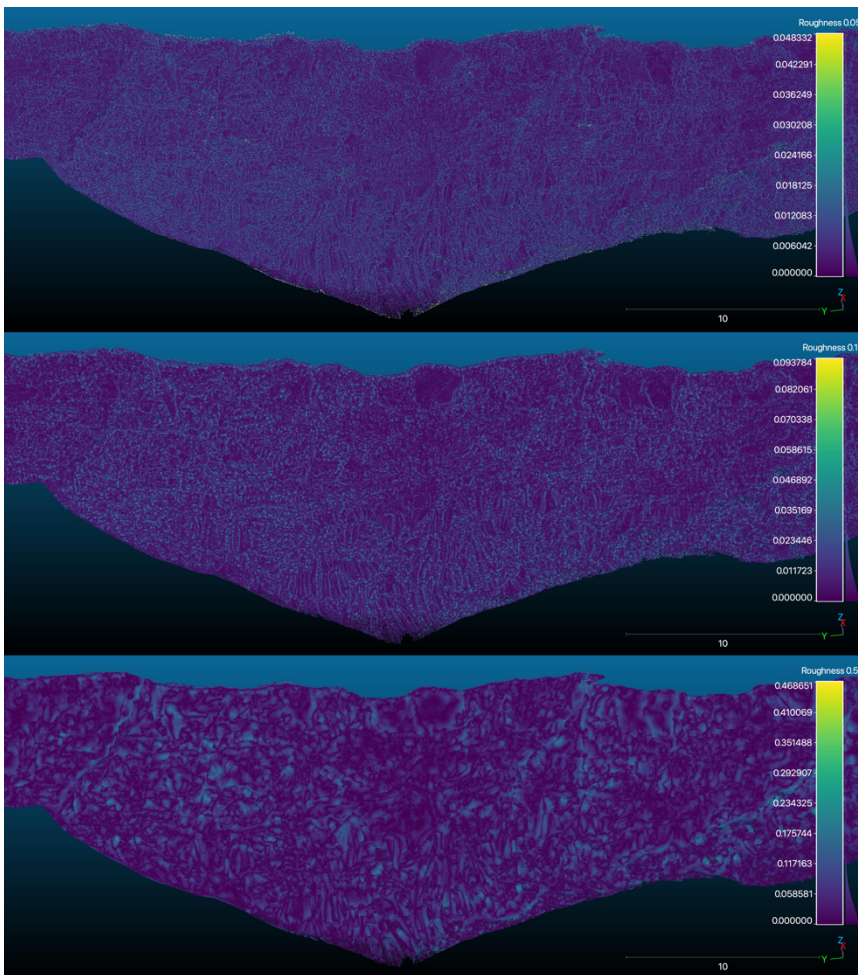**Figure 7.** A subset of the scarp point cloud to show features of 0.05 m, 0.1 m, and 0.5 m roughness analyses. Note the different range of each colorbar, representing the range of roughness values in each analysis, expressed in meters. The scale bar in the lower right corner is 10 m.

4. Discussion

Our phase association method combined with the amplitude-based event location method of Battaglia and Aki (2003) provides a powerful tool to calculate event hypocenters in regions without seismic velocity models, using simplifying assumptions about the system. We calculated travel-time-based locations using different variations of a 1D seismic velocity model and verified phase picks with manually assigned uncertainties however the results were poorly constrained and generated event locations pinned to the boundaries of the region, suggesting unrealized complexity in the seismic velocity model. Future work may employ local earthquake tomography to generate a velocity model for the region on and surrounding the RRL.

The apparent clustering of event locations along the scarp on the eastern boundary of the landslide may in part be an artifact of the network geometry, where nearly all seismometers were located east of the scarp in a nearly linear array (Figure 1a). The network geometry makes it difficult to resolve the longitudinal component of each event hypocenter due to the lack of longitudinal network coverage. However, the landslide body may be highly attenuating to seismic waves from its fractured state. A highly attenuating landslide would naturally filter out seismic signals that travel greater distances through the attenuating material, so we do not expect to recover the majority of seismic signals generated from the western boundary of the landslide and beyond.

The areas of high roughness in the 1 m, 5 m, and 10 m analyses form vertical clusters on some regions of the scarp, namely from 5155540 m to 5155760 m in Figure 5, though the full extent of these clusters is obscured by the varying height of the exposed scarp. The varying height of the scarp point cloud is a result of landslide debris collecting in certain areas which obfuscates the scarp and results in a smaller exposed scarp area. Thus we only consider areas of the RRL scarp that are free of landslide debris. (Sagy et al., 2007)) investigated the roughness of fault scarps and found that fault surface roughness decreases with increasing slip. If this finding holds for the RRL, the majority of slip should occur on areas of the scarp with lower roughness. Additionally, if more slip occurs on smoother surfaces, the lower portions of the scarp should be smoother than the

upper portions since the upper scarp was the first part to be exposed. However, we find that fault roughness dominantly clusters vertically at scales of r≥1m, and there is no apparent spatial clustering at smaller scales.
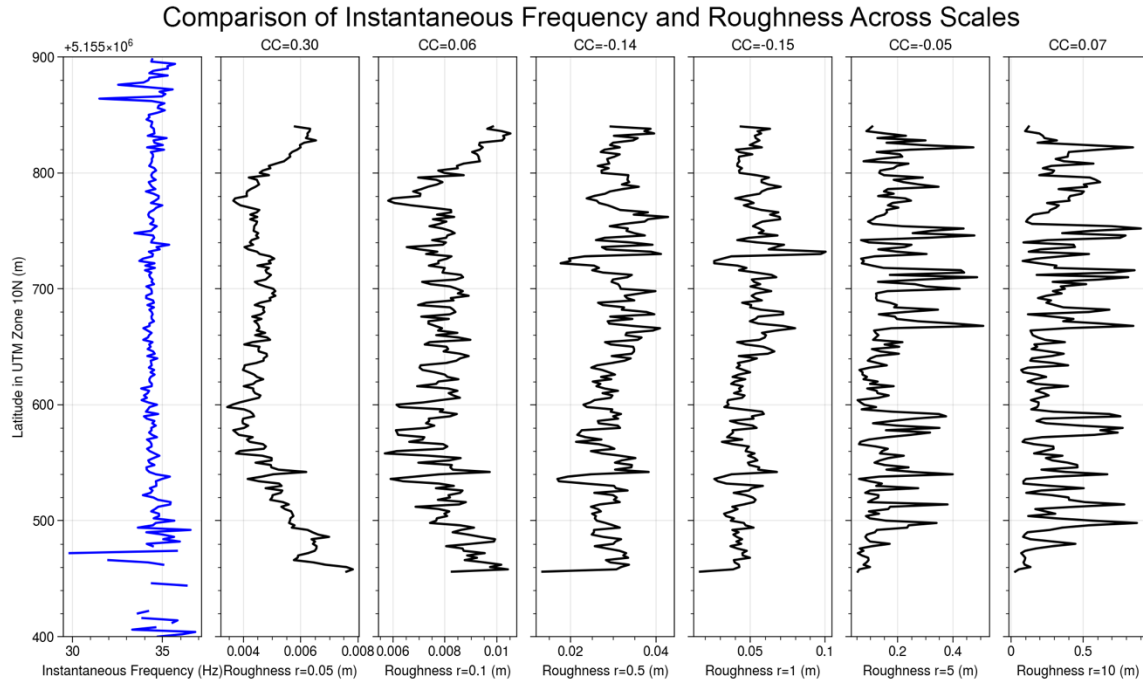
Figure 8. The leftmost panel shows the median instantaneous frequency of all events in 2 m latitude bins, expressed in Hz. Each successive panel shows the median scarp roughness for neighborhood radii of 0.05 m, 0.1 m, 0.5 m, 1 m, 5 m, and 10 m from 2 m latitude bins. Note the different ranges of each x-axis, representing the range of roughness values in each analysis, expressed in meters. The Pearson correlation coefficient with the median instantaneous frequency from each bin is indicated at the top of each roughness panel.

Despite the lack of apparent spatial trends in the distribution of the source amplitudes and instantaneous frequencies at the whole-landslide scale (Figure 4a, 4b), the instantaneous frequencies of events are remarkably consistent over time. Figure 5a shows the source instantaneous frequencies for all events occurring on March 13, 2018 and May 17, 2018, where the median difference is 0.4 Hz suggesting a constant physical control on the source frequency over time like the fracture properties of the host material. We binned the instantaneous frequency of events by 2 m of latitude to compare the results of our source analysis with our scarp roughness analysis. The binned source frequencies are consistent with minor variations from the median instantaneous frequency except for the bins at the edges due to event sparseness (Figure 8). We binned the scarp roughness by 2

m of latitude across all neighborhood scales to investigate along-scarp variations in roughness and determine the Pearson correlation coefficient between the binned source frequencies and binned roughnesses. Figure 8 shows the along-scarp source frequencies and roughnesses, where the scarp roughness for a 0.05 m neighborhood is most highly correlated with the source frequency at a correlation coefficient of 0.30.

5. Conclusions

We showed that source frequency is most correlated to fault roughness at the scale of 5 cm on the Rattlesnake Ridge Landslide. Fault roughness at other length scales is not strongly correlated to source frequency. Additionally, we found a nearly constant source frequency distribution throughout the duration of our experiment, suggesting a uniform fracture mechanism and elastic decoupling along the landslide body. We determined locations for 24,115 events detected on March 13, 2018, the first day of the experiment, and in total we detected 43,661,881 microseismic phase arrivals and 4,837,460 events over the 17-week span of our nodal seismometer experiment. Since our best source-scarp correlation was at the finest spatial resolution, an expansion of this work that is currently underway finely discretizes the parameter space of the amplitude-based location method to determine more precise event locations and estimates of event size to explore the relationship between source character and fault geometry at a smaller scale.

CHAPTER IV

AN ASSESMENT OF VERTICAL LAND MOVEMENT ALONG THE NORTHERN CASCADIA SUBDUCTION ZONE

1. Introduction

Coastlines support diverse ecosystems and a myriad of anthropogenic interests like communities, historical sites, and infrastructure. The safety and prosperity of coastal communities and the natural and built environment depend on our ability to plan for, predict and adapt to changing conditions like rising mean sea level. Mean sea level change over time-frames of decades to centuries is primarily driven by thermal expansion of the ocean and mass loss from glaciers and ice sheets [1], but can be modified locally by the vertical velocity of the land along the coast, leading to relative sea level change. Therefore, it is necessary to pair estimates of absolute sea level change with vertical land movement estimates in order to constrain relative sea level change and better assess the vulnerability of coastal resources. Vertical land movement (VLM) refers to the average long-term displacement of land surface in a geocentric reference frame that results from reorganization of the materials comprising Earth's crust or from isostatic adjustment of the crust in response to a changing load [2]. Both anthropogenic processes (e.g. groundwater and hydrocarbon extraction, loading from water reservoirs, and anthropogenic compaction) and local natural processes (e.g. sediment compaction, tectonic deformation, and glacial isostatic adjustment) can cause vertical land movement at a variety of temporal (days to centuries) and spatial scales (millimeters to thousands of kilometers) [3,4]. Estimates of VLM are used to constrain models of these causal processes and assessments of earthquake, tsunami, and storm hazards [5,6]. The focus of this study is to constrain rates of land motion and relative sea level change to inform coastal hazards planning utilizing a method that is adaptable to other regions.

In coastal Washington State, on the Pacific coast of central North America, variable rates of coastal vertical land movement have been estimated by a variety of researchers, ranging between 4 mm/yr uplift and -1 mm/yr subsidence. Regional patterns of VLM in coastal Washington are largely attributed to tectonic processes [7,8] from the Cascadia subduction zone (CSZ) to the west, and glacio-isostatic adjustment from deglaciation [9,10]. The CSZ hosts great earthquakes on a 500-530-year average recurrence interval [11] and is the predominant geodynamic process in this region generating crustal strain accumulation, in addition to clockwise forearc rotation [12]. Washington also hosts smaller crustal faults like the Seattle fault [13], as well as a multitude of volcanoes along the Cascadia volcanic arc. The geology of the coastal region is dominated by young oceanic basalt and sedimentary rock spanning the study area [14, 15]. The area of interest in this study spans from the Pacific Ocean to the Cascadia volcanic arc, specifically along the coastline of Washington State.

Previous investigators have attempted to estimate rates of vertical land movement in the Pacific Northwest of the USA generally, and specifically in Washington State, motivated either by the desire to incorporate those movements into sea level assessments, or to inform seismic hazard assessments [16–19]. Most investigations have utilized one of three different methods for measuring long-term rates of vertical land movement: 1) Leveling, which utilizes repeat measurements of geodetic monuments to derive a relative estimate of vertical land movement (i.e., vertical movement of one survey benchmark relative to another; see Burgette et al. [7]. Many early studies of vertical land movement referenced these relative rates to a geodetic reference frame by linking leveling results to estimates of vertical land movement derived from tide gauges. 2) "Water-level differencing" methods difference water levels measured at tide gauges located close to each other to derive an estimate of vertical land movement at one tide gauge site relative to another. Many early studies of vertical land movement converted the relative rates derived using this approach to absolute rates using an assumed global average rate of sea level change. 3) Continuous global navigation satellite systems (CGNSS), which utilizes regularly-sampled measurements of position from fixed GNSS stations to derive an

estimate of long-term vertical land movement rates in an absolute (i.e., geocentric) reference frame (i.e., movements relative to a center of mass of the Earth).

Mote et al. [20] conducted a review and discussion of investigations to characterize vertical land movement in Washington State. They compared three previous studies [21–23], all based primarily on leveling, to a preliminary CGNSS analysis. They found general agreement in regional patterns between these previous investigations, but discrepancies in the estimated rates of vertical land movement in some locations. More recent studies [16,17,20,24,25], attempted to estimate rates and patterns of vertical land movement with the goal of resolving differences between relative sea level measured at tide gauges against vertical land movement rates at co-located CGNSS stations. These investigations provide a way to assess trends in regional absolute sea level, and compare the regional sea level trends against globally averaged rates. In general, these investigations rely on CGNSS datasets, typically from just one of several data providers, and also typically focus on a very limited number of locations in Washington State that are co-located with tide gauges. The most recent studies have also utilized GNSS glacial isostatic adjustment (GIA) corrections at tide gauges [18] and multiple CGNSS data providers [19].

In terms of resolving spatial variations in vertical land movement, most previous analyses suffered from either limited data, relying on estimates from just one data source or methodology, and/or a lack of estimates made directly on the coast. In addition, Snay et al. [16] point out discrepancies between different providers of continuous CGNSS-derived vertical land movement estimates, which are also a consequence of the application of different methodologies, differing time-series lengths, or different analysis approaches. Finally, previous sea level rise assessments focused on Washington State [20,25] incorporated estimates of VLM into relative sea level projections, but without enough spatial resolution to resolve meaningful along-coast variations on a community scale. Partly as a consequence of these short-comings, local coastal managers in Washington State reported that they didn't have adequate information to plan adequately for sea level rise [26]. Globally, studies have identified centimeter-scale VLM signals combining leveling and spaceborne SAR [27], however coastal Washington is heavily

44

vegetated and regional mm/yr scale VLM is outside of the observable range of standard SAR processing in our study region.

In this study, we present an approach to assimilate VLM estimates and their uncertainties, derived from multiple data types, in order to maximize the density of estimates on the coastal landscape and better account for the discrepancies between them. We also account for the primary VLM signal in areas without measurements by interpolating multiple data types and modeled vertical land velocities from interseismic tectonic locking on the CSZ, which dominates vertical velocities in instrumented areas. Our work reveals variable rates of vertical land movement in coastal Washington that may exacerbate or outpace sea level change depending on the location. We combine our model of vertical land movement with absolute sea level change projections and produce probabilistic relative sea level change projections, under two greenhouse gas scenarios and assuming no subduction zone earthquake, along the entirety of coastal Washington (first presented by Miller et al. [28]). The approach presented here is adaptable to any study area for which measurements and models of VLM exist, and represents an improvement over current methods of VLM estimation, resulting in dense and robust estimates of VLM that benefit coastal hazards planning.

2. Materials and Methods

2.1. Data
2.1.1. Continuous GPS

GNSS observations provide estimates of vertical land motion rates in a geocentric reference frame. While these estimates are relatively precise (with uncertainties on the order of several mm/yr), solutions can vary depending on processing assumptions, such as regional filtering methods or how atmospheric water vapor is modeled. The observed differences in vertical rate estimates and their uncertainties across different CGNSS datasets [16] motivated us to develop an assimilative approach for deriving vertical land movement rates from CGNSS data from multiple GNSS datasets. We based our best estimates and associated uncertainties for CGNSS sites on the distribution in estimated

rates and uncertainties across datasets provided by five different providers: Nevada Geodetic Laboratory [29], NASA JPL [30], Scripps Orbit and Permanent Array Center [31], Pacific Northwest Geodetic Array Geodesy Laboratory [32], and UNAVCO [33]. All of the GNSS data are in the ITRF2008 reference frame.

Data were downloaded for all available stations in the Pacific Northwest (inclusive of western Oregon, western Washington and southern British Columbia) from the five different CGNSS data processing groups. To address the disparity in rates and uncertainties across CGNSS-derived estimates we first classified CGNSS stations into high/low quality categories based on the length of the time-series over which vertical velocity solutions were estimated from a visual examination of the relationship between uncertainty and time-series length. Records exceeding nine years were initially classified as "high-quality". Records shorter than nine years were classified as "high-quality" only if at least three of the vertical rate estimates across the different processing groups agreed to within ±1 mm/yr. Stations designated as "low-
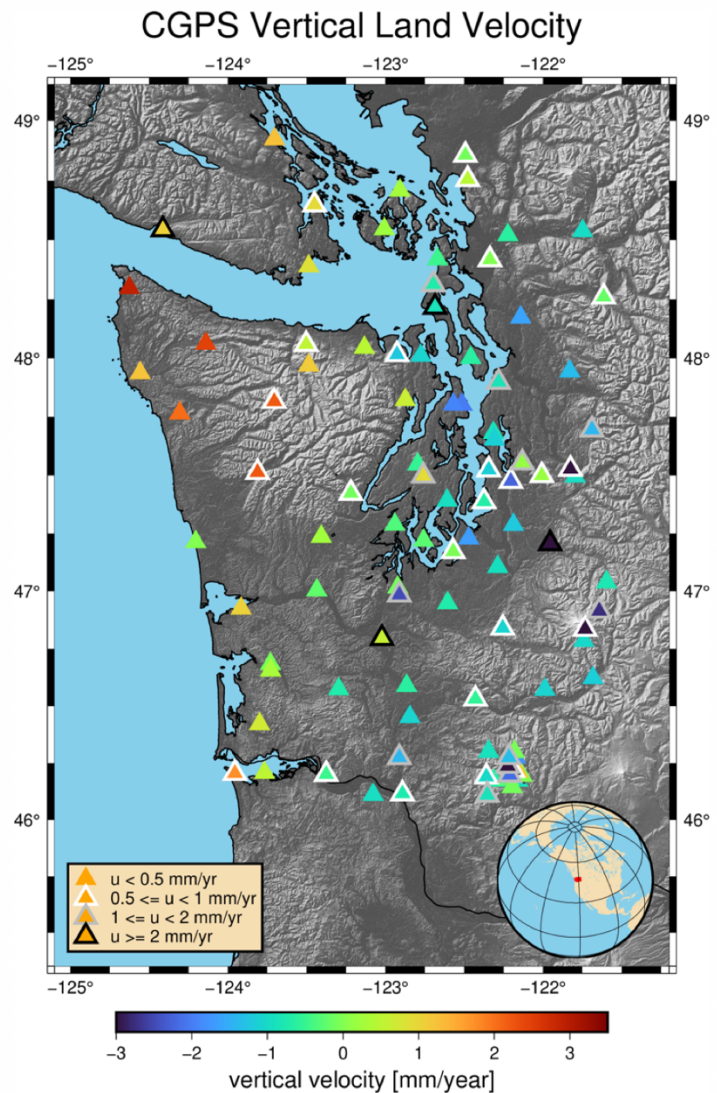

Figure 1. Continuous GNSS measurements of vertical land movement from five data providers. Vertical velocity is denoted by marker color and uncertainty is denoted by marker outline. A transition from uplift, at the western tip of the Olympic Peninsula, to subsidence east is apparent in the CGNSS observations. Refer to Figure 2 for names of places.

quality" via this filtering step were excluded from further analysis. This quality assessment procedure classified 117 out of 188 total CGNSS stations in our area of interest (Figure 1) as "high-quality".

The best estimate of the vertical rate at a CGNSS site was designed to take into account differences in solutions between the five different datasets, and was arrived at through a multi-step process. First, an outlier detection algorithm was applied to the "high-quality" CGNSS sites with more than three estimates from different processing groups, in order to separate out stations with longer time-series but for which one of the processing group's estimates was dramatically different from the others. For this assessment we applied a median absolute deviation approach to identify outliers, with an outlier cut-off value of 6. Therefore, any value with a median absolute deviation of more than 6 times the median value was eliminated from the calculation of a mean velocity across data processing centers.

Next, we calculated a weighted average of the individual vertical rate estimates, where the weighting was scaled by an adjusted uncertainty in the station vertical velocity:

$$\bar{x} = \ \Sigma_{i=1} \frac{x_i}{\sigma_i^2} \Big/ \Sigma_i \frac{1}{\sigma_i^2} \qquad \text{(Eq. 1)}$$

where x_i are the reported velocities from the different processing groups and σ_i are the adjustment uncertainties for each observation. The weighted averaging approach has the effect of making those vertical velocities with smaller adjusted uncertainties carry more weight in the vertical velocity averaging process. The magnitude of the uncertainty estimates for CGNSS-based vertical land movement observations were not consistent across data providers, with some providing a relatively narrow uncertainty range and others estimating a wide uncertainty range. However, the relative scale of the uncertainties was generally consistent within and across datasets and was assumed to be indicative of the relative scale of uncertainty of the estimates between stations. In order to utilize the weighted averaging approach described in Equation 1 the different uncertainty estimates for each station needed to be adjusted. As a result, we developed an adjustment

process to rescale uncertainties and facilitate comparisons across datasets. We assume that the uncertainty in the vertical rate estimate should asymptote to a stable value as more observations become available (i.e., due to a longer observational record). We therefore corrected the uncertainty estimates by: 1) Calculating the mean uncertainty for each of the five CGNSS data sets for all high-quality stations. 2) Estimating a scaling factor for the reported uncertainties for each processing center such that the mean uncertainty for all high-quality stations is consistent between processing centers. This ensures that the variability in uncertainty is preserved between stations. 3) Multiplying all CGNSS vertical uncertainties by the appropriate scaling factor assigned to each processing center. To estimate the uncertainty of our final, average vertical velocity rates for each station we calculated the standard deviation of the vertical rate estimates for a station, as calculated by the different processing groups (Figure 1). This approach was more conservative than propagating the error associated with each rate.

2.1.2. Tide Gauges

Water-level differencing, in our case differencing monthly-averaged water levels from tide gauges, provides an estimate of the relative difference in vertical land velocity rates between tide gauges. There are two approaches: "single-differencing", which assumes that the stations are close enough to each other that they experience the same variations in sea level; and "double-differencing", which does not assume that the stations share an absolute sea-level trend, but rather attempts to directly estimate the absolute sea level pattern at a tide gauge using altimetry [34]. We conducted a single-differencing analysis that employed the following steps: 1) Obtain monthly average water level data from the Permanent Service for Mean Sea Level for a set of 23 stations in Oregon, Washington and British Columbia. 2) Choose a set of "reference stations" that were co-located with a "high quality" CGNSS station (within 5km, though 3 of the 4 reference stations were located less than 500 m apart), and included a long (>20 years) water level record. 3) Difference each station's monthly sea level against those from each of the four reference stations. 4) Remove the mean seasonal signal in the resulting

differed time-series, by subtracting out the long-term average for each calendar month. 5) Estimate the trend and standard error in the linear regression, accounting for auto-correlation (using the variance inflation factor approach described in Zervas [35]. 6) Adjust the estimated relative vertical velocity to an absolute rate by adding it to the best estimate vertical rate derived from the high quality CGNSS station co-located with each "reference" water level station. The uncertainties assigned to the rates derived using this approach (Figure 2) were estimated by propagating the uncertainty assigned to the co-located CGNSS station.

Figure 2. Measurements of vertical land movement derived from water level differencing of tide gauges. Vertical velocity is denoted by marker color and uncertainty is denoted by marker outline. Places and areas mentioned in this study are labeled with stars and names in white.

2.1.3. Leveling

Leveling is a surveying method that is used to measure the relative height difference between two nearby benchmarks. By repeating a survey of the benchmarks at a later time and differencing against an earlier data set, it is possible to measure the rate of change in the elevation difference between benchmarks. This method provides relative changes in height between adjacent stations (i.e. tilt) and must be tied to a nearby CGNSS or tide gauge station in order to be placed in a reference frame. We incorporate vertical rates from leveling in our analysis using the methodologies and data described in Burgette et al. [7], Krogstad et al. [36], Mitchell et al. [22], and Schmidt et al. [37], which utilize historical leveling data dating to the 1920's (Figure 3), by adjusting
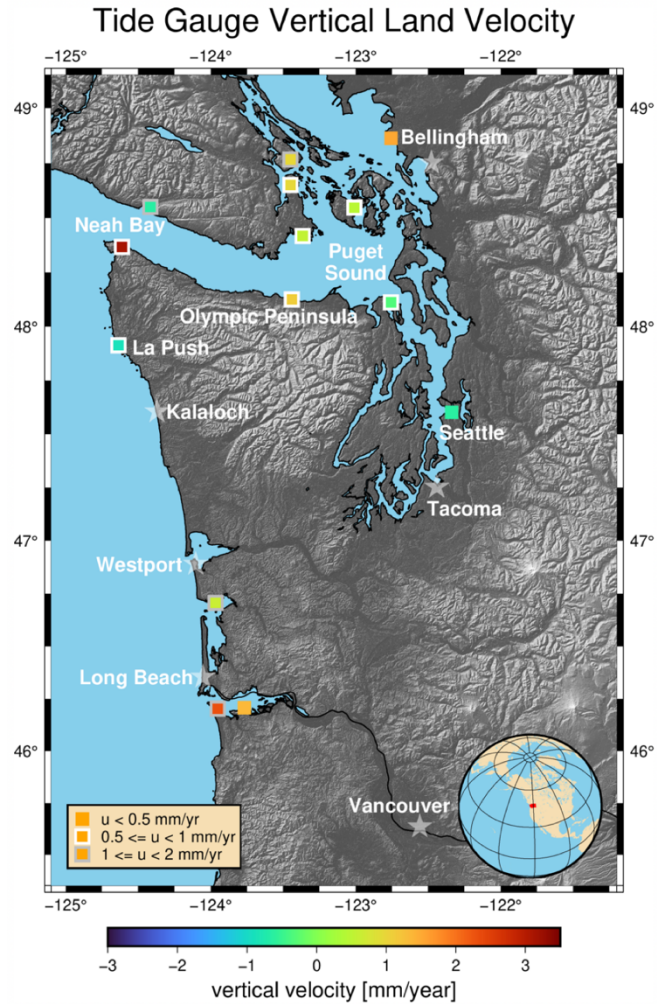
49

earlier tide gauge-based reference frames to ours, based on CGNSS as described above. We also added two new lines from Westport and Tacoma east. These relative rates were converted to absolute rates of vertical land movement by attaching leveling lines to nearby high-quality CGNSS stations. Relative vertical rates for a series of benchmarks along a leveling line (typically located along transportation corridors) were adjusted to best fit the vertical land movement estimates of one or more nearby CGNSS stations or tide gauges. The uncertainty of the CGNSS station is assigned to the nearest leveling point, then uncertainty is propagated from that point using the measurement uncertainties of successive leveling observations. We also recalculated the uncertainties for the north-south line on the east side of the Olympic Peninsula that were too small in previous work that we incorporated.

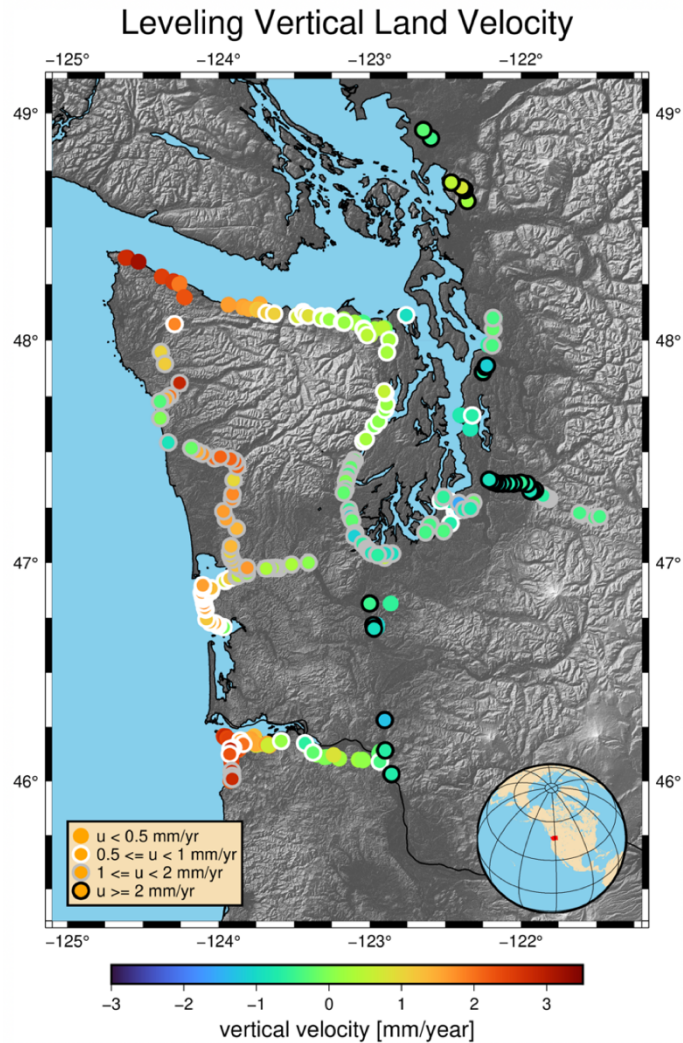**Figure 3.** Measurements of vertical land movement derived from leveling. Vertical velocity is denoted by marker color and uncertainty is denoted by marker outline. Spatially dense leveling observations perpendicular to the Cascadia subduction zone show the dominant east-west VLM signal resulting from interseismic locking on the megathrust. Refer to Figure 2 for place names.

2.2. Tectonic Model

Within our study area we found a total of 519 VLM rate estimates from CGNSS, leveling, and tide gauges (Figure 4). However, there are large stretches of our study area for which vertical land movement observations do not exist (Figure 4). The limited data that exist near the coast and the spatially-dense leveling lines (roughly perpendicular to the CSZ) suggest large gradients in vertical land movement over short distances, which could lead to a misrepresentation of rates of vertical land movement on the shoreline in areas where most observations are collected farther inland. Specifically, at locations on the north and central coast near La Push and Kalaloch, Washington, observations point to subsidence on the shoreline, and rapid uplift only a short distance inland. Further, an interpolation of the combined vertical land velocity observations yields unphysical

Figure 4. Vertical rate estimates extracted from the tectonic model, and measurements of vertical land movement derived from CGNSS, leveling, and tide gauges. Data type is denoted by marker shape, vertical velocity is denoted by marker color, and uncertainty is denoted by marker outline. We prescribed a conservative uncertainty of 2 mm/yr to estimates from the tectonic model. Note the numerous stretches of coastline without VLM measurements. Refer to Figure 2 for place names.

edge effects since all data were acquired on land and there are no seafloor observations to constrain the western edge of the interpolation. To first order, the large-scale pattern of deformation revealed by vertical land movement observations in our area of interest can
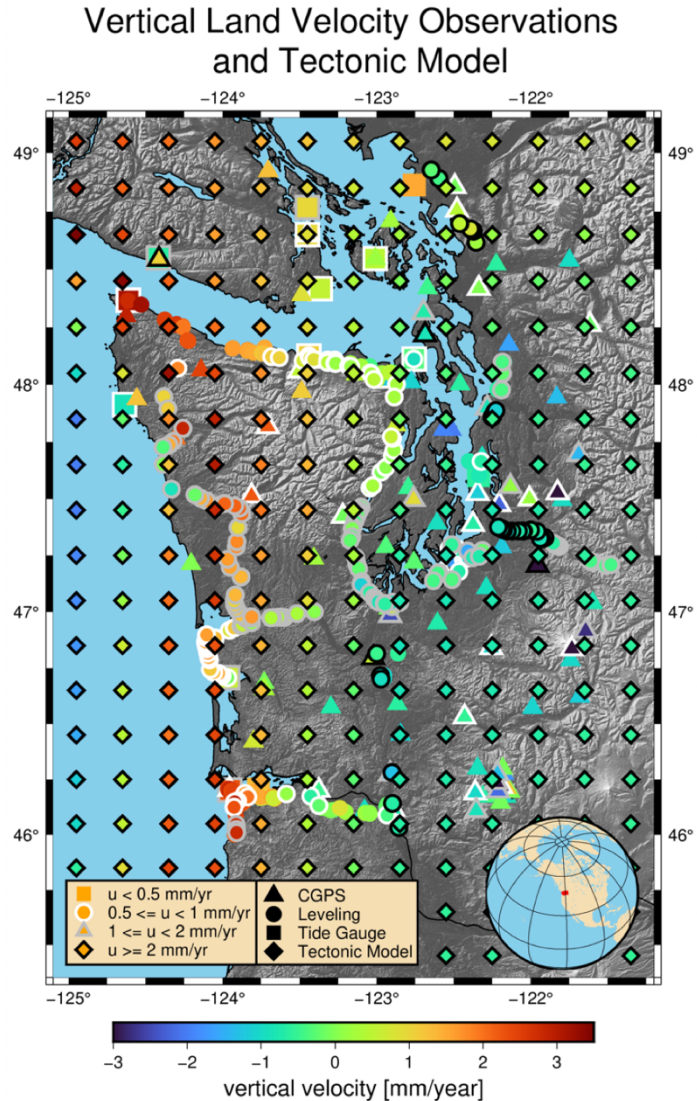
be explained by interseismic locking of the megathrust on the Cascadia subduction zone, and large gradients in near-coast deformation are likely [38].

We incorporated a discretely sampled velocity field derived from a forward model of a locked fault slipping at depth in the Cascadia subduction zone in our analysis to place geophysical constraints on the expected vertical signal in regions without direct measurements. The interseismic locking model uses the modeling framework of Burgette et al. [7], which was solely focused on modeling leveling data in Oregon, but expanded to Washington State and constrained by both vertical leveling and horizontal GPS velocities by Schmidt et al. [37]. This locking model was compared to and combined with other similar locking models to constrain seismic hazards in the Pacific Northwest for the United States National Seismic Hazard Maps [5] in Frankel and Petersen [39]. The interseismic locking model assumes that the slip deficit rate is equal to the plate convergence rate (i.e. fully locked) near the trench and decreases exponentially in the transition zone. The locking model is also assumed to vary smoothly along strike. The depth of the lower edge of the fully locked zone and lower edge of the transition zone as a function of latitude are optimized through a grid search. The resulting locking model is largely similar to other locking models for Cascadia [5], where fault locking is primarily confined to the megathrust at depths shallower than 20 km (coinciding with sections of the megathrust west of the coastline). In using the locking model for this paper, we use the distribution of the slip-rate deficit on the megathrust to forward predict uplift rate across our focus area. To better match the new refined data set, we have applied a uniform vertical shift to account for our different reference frame.

The locking model is intended to physically model the crustal strain associated with the convergence of the Juan de Fuca and North American plates, which is the dominant signal in the geodetic data. This strain is elastically stored in the crust and will eventually be released in a future megathrust earthquake on the subduction zone, thus our estimates of vertical land velocity are not valid after the next megathrust earthquake. Our tectonic model does not model other processes, like compaction of sediments, erosion, or the movement of shallow crustal faults that may result in the vertical movement of the ground. Vertical rate estimates were extracted from the locking model at a grid spacing of

52

0.2-degree (16-22 km). These were combined with our other vertical rate estimates for the purposes of interpolating a best-estimate vertical velocity field. The modeled vertical rates were arbitrarily assigned a relatively large uncertainty of ± 2 mm/yr to minimize the influence of the model in areas with ample observations. The locking model is not used to replace or modify the observations, but rather is used to more accurately interpolate vertical velocity estimates at locations between the observations, particularly where large gradients exist.

2.2. Interpolation

We interpolate between all discrete observations and gridded tectonic model velocity field points to represent the vertical land velocity as a surface that is a function of the longitude and latitude, or a height field with z = f(longitude, latitude). Since we model the vertical velocity as a height field, the field may not contain vertical slopes or overhangs, neither of which are realistic representations of land movement at the scale of interest (~10 km). We first generate a scattered interpolant from the combined observed and modeled vertical velocities using Delaunay triangulation with bivariate linear interpolation [40]. Triangulation of the scattered vertical velocities in the longitude-latitude plane generates a continuous surface composed of triangular pieces joined at edges, or a triangulated irregular network, over the area of interest. The triangulated irregular network represents a piecewise interpolation scheme in which bivariate linear interpolation is applied to each triangle. We then query the interpolant at a grid spacing of 0.1-degree to yield an interpolated vertical land velocity height field (Figure 5a).

To include a measure of uncertainty for interpolated vertical velocities we employ bootstrapping. At each location with observed or modeled vertical velocities we specify a normal distribution defined by the vertical velocity as the distribution mean and the standard deviation. We then randomly sample each distribution and generate an interpolated vertical velocity height field, repeating the process 10,000 times. The reported interpolation uncertainty is the standard deviation, with N-1 normalization, of the 10,000 interpolation iterations at each grid point, thus representing the variation in

53

interpolated vertical velocity given hypothetical variations in the data. In essence, the uncertainty presented in Figure 5b is a measure of the stability of the interpolation results.
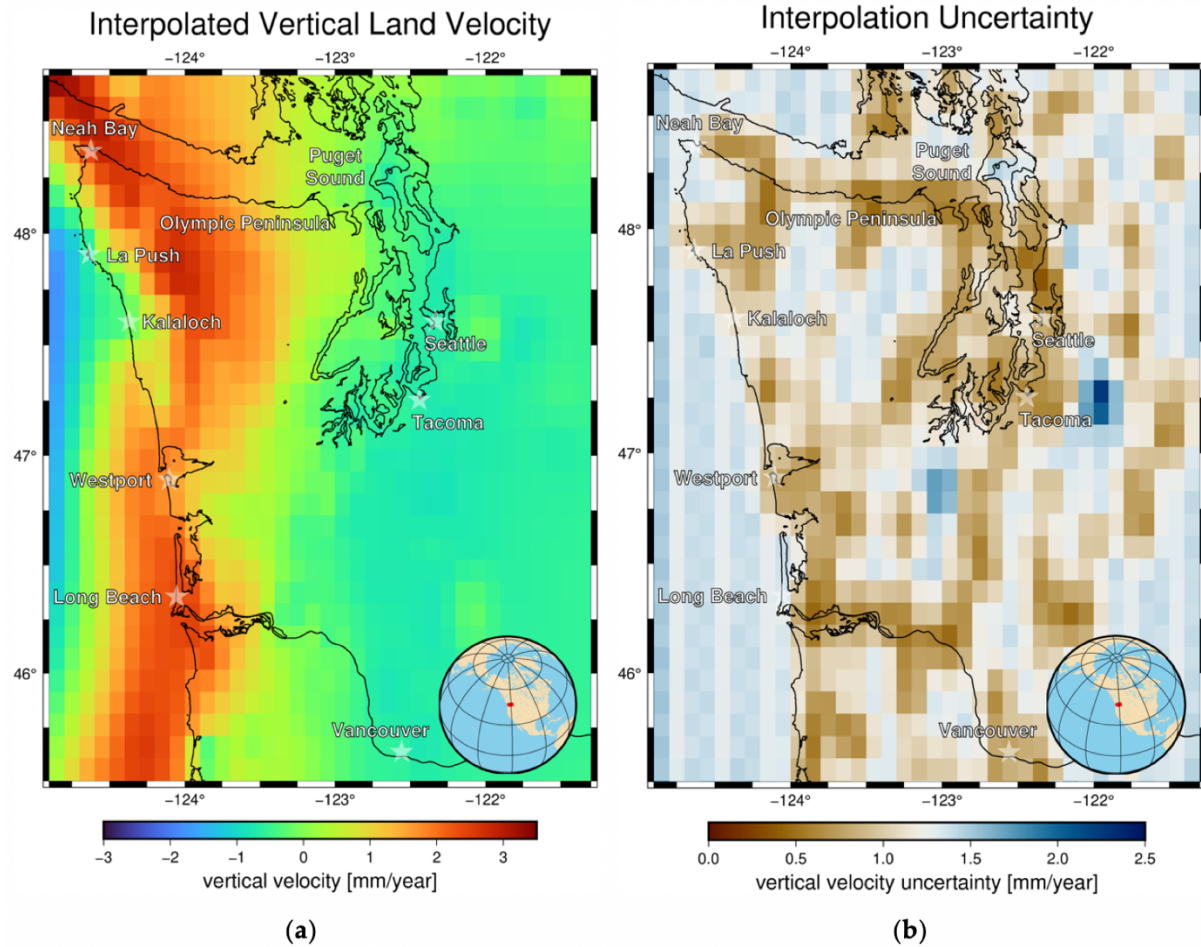
Figure 5. (a) Interpolated surface queried on a 0.1-degree grid representing a continuous vertical velocity field for coastal Washington; (b) Bootstrapped uncertainty of the interpolated vertical velocity field shown in Figure 5a.

3. Results

We model the vertical velocity field of coastal Washington as an interpolated height field to produce the most spatially comprehensive estimate of vertical land motion for coastal Washington to date. Previous investigators have found variations in coastal vertical land movement ranging from ~1.0 mm/yr of subsidence (in central Puget Sound) to approximately 3-4 mm/yr of uplift (on the northwest tip of the Olympic Peninsula). Overall, we find the same general patterns suggested by previous investigators, and resolve many of the finer-scale variations between tide stations and leveling lines. In

addition, we find the most rapid rates of coastal uplift associated with the northwest tip of the Olympic Peninsula (Figure 5). Our results also suggest:

1.   A strong west-to-east gradient in rates of vertical land movement across our area of interest that is particularly pronounced along a transect following the Strait of Juan de Fuca (Figure 5a), and that we attribute to subduction zone processes.

2.   Low rates of subsidence (< 1 mm/yr) in Puget Sound, but with a south-to-north gradient showing higher rates of subsidence to the south and lower rates to the north, consistent with the pattern expected for glacio-isostatic adjustment.

3.   Rapid uplift along the southwest Washington coast, but with a large uncertainty in estimated rates, including Westport and the Long Beach Peninsula.

We also find a broad area of coastal subsidence along the northern Pacific Ocean coast of Washington State (Figure 6). Previous studies generally do not make spatially continuous VLM estimates throughout this area, though some studies did find evidence of subsidence in the same area [23,34]. Other studies estimated uplift (e.g. [14]) along this section of coast, or observations in this area were not considered (e.g. [11]). Figure 6 shows the northwest region of study area where we find subsidence along coastal Washington, indicated by the colored grid that constitutes the interpolated vertical velocity surface, in addition to VLM observations and the gridded tectonic model that inform the interpolation. Observations of VLM from leveling, tide gauges, and CGNSS stations in this region show spatial vertical velocity gradients (0.2 mm/km) that are steeper than those present in the tectonic locking model (0.1 mm/km; Figure 6). Figure 7a

shows the interpolant queried at a sub-kilometer scale along the coastline to depict smooth variations in coastal VLM, and Figure 7b shows the associated uncertainty.

Despite the density of observations utilized in this assessment, areas of large uncertainty remain, either due to uncertainties in the observations themselves, large gradients in the rate of vertical land movement, or a lack of observations in certain parts of the landscape. We quantify the uncertainty associated with our interpolated model of vertical land motion (Figure 5b). It is important to note, there are also areas of uplift or subsidence driven by processes other than interseismic strain accumulation and at scales smaller than the resolution of this study are not well-represented in our model or uncertainty analysis. Areas containing VLM observations with high uncertainties (observations with black outlines in Figure 4) correspond to the areas in our model with the highest uncertainty (dark blue colors in Figure 5b). The focus of
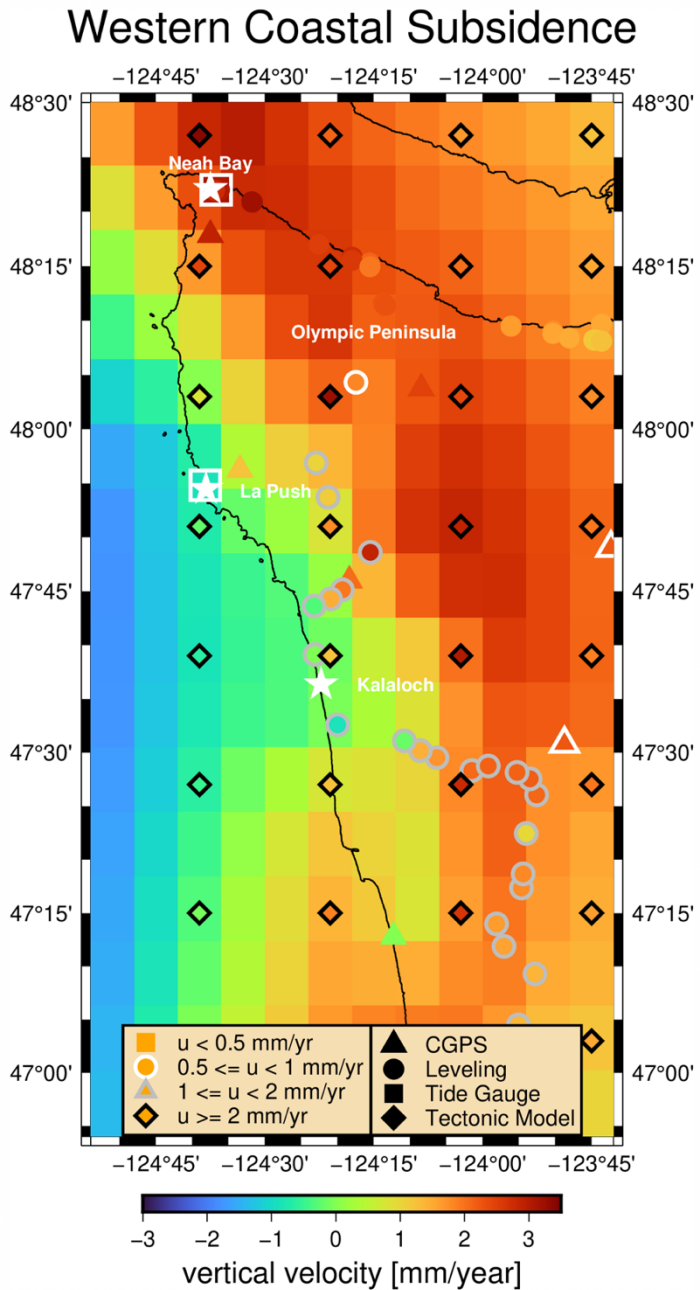
Figure 6. Broad region of coastal subsidence in Washington State along the western Olympic Peninsula. Also shown are vertical rate estimates extracted from the tectonic model, and measurements of vertical land movement derived from CGNSS, leveling, and tide gauges. Data type is denoted by marker shape, vertical velocity is denoted by marker color, and uncertainty is denoted by marker outline.
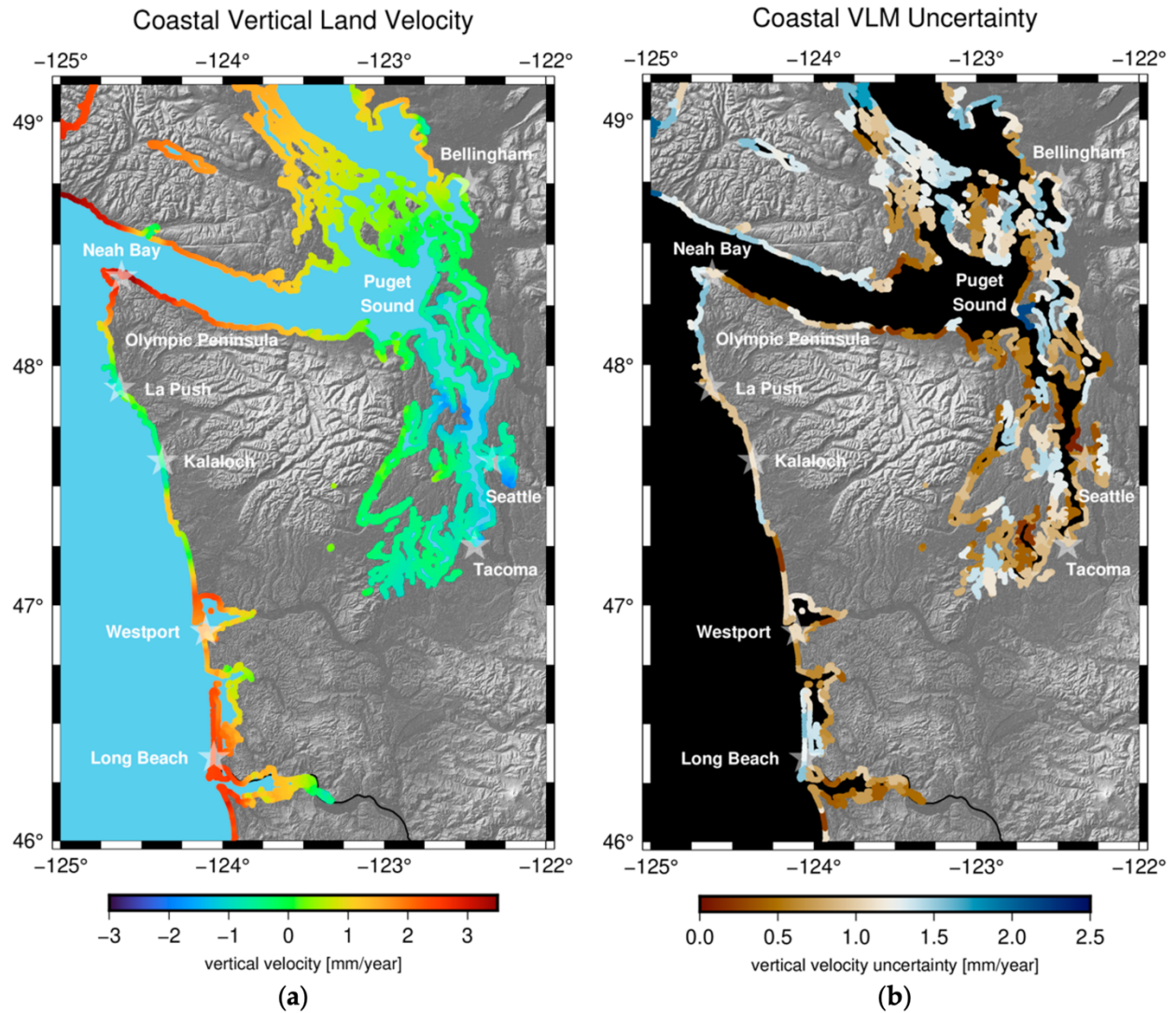
Figure 7. (a) Coastal vertical land movements along Washington's coastline, derived from our interpolant, representing a continuous vertical velocity field for coastal Washington (Figure 5a). Select cities and towns marked by a star and their name in white. (b) Bootstrapped uncertainty of the interpolated vertical velocity field (as shown in Figure 5b) for coastal Washington.

this study is to provide robust estimates of vertical land movement along the coast, so our estimated rates of VLM in inland Washington, particularly near volcanoes and the eastern boundary of our model, do not fully characterize contemporary crustal movements considering interseismic strain accumulation decreases with distance from the subduction zone.

4. Discussion

Our estimates of VLM and the associated uncertainties, when combined with sea level projections, provide insights about current and future relative sea level changes for coastal communities throughout Washington that can supply local coastal managers with the information necessary to plan adequately for sea level rise (Figure 7a, 7b). An assumption of this study, supported by over 70 years of tide gauge and repeated leveling observations, is that the observed and modeled rates of vertical land movement are constant over the interseismic period, so we discuss the implications of a Cascadia subduction zone earthquake on vertical land motion in the region. Additionally, we further explore spatial patterns in the resulting interpolated vertical velocity field and identify a convolved north-south vertical velocity gradient, likely from glacial isostatic adjustment, that will continue whether there is a Cascadia earthquake or not. To conclude this study, we explore the effect of the assumed GIA signal on an elastic dislocation model of Cascadia subduction zone locking, and thus could impact earthquake hazard level estimates.

4.1. Relative Sea Level Change

We combine our estimate of interpolated vertical land movement with absolute sea level change projections to produce probabilistic relative sea level change projections for 171 locations throughout coastal Washington under two greenhouse gas scenarios, first presented by Miller et al. [28]. We utilize a single absolute sea level rise projection for all of Washington State, as the regional variations in absolute sea level change are not well resolved over this scale [28]. The low and high greenhouse gas scenarios (RCP 4.5 and 8.5 [41]) reflect different emissions trajectories that depend on human behavior over decades; thus we do not speculate which scenario is more likely. The projections presented in Figure 8 incorporate uncertainties from the models and observations incorporated into the assessment, which includes the range of expected mass loss from the Antarctica and Greenland ice sheets. Our projections are presented as the likelihood that sea level change will meet or exceed a particular offset from contemporary sea level, or the probability of exceedance. We utilize an approach for estimating absolute sea level

change adapted from Kopp et al. [42] for seven Washington State tide gauges, fully described by Miller et al. [28].
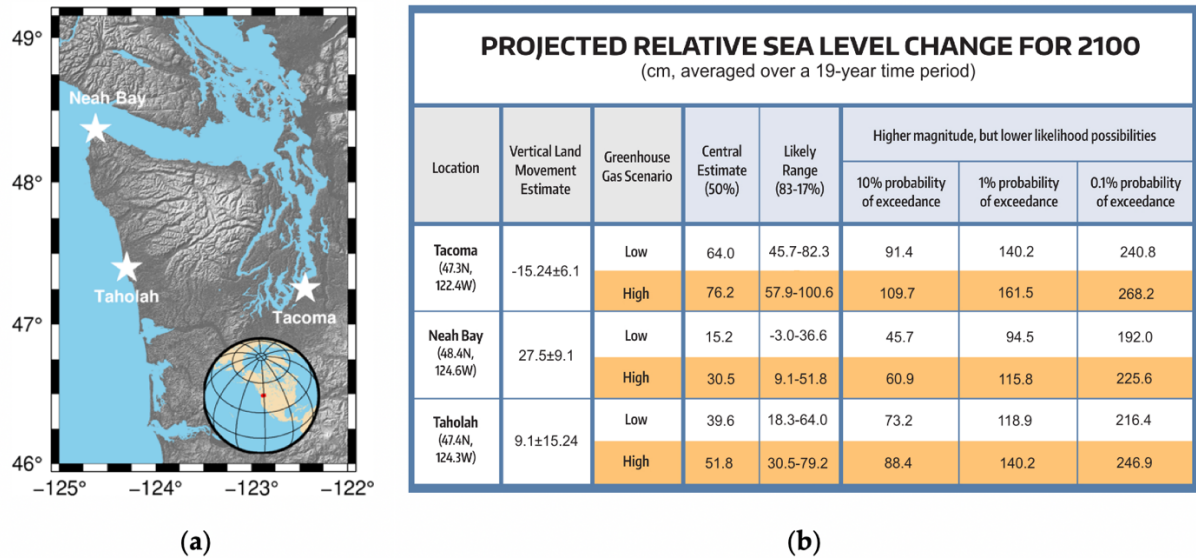
PROJECTED RELATIVE SEA LEVEL CHANGE FOR 2100 (cm, averaged over a 19-year time period)							
Location	Vertical Land Movement Estimate	Greenhouse Gas Scenario	Central Estimate (50%)	Likely Range (83-17%)	Higher magnitude, but lower likelihood possibilities		
					10% probability of exceedance	1% probability of exceedance	0.1% probability of exceedance
Tacoma (47.3N, 122.4W)	-15.24±6.1	Low	64.0	45.7-82.3	91.4	140.2	240.8
		High	76.2	57.9-100.6	109.7	161.5	268.2
Neah Bay (48.4N, 124.6W)	27.5±9.1	Low	15.2	-3.0-36.6	45.7	94.5	192.0
		High	30.5	9.1-51.8	60.9	115.8	225.6
Taholah (47.4N, 124.3W)	9.1±15.24	Low	39.6	18.3-64.0	73.2	118.9	216.4
		High	51.8	30.5-79.2	88.4	140.2	246.9

(a)   (b)

Figure 8. Three coastal locations in Washington State discussed in: (b) table adapted from Miller et al. [28] showing relative sea level rise projections for 3 of 171 locations along coastal Washington. Projections are expressed in terms of the probability of exceedance for 2100 under two different greenhouse gas scenarios (RCP 4.5 ["Low"] and RCP 8.5 ["High"]; [41]). Projected changes are assessed relative to contemporary sea level, defined as the average sea level over the 19-year period 1991-2009. Projections for all 171 locations are available in [28].

Since interseismic strain accumulation from tectonic locking on the CSZ is the primary VLM signal in the coastal Pacific Northwest on a regional scale, relative sea level rise patterns mirror the opposite of the tectonic uplift signal. Areas like Neah Bay that experience rapid vertical uplift (Figure 7) will, in general, experience less relative sea level rise, and sea level drop in cases where vertical land velocities outpace rates of absolute sea level rise. Conversely, regions experiencing land subsidence, like Tacoma (Figure 7), will have rates of relative sea level rise that are greater than the rate of absolute sea level rise. The effect of large uncertainties in vertical land velocities can be seen in the projections for sites like Long Beach peninsula, resulting in a large difference between probability of exceedance projections. Relative sea level projections for 171 locations along the Washington coast are available and we refer readers to Miller et al. [28] for additional details of our relative sea level rise assessment.

4.2. Cascadia Earthquake Scenario

We assume constant rates of vertical land movement during an interseismic period, and thus constant strain accumulation. This assumption is reasonable given that: 1) we are late in the interseismic period when deformation rates are expected to be constant in time [38], and 2) nearly constant rates of VLM are observed for the ~70-year tide gauge and leveling record. However, the uplift proximal to the coast indicates that strain energy is accumulating in the crust and will be released in the next megathrust earthquake. A large earthquake would result in coseismic land displacements that void our assumption of a constant deformation rate and produce temporally and spatially variable rates of vertical land movement. Additionally, rapid and spatially variable
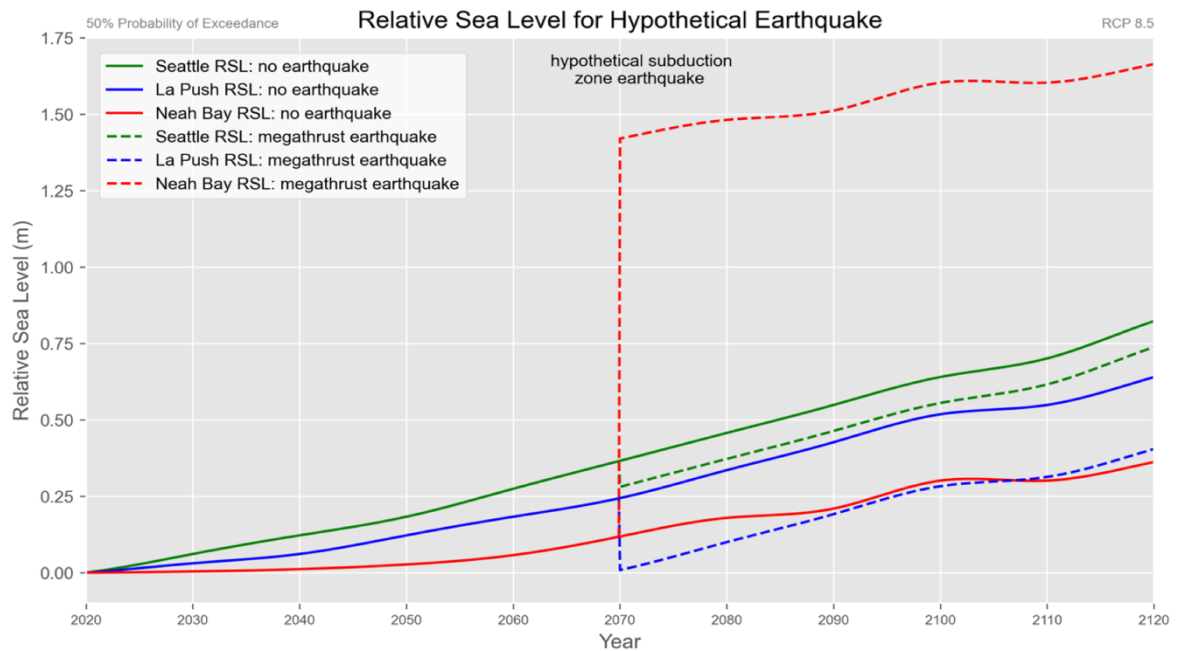

Figure 9. Relative sea level (RCP 8.5 and a 50% probability of exceedance) over time with and without a hypothetical megathrust rupture at 2070 to exhibit the effect of coseismic land change on relative sea level at La Push, Neah Bay, and Seattle. Coseismic land change is assumed to equal the sum of our estimated annual vertical deformation rate due to the Cascadia subduction zone summed over the hypothetical interseismic period, with the opposite sense of motion. We assume no postseismic viscoelastic relaxation for the purpose of this visualization. The hypothetical earthquake and associated coseismic land changes will produce an instantaneous shift in RSL, and areas experiencing rapid uplift, like Neah Bay, will see a dramatic increase in RSL. Regions that are subsiding west of the zone of interseismic uplift, like La Push, are expected to experience coseismic uplift and will see a decrease in RSL after a major subduction zone earthquake. Regions well east of the subduction zone, such as Puget Sound and Seattle, are expected to experience minor uplift.

postseismic deformation follows large earthquakes, resulting from viscoelastic stress transfer that continues decades after the earthquake. The Tohoku earthquake that struck central Japan on March 11, 2011, for example, resulted in coastal subsidence of more than 1 meter in places along the east coast of Japan [43]. Localized uplift of the coast is also possible depending on the geometry of the subduction zone and proximity of the coast to the zone of locking. Figure 9 provides simplified examples of the effect of a megathrust earthquake on relative sea level for three sites from 2020 to 2120 with and without a hypothetical megathrust earthquake at the year 2070, assuming that our estimated VLM rate is entirely due to subduction processes and full recovery of the VLM rate summed over the hypothetical interseismic period (1700-2070). The true coseismic VLM depends on the type and timing of rupture, but previous studies that focus on constraining the complexities of coseismic displacements report a range of coseismic subsidence consistent with our first-order estimate for areas experiencing uplift [6,44,45,46]. Despite the simplifications and assumptions inherent to the hypothetical coseismic land motions depicted in Figure 9, the region of subsidence we find from La Push to Kalaloch may produce coseismic uplift rather than the coseismic subsidence expected in regions experiencing interseismic uplift, depending on the complexities of subduction processes. Thus Figure 9 serves to reiterate the importance of constraining VLM and the driving processes to inform hazard assessments.

4.3. North-south VLM Gradient

We find two dominant signals in the data that are most-evident in our study area: an east-west gradient consistent with locking along the Cascadia subduction zone (CSZ), and a smaller magnitude south-north gradient that is most apparent east of the region affected by subduction zone locking. The two gradients are superimposed in the coastal region, although VLM data are routinely used to inform subduction zone models that assume the data are absent of independent sources of motion. To isolate the north-south vertical velocity gradient, we utilize the gridding of our interpolated surface and find the mean value for all rows of 0.1-degree by 0.1-degree cells east of -123.0° longitude, then we subtract the mean for each row from all 0.1-degree by 0.1-degree cells in that row. The longitude-averaged north-south vertical velocity ranges from 0.6 mm/yr in the north

(49.0° latitude) to -0.7 mm/yr in the south (45.5° latitude). This simple estimate of the observed north-south gradient assumes that the vertical velocity gradient is strictly north-south trending, but is intended to provide only a first-order approximation of the signal.

To assess the contribution of this vertical velocity gradient, we generate simple elastic dislocation models (as in Schmidt et al. [37]) for CSZ locking with and without the north-south gradient by subtracting the observed gradient east of the Puget Sound from all of Washington, including the CSZ locking-dominated gradient in coastal Washington, west of the Cascades. We compare the predicted horizontal strain from each model to the observed horizontal strain, measured from horizontal GNSS motion. Correcting for the north-south gradient in our model reduces the RMS error by 2% and better predicts the observed strain in Washington. Additionally, the correction extends the modeled extent of tectonic locking farther downdip near La Push. Since the observed vertical and horizontal strain best fit our model with the north-south regional uplift gradient removed, we hypothesize that this gradient is superimposed on the coastal region, and likely unrelated to the CSZ. We speculate that the observed north-south gradient is GIA, consistent with previous studies [4,9]; however other mechanisms are possible, including a 3D viscoelastic response to past CSZ rupture, rotation of the forearc, and local subsidence associated with the broader Puget Sound forearc basin region. Regardless of the source, the convolved signal implies that multiple overlapping processes are driving vertical land movement in Washington State.

5. Conclusions

We generate the most spatially comprehensive estimate of VLM to date for coastal Washington and find moderate rates of subsidence throughout the Puget Sound and near La Push, separated by a broad region of rapid uplift that extends south to Oregon. Combining VLM with forecast sea level rise provides relative sea level change for coastal Washington. A north-south vertical velocity gradient, consistent with GIA, is apparent in VLM observations and correction of an elastic dislocation model for this signal yields lower errors in the predicted horizontal strain in Washington when

compared to observations. The dominant VLM pattern in this region is consistent with interseismic strain accumulation on the CSZ.

Ideally, future research will combine new techniques and spatially-comprehensive data sets to produce dense and robust estimates of VLM. Previous VLM assessments predominantly infer uplift in the region spanning La Push to Kalaloch where we find subsidence [20,25]. Conflicting VLM results pose challenges for hazards planning in coastal communities; thus future studies that further constrain vertical uplift rates in areas with few direct observations are critical to understanding VLM and its sources throughout Washington. Since relative sea level projections utilize annually compounding rates of VLM, misestimation of vertical rates may lead to large errors in projected relative sea level and misuse of community resources leading to potential ramifications for community vulnerability. Further, VLM estimates inform coseismic deformation models that are critical for accurate estimation of tsunami hazards, requiring robust, spatially-comprehensive, and repeatable VLM estimates.

REFERENCES CITED

Chapter II

Álvarez-Gómez, J. A. (2019). FMC—Earthquake focal mechanisms data management, cluster and classification. SoftwareX, 9, 299–307. Anderson, E. M. (1951). The dynamics of faulting and dyke formation with applications to Britain. Edinburgh: Hafner Pub. Co. https://scits.stanford.edu/anderson-e-m-1951-dynamics-faulting-and-dyke-formation-applications-brittan-edinburgh-oliver-and

Angelier, J. (1984). Tectonic analysis of fault slip data sets. Journal of Geophysical Research, 89, 5835–5848. https://doi.org/10.1029/JB089iB07p05835

Arnold, R., & Townend, J. (2007). A Bayesian approach to estimating tectonic stress from seismological data. Geophysical Journal International, 170, 1336–1356. https://doi.org/10.1111/j.1365-246X.2007.03485.x

Arthur, D., & Vassilvitskii, S. (2006). K-means++: The advantages of careful seeding. In Proceedings of the annual acm-siam symposium on discrete algorithms. Stanford, CA: Stanford University. http://ilpubs.stanford.edu:8090/778/

Audet, P., & Bürgmann, R. (2014). Possible control of subduction zone slow-earthquake periodicity by silica enrichment. Nature, 510,389–392. https://doi.org/10.1038/nature13391

Bird, P. (2003). An updated digital model of plate boundaries. Geochemistry, Geophysics, Geosystems, 4(3), 1027. https://doi.org/10.1029/2001GC000252

Bott, M. H. P. (1959). The mechanics of oblique slip faulting. Geological Magazine, 96, 109–117. https://doi.org/10.1017/S0016756800059987

Brown, J. R., Beroza, G. C., Ide, S., Ohta, K., Shelly, D. R., Schwartz, S. Y., et al. (2009). Deep low-frequency earthquakes in tremor localize to the plate interface in multiple subduction zones. Geophysical Research Letters, 36, L19306. https://doi.org/10.1029/2009GL040027

Brown, K. M., Kopf, A., Underwood, M. B., & Weinberger, J. L. (2003). Compositional and fluid pressure controls on the state of stress on the Nankai subduction thrust: A weak plate boundary. Earth and Planetary Science Letters, 214, 589–603. https://doi.org/10.1016/S0012821X(03)00388-1

Bürgmann, R. (2018). The geophysics, geology and mechanics of slow fault slip. Earth and Planetary Science Letters, 495, 112–134. https:// doi.org/10.1016/j.epsl.2018.04.062

Byerlee, J. (1978). Friction of rocks. In Rock friction and earthquake prediction. Basel: Birkhäuser. https://doi.org/10.1007/978-3-0348-71822_4

Byrne, T. B., Lin, W., Tsutsumi, A., Yamamoto, Y., Lewis, J. C., Kanagawa, K., et al. (2009). Anelastic strain recovery reveals extension across SW Japan subduction zone. Geophysical Research Letters, 36, L23310. https://doi.org/10.1029/2009GL040749

Collettini, C., Tesei, T., Scuderi, M. M., Carpenter, B. M., & Viti, C. (2019). Beyond Byerlee friction, weak faults and implications for slip behavior. Earth and Planetary Science Letters, 519, 1–316. https://doi.org/10.1016/j.epsl.2019.05.011

DeMets, C., Gordon, R. G., & Argus, D. F. (2010). Geologically current plate motions. Geophysical Journal International, 181, 1–80. https:// doi.org/10.1111/j.1365-246X.2009.04491.x

Dragert, H., Wang, K., & James, T. S. (2001). A silent slip event on the deeper Cascadia subduction interface. Science, 292, 1525–1528. https://doi.org/10.1126/science.1060152

French, M. E., & Condit, C. B. (2019). Slip partitioning along an idealized subduction plate boundary at deep slow slip conditions. Earth and Planetary Science Letters, 528, 1–10. https://doi.org/10.1016/j.epsl.2019.115828

Gao, X., & Wang, K. (2017). Rheological separation of the megathrust seismogenic zone and episodic tremor and slip. Nature, 543, 416–419. https://doi.org/10.1038/nature21389

Gephart, J. W. (1990). Stress and the direction of slip on fault planes. Tectonics, 9, 845–858. https://doi.org/10.1029/TC009i004p00845 Gephart, J. W., & Forsyth, D. W. (1984). An improved method for determining the regional stress tensor using earthquake focal mechanism data: Application to the San Fernando earthquake sequence. Journal of Geophysical Research, 89, 9305–9320. https://doi.org/10.1029/JB089iB11p09305

Gutenberg, B., & Richter, C. F. (1944). Frequency of earthquakes in California. Bulletin of the Seismological Society of America, 34(4), 185–188.

Hardebeck, J. L. (2015). Stress orientations in subduction zones and the strength of subduction megathrust faults. Science, 349, 1213–1216. https://doi.org/10.1126/science.aac5625

Hardebeck, J. L., & Hauksson, E. (1999). Role of fluids in faulting inferred from stress field signatures. Science, 285, 236–239. https://doi.org/10.1126/science.285.5425.236

Hardebeck, J. L., & Loveless, J. P. (2018). Creeping subduction zones are weaker than locked subduction zones. Nature Geoscience, 11, 60–64. https://doi.org/10.1038/s41561-017-0032-1

Hardebeck, J. L., & Michael, A. J. (2004). Stress orientations at intermediate angles to the San Andreas Fault, California. https://doi.org/10.1029/2004JB003239

Hardebeck, J. L., & Michael, A. J. (2006). Damped regional-scale stress inversions: Methodology and examples for southern California and the Coalinga aftershock sequence. Journal of Geophysical Research, 111, B11310. https://doi.org/10.1029/2005JB004144

Hawthorne, J. C., & Rubin, A. M. (2010). Tidal modulation of slow slip in Cascadia. Journal of Geophysical Research, 115, B09406. https://doi.org/10.1029/2010JB007502

Hayes, G. P., Moore, G. L., Portner, D. E., Hearne, M., Flamme, H., Furtney, M., & Smoczyk, G. M. (2018). Slab2, a comprehensive subduction zone geometry model. Science, 362, 58–61. https://doi.org/10.1126/science.aat4723

Healy, D. (2012). Anisotropic poroelasticity and the response of faulted rock to changes in pore-fluid pressure. Geological Society Special Publication, 367, 201–214. https://doi.org/10.1144/SP367.14

Hill, D. P. (1993). A note on ambient pore pressure, fault-confined pore pressure, and apparent friction. Bulletin of the Seismological Society of America, 83(2), 583–586.

Hirose, H., & Obara, K. (2005). Repeating short- and long-term slow slip events with deep tremor activity around the Bungo channel region, southwest Japan. Earth, Planets and Space, 57, 961–972. https://doi.org/10.1186/BF03351875

Ikari, M. J., Saffer, D. M., & Marone, C. (2009). Frictional and hydrologic properties of a major splay fault system, Nankai subduction zone. Geophysical Research Letters, 36, L20313. https://doi.org/10.1029/2009GL040009

Ikeda, M., Toda, S., Kobayashi, S., Ohno, Y., Nishizaka, N., & Ohno, I. (2009). Tectonic model and fault segmentation of the Median Tectonic Line active fault system on Shikoku, Japan. Tectonics, 28, TC5006. https://doi.org/10.1029/2008TC002349

Itaba, S., Kitagawa, Y., Koizumi, N., Takahashi, M., Matsumoto, N., & Takeda, N. (2012). The variation of the strain, tilt and groundwater level in the Shikoku district and Kii peninsula, Japan (from may to october 2011). Report of the Coordinating Committee for Earthquake Prediction, 87, 399–418.

Itaba, S., Kitagawa, Y., Koizumi, N., Takahashi, M., Matsumoto, N., & Takeda, N. (2013a). Short-term slow slip events in the Tokai area, the Kii peninsula and the Shikoku district, Japan (from May to October 2012). Report of the Coordinating Committee for Earthquake Prediction, 89, 226–238.

Itaba, S., Kitagawa, Y., Koizumi, N., Takahashi, M., Matsumoto, N., & Takeda, N. (2013b). Short-term slow slip events in the Tokai area, the Kii peninsula and the Shikoku district, Japan (from November 2012 to April 2013). Report of the Coordinating Committee for Earthquake Prediction, 90, 254–269.

Itaba, S., Koizumi, N., Takahashi, M., Matsumoto, N., Kitagawa, Y., Ochi, T., & Takeda, N. (2014). Short-term slow slip events in the Tokai area, the Kii peninsula and the Shikoku district, Japan (from November 2013 to April 2014). Report of the Coordinating Committee for Earthquake Prediction, 92, 238–249.

Itaba, S., Koizumi, N., Takahashi, M., Matsumoto, N., Kitagawa, Y., & Takeda, N. (2014). Short-term slow slip events in the Tokai area, the Kii peninsula and the Shikoku district, Japan (from May to October 2013). Report of the Coordinating Committee for Earthquake Prediction, 91, 230–242.

Ito, Y., Asano, Y., & Obara, K. (2009). Very-low-frequency earthquakes indicate a transpressional stress regime in the Nankai accretionary prism. Geophysical Research Letters, 36, L20309. https://doi.org/10.1029/2009GL039332

Kagan, Y. Y. (2005). Double-couple earthquake focal mechanism: Random rotation and display. Geophysical Journal International, 164, 236–245. https://doi.org/10.1111/j.1365-246X.2005

Kaneda, H., & Okada, A. (2008). Long-term seismic behavior of a fault involved in a multiple-fault rupture: Insights from tectonic geomorphology along the Neodani Fault, central Japan. Bulletin of the Seismological Society of America, 98, 2170–2190. https://doi.org/ 10.1785/0120070204

Kano, M., Aso, N., Matsuzawa, T., Ide, S., Annoura, S., Arai, R., et al. (2018). Development of a slow earthquake database. Seismological Research Letters, 89, 1566–1575. https://doi.org/10.1785/0220180021

Katsumata, A., & Kamaya, N. (2003). Low-frequency continuous tremor around the Moho discontinuity away from volcanoes in the southwest Japan. Geophysical Research Letters, 30(1), 1020. https://doi.org/10.1029/2002GL015981

Kaverina, A. N., Lander, A. V., & Prozorov, A. G. (1996). Global creepex distribution and its relation to earthquake-source geometry and tectonic origin. Geophysical Journal International, 125, 249–265. https://doi.org/10.1111/j.1365-246X.1996.tb06549.x

Kita, I., Yamamoto, M., Asakawa, Y., Nakagawa, M., Taguchi, S., & Hasegawa, H.(2001). Contemporaneous ascent of within-plate type and island-arc type magmas in the Beppu-Shimabara graben system, Kyushu island, Japan. Journal of Volcanology and Geothermal Research, 111, 99. https://doi.org/10.1016/S0377-0273(01)00222-0

Kitagawa, Y., Itaba, S., Koizumi, N., Takahashi, M., Matsumoto, N., & Takeda, N. (2012). Short-term slow slip events in the Tokai area, the Kii peninsula and the Shikoku district, Japan (from November 2011 to April 2012). Report of the Coordinating Committee for Earthquake Prediction, 88, 303–311.

Kitagawa, Y., Itaba, S., Takahashi, M., Matsumoto, N., & Takeda, N. (2011). The variation of the strain, tilt and groundwater level in the Shikoku district and Kii peninsula, japan (from November 2010 to May 2011). Report of the Coordinating Committee for Earthquake Prediction, 86, 519–533.

Kobayashi, A. (2014). A long-term slow slip event from 1996 to 1997 in the Kii Channel, Japan. Earth, Planets and Space, 66, 9. https://doi. org/10.1186/1880-5981-66-9

Kopf, A., & Brown, K. M. (2003). Friction experiments on saturated sediments and their implications for the stress state of the Nankai and Barbados subduction thrusts. Marine Geology, 202, 193–210. https://doi.org/10.1016/S0025-3227(03)00286-X

Kubo, A., & Fukuyama, E. (2003). Stress field along the Ryukyu Arc and the Okinawa Trough inferred from moment tensors of shallow earthquakes. Earth and Planetary Science Letters, 310, 305–316. https://doi.org/10.1016/S0012-821X(03)00132-8

Kubo, A., Fukuyama, E., Kawai, H., & Nonomura, K. (2002). NIED seismic moment tensor catalogue for regional earthquakes around Japan: Quality test and application. Tectonophysics, 356, 23–48. https://doi.org/10.1016/S0040-1951(02)00375-X

Lee, J., Hong, T. K., & Chang, C. (2017). Crustal stress field perturbations in the continental margin around the Korean Peninsula and Japanese islands. Tectonophysics, 718, 140–149. https://doi.org/10.1016/j.tecto.2017.08.003

Lin, W., Byrne, T. B., Kinoshita, M., McNeill, L. C., Chang, C., Lewis, J. C., et al. (2016). Distribution of stress state in the Nankai subduction zone, southwest Japan and a comparison with Japan Trench. Tectonophysics, 692, 120–130. https://doi.org/10.1016/j.tecto.2015.05.008

Lombardi, A. M. (2017). SEDA: A software package for the Statistical Earthquake Data Analysis. Scientific Reports, 7, 1–16. https://doi.org/10.1038/srep44171

Lund, B., & Slunga, R. (1999). Stress tensor inversion using detailed microearthquake information and stability constraints: Application to Ölfus in southwest Iceland. Journal of Geophysical Research, 104, 14,947–14,964. https://doi.org/10.1029/1999JB900111

MATLAB (2018). Version 9.4.0.813654 (r2018a). Natick, Massachusetts: The MathWorks Inc.

Martínez-Garzón, P., Ben-Zion, Y., Abolfathian, N., Kwiatek, G., & Bohnhoff, M. (2016). A refined methodology for stress inversions of earthquake focal mechanisms. Journal of Geophysical Research: Solid Earth, 121, 8666–8687. https://doi.org/10.1002/2016JB013493

Martínez-Garzón, P., Kwiatek, G., Ickrath, M., & Bohnhoff, M. (2014). MSATSI: A MATLAB package for stress inversion combining solid classic methodology, a new simplified user-handling, and a visualization tool. Seismological Research Letters, 85, 896–904. https://doi.org/10.1785/0220130189

Matsu'ura, M., & Hasegawa, Y. (1987). A maximum likelihood approach to nonlinear inversion under constraints. Physics of the Earth and Planetary Interiors, 47, 179–187. https://doi.org/10.1016/0031-9201(87)90076-8

Maury, J., Cornet, F. H., & Dorbath, L. (2013). A review of methods for determining stress fields from earthquakes focal mechanisms; Application to the Sierentz 1980 seismic crisis (Upper Rhine Graben). https://doi.org/10.2113/gssgfbull.184.4-5.319

McKenzie, D. P. (1969). Relation between fault plane solutions for earthquakes and the directions of the principal stresses. Bulletin of the Seismological Society of America, 29, 189–193. https://doi.org/10.1136/bmj.2.3908.1076

Michael, A. J. (1984). Determination of stress from slip data: Faults and folds. Journal of Geophysical Research, 89, 11,517–11,526. https://doi.org/10.1029/JB089iB13p11517

Miyazaki, S., & Heki, K. (2001). Crustal velocity field of southwest Japan: Subduction and arc-arc collision. Journal of Geophysical Research, 106, 4305–4326. https://doi.org/10.1029/2000JB900312

Nadeau, R. M., & Dolenc, D. (2005). Nonvolcanic tremors deep beneath the San Andreas Fault. Science, 307, 389. https://doi.org/10.1126/science.1107142

Nishimura, T. (2014). Short-term slow slip events along the Ryukyu Trench, southwestern Japan, observed by continuous GNSS. Progress in Earth and Planetary Science, 1, 22. https://doi.org/10.1186/s40645-014-0022-5

Nishimura, T., Matsuzawa, T., & Obara, K. (2013). Detection of short-term slow slip events along the Nankai Trough, southwest Japan, using GNSS data. Journal of Geophysical Research: Solid Earth, 118, 3112–3125. https://doi.org/10.1002/jgrb.50222

Obara, K. (2002). Nonvolcanic deep tremor associated with subduction in southwest Japan. Science, 296, 1679–1681. https://doi.org/10.1126/science.1070378

Obara, K., Hirose, H., Yamamizu, F., & Kasahara, K. (2004). Episodic slow slip events accompanied by non-volcanic tremors in southwest Japan subduction zone. Geophysical Research Letters, 31, L23602. https://doi.org/10.1029/2004GL020848

Obara, K., & Ito, Y. (2005). Very low frequency earthquakes excited by the 2004 off Kii peninsula earthquakes: A dynamic deformation process in the large accretionary prism. Earth, Planets and Space, 57, 321–326. https://doi.org/10.1186/BF03352570

Ochi, T., Itaba, S., Koizumi, N., Takahashi, M., Matsumoto, N., Kitagawa, Y., & Takeda, N. (2015). Short-term slow slip events in the Tokai area, the Kii peninsula and the Shikoku district, Japan (from November 2014 to April 2015). Report of the Coordinating Committee for Earthquake Prediction, 94, 250–261.

Ochi, T., Itaba, S., Koizumi, N., Takahashi, M., Matsumoto, N., Kitagawa, Y., & Takeda, N. (2016). Short-term slow slip events in the Tokai area, the Kii peninsula and the Shikoku district, Japan (from May 2015 to October 2015). Report of the Coordinating Committee for Earthquake Prediction, 95, 255–264.

Okada, Y., Kasahara, K., Hori, S., Obara, K., Sekiguchi, S., Fujiwara, H., & Yamamoto, A. (2004). Recent progress of seismic observation networks in Japan—Hi-net, F-net, K-net and KiK-net. Earth, Planets and Space, 56, xv–xxviii. https://doi.org/10.1186/BF03353076

Pawlowicz, R. (2019). M_map: A mapping package for Matlab, version 1.4k. www.eoas.ubc.ca/~rich/map.html

Payero, J. S., Kostoglodov, V., Shapiro, N., Mikumo, T., Iglesias, A., Pérez-Campos, X., & Clayton, R. W. (2008). Nonvolcanic tremor observed in the Mexican subduction zone. Geophysical Research Letters, 35, L07305. https://doi.org/10.1029/2007GL032877 Reid, H. F. (1910). The California earthquake of April 18, 1906. Report of the State Earthquake Investigation Commission, 2, 16–18.

Research Information Database DB095: Active fault database of Japan (2012). National Institute of Advanced Industrial Science and Technology https://gbank.gsj.jp/activefault/index_e_gmap.html

Rogers, G., & Dragert, H. (2003). Episodic tremor and slip on the Cascadia subduction zone: The chatter of silent slip. Science, 300, 1942–1943. https://doi.org/10.1126/science.1084783

Sacks, A., Saffer, D. M., & Fisher, D. (2013). Analysis of normal fault populations in the Kumano forearc basin, Nankai Trough, Japan: 2. Principal axes of stress and strain from inversion of fault orientations. Geochemistry, Geophysics, Geosystems, 14, 1973–1988. https://doi. org/10.1002/ggge.20118

Sagiya, T., Miyazaki, S., & Tada, T. (2000). Continuous GPS array and present-day crustal deformation of Japan. Pure and Applied Geophysics, 157, 2303–2322. https://doi.org/10.1007/978-3-0348-7695-7_26

Scholz, C. H. (2015). On the stress dependence of the earthquake b value. Geophysical Research Letters, 42, 1399–1402. https://doi.org/ 10.1002/2014GL062863

Sekine, S., Hirose, H., & Obara, K. (2010). Along-strike variations in short-term slow slip events in the southwest Japan subduction zone. Journal of Geophysical Research, 115, B00A27. https://doi.org/10.1029/2008JB006059

Shelly, D. R., Beroza, G. C., & Ide, S. (2007). Non-volcanic tremor and low-frequency earthquake swarms. Nature, 446, 305–307. https://doi. org/10.1038/nature05666

Shen, L. W., Schmitt, D. R., & Haug, K. (2019). Quantitative constraints to the complete state of stress from the combined borehole and focal mechanism inversions: Fox Creek, Alberta. Tectonophysics, 764, 110–123. https://doi.org/10.1016/j.tecto.2019.04.023

Sibson, R. H. (1985). A note on fault reactivation. Journal of Structural Geology, 7(6), 751–754. https://doi.org/10.1016/0148-9062(92)91063b

Sibson, R. H. (1990). Rupture nucleation on unfavourably oriented faults. Bulletin—
Seismological Society of America, 7, 751–754. https:// doi.org/10.1016/0191-
8141(85)90150-6

Tada, T. (1985). Spreading of the Okinawa Trough and its relation to the crustal
deformation in the Kyushu (2). Zisin (Journal of the Seismological Society of Japan. 2nd
ser.), 51, 113–121. https://doi.org/10.4294/zisin1948.38.1_1

Takemura, S., Matsuzawa, T., Noda, A., Tonegawa, T., Asano, Y., Kimura, T., &
Shiomi, K. (2019). Structural characteristics of the Nankai Trough shallow plate
boundary inferred from shallow very low frequency earthquakes. Geophysical Research
Letters, 46, 4192–4201. https://doi.org/10.1029/2019GL082448

Terakawa, T., & Matsu'ura, M. (2010). The 3-D tectonic stress fields in and around Japan
inverted from centroid moment tensor data of seismic events. Tectonics, 29, TC6008.
https://doi.org/10.1029/2009TC002626

Thomas, A. M., Bürgmann, R., Shelly, D. R., Beeler, N. M., & Rudolph, M. L. (2012).
Tidal triggering of low frequency earthquakes near Parkfield, California: Implications for
fault mechanics within the brittle-ductile transition. Journal of Geophysical Research,
117, B05301. https://doi.org/10.1029/2011jb009036

Tobin, H. J., & Saffer, D. M. (2009). Elevated fluid pressure and extreme mechanical
weakness of a plate boundary thrust, Nankai Trough subduction zone. Geology, 37, 679–
682. https://doi.org/10.1130/G25752A.1

Townend, J., & Zoback, M. D. (2001). Implications of earthquake focal mechanisms for
the frictional strength of the San Andreas fault system. Geological Society Special
Publication, 186, 13. https://doi.org/10.1144/GSL.SP.2001.186.01.02

Townend, J., & Zoback, M. D. (2006). Stress, strain, and mountain building in central
Japan. Journal of Geophysical Research, 111, B03411.
https://doi.org/10.1029/2005JB003759

Tsutsumi, H., Okada, A., Nakata, T., Ando, M., & Tsukuda, T. (1991). Timing and displacement of holocene faulting on the median tectonic line in central Shikoku, southwest Japan. Journal of Structural Geology, 13, 227–233. https://doi.org/10.1016/0191-8141(91)90069-U

Ujiie, K., Saishu, H., Fagereng, Å., Nishiyama, N., Otsubo, M., Masuyama, H., & Kagi, H. (2018). An explanation of episodic tremor and slow slip constrained by crack-seal veins and viscous shear in subduction mélange. Geophysical Research Letters, 45, 5371–5379. https://doi.org/10.1029/2018GL078374

Usami, T. (1996). Materials for comprehensive list of destructive earthquakes in Japan, 416-1995 (Revised and Enlarged Edition). Tokyo, Japan: University of Tokyo Press.

Vavryčuk, V. (2014). Iterative joint inversion for stress and fault orientations from focal mechanisms. Geophysical Journal International, 199, 69–77. https://doi.org/10.1093/gji/ggu224

Vavryčuk, V., Bouchaala, F., & Fischer, T. (2013). High-resolution fault image from accurate locations and focal mechanisms of the 2008 swarm earthquakes in West Bohemia, Czech Republic. Tectonophysics, 590, 189–195. https://doi.org/10.1016/j.tecto.2013.01.025

Wallace, R. E. (1951). Geometry of shearing stress and relation to faulting. The Journal of Geology, 59, 118–130. https://doi.org/10.1086/625831

Wang, K., Wada, I., & Ishikawa, Y. (2004). Stresses in the subducting slab beneath southwest Japan and relation with plate geometry, tectonic forces, slab dehydration, and damaging earthquakes. Journal of Geophysical Research, 109, B08304. https://doi.org/10.1029/2003JB002888

Warren-Smith, E., Fry, B., Wallace, L., Chon, E., Henrys, S., Sheehan, A., et al. (2019). Episodic stress and fluid pressure cycling in subducting oceanic crust during slow slip. Nature Geoscience, 12, 475–481. https://doi.org/10.1038/s41561-019-0367-x

Wech, A. G., Creager, K. C., Houston, H., & Vidale, J. E. (2010). An earthquake-like magnitude-frequency distribution of slow slip in northern Cascadia. Geophysical Research Letters, 37, L22310. https://doi.org/10.1029/2010GL044881

Wessel, P., Smith, W. H. F., Scharroo, R., Luis, J., & Wobbe, F. (2013). Generic mapping tools: Improved version released. Eos, 94, 409–410. https://doi.org/10.1002/2013EO450001

Yokota, Y., Ishikawa, T., Watanabe, S. I., Tashiro, T., & Asada, A. (2016). Seafloor geodetic constraints on interplate coupling of the Nankai Trough megathrust zone. Nature, 534, 374–377. https://doi.org/10.1038/nature17632

Zhuang, J., Ogata, Y., & Vere-Jones, D. (2002). Stochastic declustering of space-time earthquake occurrences. Journal of the American Statistical Association, 97, 369–380. https://doi.org/10.1198/016214502760046925

Zoback, M. D., Townend, J., & Grollimund, B. (2002). Steady-state failure equilibrium and deformation of intraplate lithosphere. International Geology Review, 44, 383–401. https://doi.org/10.2747/0020-6814.44.5.383

Zonenshain, L. P., & Savostin, L. A. (1981). Geodynamics of the Baikal rift zone and plate tectonics of Asia. Tectonophysics, 76, 1–45. https://doi.org/10.1016/0040-1951(81)90251

Chapter III

Abadi, M., Agarwal, A., Barham, P., Brevdo, E., Chen, Z., Citro, C., et al. (2016). TensorFlow: Large-Scale Machine Learning on Heterogeneous Distributed Systems. ArXiv:1603.04467 [Cs]. Retrieved from http://arxiv.org/abs/1603.04467

van Asch, T. W. J. (2005). Modelling the hysteresis in the velocity pattern of slow-moving earth flows: the role of excess pore pressure. Earth Surface Processes and Landforms, 30(4), 403–411. https://doi.org/10.1002/esp.1147

Battaglia, J., & Aki, K. (2003). Location of seismic events and eruptive fissures on the Piton de la Fournaise volcano using seismic amplitudes. Journal of Geophysical Research: Solid Earth, 108(B8). https://doi.org/10.1029/2002JB002193

Blakely, R. J., Sherrod, B. L., Weaver, C. S., Wells, R. E., Rohay, A. C., Barnett, E. A., & Knepprath, N. E. (2011). Connecting the Yakima fold and thrust belt to active faults in the Puget Lowland, Washington. Journal of Geophysical Research: Solid Earth, 116(B7). https://doi.org/10.1029/2010JB008091

CloudCompare. (n.d.). (Version 2.12). Retrieved from http://www.cloudcompare.org/

Corominas, J., Moya, J., Ledesma, A., Lloret, A., & Gili, J. A. (2005). Prediction of ground displacements and velocities from groundwater level changes at the Vallcebre landslide (Eastern Pyrenees, Spain). Landslides, 2(2), 83–96. https://doi.org/10.1007/s10346-005-0049-1

Ester, M., Kriegel, H.-P., Sander, J., & Xu, X. (1996). A density-based algorithm for discovering clusters in large spatial databases with noise. In Proceedings of the Second International Conference on Knowledge Discovery and Data Mining (pp. 226–231). Portland, Oregon: AAAI Press.

Gomberg, J., Bodin, P., Savage, W., & Jackson, M. E. (1995). Landslide faults and tectonic faults, analogs?: The Slumgullion earthflow, Colorado. Geology, 23(1), 41–44. https://doi.org/10.1130/0091-7613(1995)023<0041:LFATFA>2.3.CO;2

Heimann, S., Kriegerowski, M., Isken, M., Cesca, S., Daout, S., Grigoli, F., et al. (2017). Pyrocko - An open-source seismology toolbox and library. https://doi.org/10.5880/GFZ.2.1.2017.001

Hungr, O., Leroueil, S., & Picarelli, L. (2014). The Varnes classification of landslide types, an update. Landslides, 11(2), 167–194. https://doi.org/10.1007/s10346-013-0436-y

Iverson, R. M., & Major, J. J. (1987). Rainfall, ground-water flow, and seasonal movement at Minor Creek landslide, northwestern California: Physical interpretation of empirical relations. GSA Bulletin, 99(4), 579–594. https://doi.org/10.1130/0016-7606(1987)99<579:RGFASM>2.0.CO;2

John, J. A., & Draper, N. R. (1980). An Alternative Family of Transformations. Journal of the Royal Statistical Society. Series C (Applied Statistics), 29(2), 190–197. https://doi.org/10.2307/2986305

Kennett, B. L. N., Engdahl, E. R., & Buland, R. (1995). Constraints on seismic velocities in the Earth from traveltimes. Geophysical Journal International, 122(1), 108–124. https://doi.org/10.1111/j.1365-246X.1995.tb03540.x

Krischer, L., Megies, T., Barsch, R., Beyreuther, M., Lecocq, T., Caudron, C., & Wassermann, J. (2015). ObsPy: a bridge for seismology into the scientific Python ecosystem. Computational Science & Discovery, 8(1), 014003. https://doi.org/10.1088/1749-4699/8/1/014003

Massey, C. I., Petley, D. N., & McSaveney, M. J. (2013). Patterns of movement in reactivated landslides. Engineering Geology, 159, 1–19. https://doi.org/10.1016/j.enggeo.2013.03.011

McPhillips, D. F., Herrick, J. A., Ahdi, S., Yong, A. K., & Haefner, S. (2020). Updated Compilation of VS30 Data for the United States [Data set]. U.S. Geological Survey. https://doi.org/10.5066/P9H5QEAC

Mousavi, S. M., Ellsworth, W. L., Zhu, W., Chuang, L. Y., & Beroza, G. C. (2020). Earthquake transformer—an attentive deep-learning model for simultaneous earthquake detection and phase picking. Nature Communications, 11(1), 3952. https://doi.org/10.1038/s41467-020-17591-w

Norrish, N. I. (2018, January 30). Rattlesnake Hills Landslide Evaluation. Wyllie &
Norrish Rock Engineers. Retrieved from
https://www.governor.wa.gov/sites/default/files/WN%20Rattlesnake%20Hills%20Landsl
ide%20Evaluation%20.pdf

Pedregosa, F., Varoquaux, G., Gramfort, A., Michel, V., Thirion, B., Grisel, O., et al.
(2011). Scikit-learn: Machine Learning in Python. Journal of Machine Learning
Research, 12(85), 2825–2830.

Prior, D. B., & Stephens, N. (1972). Some Movement Patterns of Temperate Mudflows:
Examples from Northeastern Ireland. GSA Bulletin, 83(8), 2533–2544.
https://doi.org/10.1130/0016-7606(1972)83[2533:SMPOTM]2.0.CO;2

Reidel, S. P., Camp, V. E., Ross, M. E., Wolff, J. A., Martin, B. S., Tolan, T. L., & Wells,
R. E. (2013). The Columbia River Flood Basalt Province. Geological Society of America.

Ronneberger, O., Fischer, P., & Brox, T. (2015). U-Net: Convolutional Networks for
Biomedical Image Segmentation. ArXiv:1505.04597 [Cs]. Retrieved from
http://arxiv.org/abs/1505.04597

Ross, Z. E., Meier, M. A., & Hauksson, E. (2018). P Wave Arrival Picking and First-
Motion Polarity Determination With Deep Learning. Journal of Geophysical Research:
Solid Earth, 123(6), 5120–5129. https://doi.org/10.1029/2017JB015251

Sagy, A., Brodsky, E. E., & Axen, G. J. (2007). Evolution of fault-surface roughness with
slip. Geology, 35(3), 283–286. https://doi.org/10.1130/G23235A.1

University of Washington. (1963). Pacific Northwest Seismic Network - University of
Washington [SEED data]. International Federation of Digital Seismograph Networks.
https://doi.org/10.7914/SN/UW

Wessel, P., Luis, J. F., Uieda, L., Scharroo, R., Wobbe, F., Smith, W. H. F., & Tian, D.
(2019). The Generic Mapping Tools Version 6. Geochemistry, Geophysics, Geosystems,
20(11), 5556–5564. https://doi.org/10.1029/2019GC008515

Zhu, W., & Beroza, G. C. (2019). PhaseNet: a deep-neural-network-based seismic arrival-time picking method. Geophysical Journal International, 216(1), 261–273. https://doi.org/10.1093/gji/ggy423

Chapter IV

1.   Church JA, White NJ. Sea-Level Rise from the Late 19th to the Early 21st Century. The Earth's Cryosphere and Sea Level Change. 2011. pp. 585–602. doi:10.1007/978-94-007-2063-3_17

2.   Moucha R, Forte AM, Mitrovica JX, Rowley DB, Quéré S, Simmons NA, et al. Dynamic topography and long-term sea-level variations: There is no such thing as a stable continental platform. Earth and Planetary Science Letters. 2008. pp. 101–108. doi:10.1016/j.epsl.2008.03.056

3.   Wöppelmann G, Marcos M. Vertical land motion as a key to understanding sea level change and variability. Rev Geophys. 2016;54: 64–92. Available: https://agupubs.onlinelibrary.wiley.com/doi/abs/10.1002/2015RG000502

4.   Clark J, Mitrovica JX, Latychev K. Glacial isostatic adjustment in central Cascadia: Insights from three-dimensional Earth modeling. Geology. 2019;47: 295–298. doi:10.1130/G45566.1

5.   Petersen MD, Moschetti MP, Powers PM, Mueller CS, Haller KM, Frankel AD, et al. Documentation for the 2014 update of the United States national seismic hazard maps. Open-File Report. 2014. doi:10.3133/ofr20141091

6.   Gao D, Wang K, Insua TL, Sypus M, Riedel M, Sun T. Defining megathrust tsunami source scenarios for northernmost Cascadia. Nat Hazards. 2018;94: 445–469. https://idp.springer.com/authorize/casa?redirect_uri=https://link.springer.com/article/10.1007/s11069-018-3397-6&casa_token=1LnTmziAAxoAAAAA:G_Bg4yrzqWOQ9DN7AtAS5Em35kGVTKYcmZ1sjya40xEEF4tf3fwyQGAq8pF9HchnEB3gczYwQWkEzn_xFw

7.   Burgette RJ, Weldon RJ, Schmidt DA. Interseismic uplift rates for western Oregon and along-strike variation in locking on the Cascadia subduction zone. J Geophys Res [Solid Earth]. 2009;114. Available: https://agupubs.onlinelibrary.wiley.com/doi/abs/10.1029/2008JB005679

8.   Frankel A, Petersen M. Models of Earthquake Recurrence and Down-Dip Edge of Rupture for the Cascadia Subduction Zone. US Geological Survey. 2012. Available: http://wgcep.org/sites/wgcep.org/files/CSZucerf3REV0629.docx

9.   Yousefi M, Milne GA, Love R, Tarasov L. Glacial isostatic adjustment along the Pacific coast of central North America. Quaternary Science Reviews. 2018. pp. 288–311. doi:10.1016/j.quascirev.2018.06.017

10.   James TS, Gowan EJ, Wada I, Wang K. Viscosity of the asthenosphere from glacial isostatic adjustment and subduction dynamics at the northern Cascadia subduction zone, British Columbia, Canada. J Geophys Res. 2009;114: 536. doi:10.1029/2008JB006077

11. Goldfinger C, Nelson CH, Morey AE, Johnson JE, Patton JR, Karabanov EB, Gutierrez-Pastor J, Eriksson AT, Gracia E, Dunhill G, Enkin RJ. Turbidite event history—Methods and implications for Holocene paleoseismicity of the Cascadia subduction zone. US Geological Survey; 2012. Doi:10.3133/pp1661F

12. Wells RE, McCaffrey R. Steady rotation of the Cascade arc. Geology. 2013 Sep 1;41(9):1027-30. doi:10.1130/G34514.1

13. Troost KG, Booth DB. Geology of Seattle and the Seattle area, Washington. Reviews in Engineering Geology. 2008 Nov 1;20(0):1-36.

14. Schuster JE. Geologic map of Washington state. Olympia, WA: Washington State Department of Natural Resources; 2005.

15. Miller MB, Cowan DS. Roadside geology of Washington. Mountain Press; 2017.

16.   Snay R, Cline M, Dillinger W, Foote R, Hilla S, Kass W, et al. Using global positioning system-derived crustal velocities to estimate rates of absolute sea level change from North American tide gauge records. Journal of Geophysical Research: Solid Earth. 2007. doi:10.1029/2006jb004606

17.   Mazzotti S, Jones C, Thomson RE. Relative and absolute sea level rise in western Canada and northwestern United States from a combined tide gauge-GPS analysis. J Geophys Res C: Oceans. 2008;113. Available: https://agupubs.onlinelibrary.wiley.com/doi/abs/10.1029/2008JC004835

18.   Hamlington BD, Thompson P, Hammond WC, Blewitt G, Ray RD. Assessing the impact of vertical land motion on twentieth century global mean sea level estimates. J Geophys Res C: Oceans. 2016;121: 4980–4993. doi:10.1002/2016JC011747

19.   Montillet J-P, Melbourne TI, Szeliga WM. GPS vertical land motion corrections to sea-level rise estimates in the Pacific Northwest. J Geophys Res C: Oceans. 2018;123: 1196–1212. Available: https://agupubs.onlinelibrary.wiley.com/doi/abs/10.1002/2017JC013257

20.   Mote P, Petersen A, Reeder S, Shipman H, Whitely Binder L. Sea level rise in the coastal waters of Washington State. 2008. Available: https://digital.lib.washington.edu/researchworks/bitstream/handle/1773/34589/1.pdf?sequence=1

21.   Holdahl SR, Faucher F, Dragert H. Contemporary vertical crustal motion in the Pacific Northwest. Slow deformation and transmission of stress in the earth. 1989;49: 17–29. Available: https://books.google.com/books?hl=en&lr=&id=Hzvh3RkhV4gC&oi=fnd&pg=PA17&dq=Contemporary+vertical+crustal+motion+in+the+Pacific+Northwest+in+Choen+and+Vanicek+(eds)+Slow+deformation+and+transmission+of+stress+in+the+earth&ots=EeHXJR3X-W&sig=fbFKjvF6UbhVWPubNubTR33ct7g

22.   Mitchell CE, Vincent P, Weldon RJ, Richards MA. Present-day vertical deformation of the Cascadia Margin, Pacific Northwest, United States. Journal of Geophysical Research: Solid Earth. 1994. pp. 12257–12277. doi:10.1029/94jb00279

23.   Verdonck D. Contemporary vertical crustal deformation in Cascadia. Tectonophysics. 2006;417: 221–230. doi:10.1016/j.tecto.2006.01.006

24.   Wöppelmann G, Martin Miguez B, Bouin M-N, Altamimi Z. Geocentric sea-level trend estimates from GPS analyses at relevant tide gauges world-wide. Glob Planet Change. 2007;57: 396–406. doi:10.1016/j.gloplacha.2007.02.002

25.   National Research Council, Division on Earth and Life Studies, Ocean Studies Board, Board on Earth Sciences and Resources, Committee on Sea Level Rise in California, Oregon, and Washington. Sea-Level Rise for the Coasts of California, Oregon, and Washington: Past, Present, and Future. National Academies Press; 2012. Available: https://play.google.com/store/books/details?id=_oBs2zAwtGgC

26.   Halvorsen E MJ. Planning for change: climate adaptation survey results, Washington State, 2013. . Washington Sea Grant; 2014. Report No.: WSG-TR 14-01.

27. Hung WC, Hwang C, Chen YA, Zhang L, Chen KH, Wei SH, Huang DR, Lin SH. Land subsidence in Chiayi, Taiwan, from compaction well, leveling and alos/palsar: Aquaculture-induced relative sea level rise. Remote Sensing. 2018 Jan;10(1):40. doi:10.3390/rs10010040

28.   Ian Miller, Harriet Morgan, Guillaume Mauger, Tyler Newton, Ray Weldon, David Schmidt, Mark Welch, Eric Grossman. Projected Sea Level Rise for Washington State – A 2018 Assessment. Washington Coastal Resilience Project; 2018 Jul. Available: https://cig.uw.edu/resources/special-reports/sea-level-rise-in-washington-state-a-2018-assessment/

29.   Blewitt G, Hammond WC, Kreemer C. Harnessing the GPS data explosion for interdisciplinary science. EOS. 2018;99: 1–2. Available: https://eos.org/science-updates/harnessing-the-gps-data-explosion-for-interdisciplinary-science

30.   Zumberge JF. Automated GPS Data Analysis Service. GPS Solutions. 1999;2: 76–78. doi:10.1007/PL00012760

31.   Jamason P, Bock Y, Fang P, Gilmore B, Malveaux D, Prawirodirdjo L, et al. SOPAC Web site (http://sopac.ucsd.edu). GPS Solutions. 2004;8: 272–277. doi:10.1007/s10291-004-0118-2

32.   Miller M, Johnson D, Rubin C, Dragert H, Endo E, Humphreys E, et al. GPS Monitoring of the Cascadia Margin: The Pacific Northwest Geodetic Array (PANGA). Eos Trans AGU. 1997;78: 46.

33.   Herring TA, Melbourne TI, Murray MH, Floyd MA, Szeliga WM, King RW, et al. Plate Boundary Observatory and related networks: GPS data analysis methods and geodetic products. Rev Geophys. 2016;54: 759–808. Available: https://agupubs.onlinelibrary.wiley.com/doi/full/10.1002/2016RG000529

34.   Santamaría-Gómez A, Gravelle M, Wöppelmann G. Long-term vertical land motion from double-differenced tide gauge and satellite altimetry data. J Geodesy. 2014;88: 207–222. Available: https://idp.springer.com/authorize/casa?redirect_uri=https://link.springer.com/content/pdf/10.1007/s00190-013-0677-5.pdf&casa_token=nTDhZFwxg2cAAAAA:FWWAbl2RVYYVLCsFb9gw4CRBkTlc0jErhfZf1d5YGLMw4MbfSk2tZLZLAh-izV2M4VAtdj0Y_XHFavzx2Q

35.   Zervas CE. Sea level variations of the United States, 1854-2006. 2009. Available: https://repository.library.noaa.gov/view/noaa/2565

36.   Krogstad RD, Schmidt DA, Weldon RJ, Burgette RJ. Constraints on accumulated strain near the ETS zone along Cascadia. Earth Planet Sci Lett. 2016;439: 109–116. doi:10.1016/j.epsl.2016.01.033

37.   Schmidt D, Weldon R, Burgette R, Krogstad R. The distribution of interseismic locking on the Cascadia Subduction Zone constrained by leveling, tide gauge, and GPS data. AGUFM. 2011;2011: G53C–05. Available: https://earthquake.usgs.gov/static/lfs/nshm/workshops/PACNW2012/Schmidt2012CSZ.pdf

38.   Wang K, Wells R, Mazzotti S, Hyndman RD, Sagiya T. A revised dislocation model of interseismic deformation of the Cascadia subduction zone. Journal of Geophysical Research: Solid Earth. 2003. doi:10.1029/2001jb001227

39. Frankel A, Petersen M. Models of Earthquake Recurrence and Down-Dip Edge of Rupture for the Cascadia Subduction Zone. US Geological Survey Open-File Rept. 2013-1165-P, and California Geol. Surv. Special Rept. 228-P. 2012 Jun 29.

40.   Amidror I. Scattered data interpolation methods for electronic imaging systems: a survey. J Electron Imaging. 2002;11: 157–176. Available: https://infoscience.epfl.ch/record/99883

41.   van Vuuren DP, Edmonds J, Kainuma M, Riahi K, Thomson A, Hibbard K, et al. The representative concentration pathways: an overview. Clim Change. 2011;109: 5. doi:10.1007/s10584-011-0148-z

42.   Kopp RE, Horton RM, Little CM, Mitrovica JX, Oppenheimer M, Rasmussen DJ, et al. Probabilistic 21st and 22nd century sea-level projections at a global network of tide-gauge sites. Earth's Future. 2014. pp. 383–406. doi:10.1002/2014ef000239

43.   Imakiire T, Koarai M. Wide-area land subsidence caused by "the 2011 Off the Pacific Coast of Tohoku Earthquake." Soils Found. 2012;52: 842–855. doi:10.1016/j.sandf.2012.11.007

44.   Witter RC, Zhang YJ, Wang K, Priest GR, Goldfinger C, Stimely L, et al. Simulated tsunami inundation for a range of Cascadia megathrust earthquake scenarios at Bandon, Oregon, USA. Geosphere. 2013;9: 1783–1803. doi:10.1130/GES00899.1

45. Nelson AR, Shennan I, Long AJ. Identifying coseismic subsidence in tidal-wetland stratigraphic sequences at the Cascadia subduction zone of western North America. Journal of Geophysical Research: Solid Earth. 1996 Mar 10;101(B3):6115-35. doi:10.1029/95JB01051

46. Leonard LJ, Hyndman RD, Mazzotti S. Coseismic subsidence in the 1700 great Cascadia earthquake: Coastal estimates versus elastic dislocation models. GSA Bulletin. 2004 May 1;116(5-6):655-70. doi:10.1130/B25369.1

47.   Uieda L, Tian D, Leong WJ, Toney L, Newton T, Wessel P. PyGMT: A Python interface for the Generic Mapping Tools. Zenodo. 2020. doi:10.5281/zenodo.4253459

48. Wessel P, Luis JF, Uieda L, Scharroo R, Wobbe F, Smith WH, Tian D. The generic mapping tools version 6. Geochemistry, Geophysics, Geosystems. 2019 Nov;20(11):5556-64. doi:10.1029/2019GC008515

49.   Hunter JD. Matplotlib: A 2D Graphics Environment. Comput Sci Eng. 2007;9: 90–95. doi:10.1109/MCSE.2007.55